BLENDS OF POLYDIOCTYLFLUORENE (PFO) WITH POLYMERIC AND MONOMERIC ENERGY ACCEPTORS: CORRELATION OF FLUORESCENCE ENERGY TRANSFER AND FILM MORPHOLOGY IN BREATH FIGURES AND FILMS

A Dissertation
Presented to
The Academic Faculty

by

Vu Anh Nguyen

In Partial Fulfillment
of the Requirements for the Degree
Doctor of Philosophy in the
School of Chemistry and Biochemistry

Georgia Institute of Technology
August 2008

BLENDS OF POLYDIOCTYLFLUORENE (PFO) WITH POLYMERIC AND MONOMERIC ENERGY ACCEPTORS: CORRELATION OF FLUORESCENCE ENERGY TRANSFER AND FILM MORPHOLOGY IN BREATH FIGURES AND FILMS

Approved by:

Dr. Laren M. Tolbert, Advisor
School of Chemistry and Biochemistry
Georgia Institute of Technology

Dr. Angus Wilkinson
School of Chemistry and Biochemistry
Georgia Institute of Technology

Dr. Andrew Lyon
School of Chemistry and Biochemistry
Georgia Institute of Technology

Dr. Mohan Srinivasarao
School of Polymer, Textile, and Fiber Engineering
Georgia Institute of Technology

Dr. David Collard
School of Chemistry and Biochemistry
Georgia Institute of Technology

Date Approved: December 20, 2007

DEDICATION

This dissertation is dedicated with deep gratitude to my wife Hong-Diem, my grand-mother Phuc, my parents Hien and Loi, all my brothers and sisters (My-Phuoc, Tuyet-Hoa, Thu-Van, Anh-Dung, My-Linh, Anh-Viet), my mother-in-law Hue, my brother-in-law Cuong, my systers-in-law Lan and Cuc, and all my nephews and nieces (Phuong-Mai, Phuong-Loan, Minh-Hoang, Diana, Andy, Khang, Kevin, Katie). They are the joy of my life.

TABLES OF CONTENTS

ACKNOWLEDGEMENTS

First, I would like to thank my advisor, Dr. Laren M. Tolbert, for accepting me into his research group and supporting me in my research. His patience and guidance have enabled me to pursue my interest in scientific research. I also wish to thank Dr. Mohan Srinivasarao, Dr. Andrew Lyon, Dr. David, Collard, and Dr. Angus Wilkinson for serving as my committee members and providing invaluable scientific discussions that stimulate my search for scientific knowledge.

I would like to express my gratitude to: Dr. Ulrich Scherf (in Germany) for kindly providing the PFO samples, Mariachristina Rumi in Dr. Perry's group for her generous gifts of MEH-PPV and TPP samples, Dr. Mohan Srinivasarao for introducing me to the interesting breath figure arrays and for giving me access to his labs and instruments, Dr. Robert Dickson for allowing me to use his single-photon counter, and Dr. Angus Wilkinson for providing access to his X-ray diffractometer.

I wish to thank Dr. Janusz Kowalik for reviewing my thesis and providing daily stimulating discussions, Dr. Christina Bauer for collecting the XRD and SEM data and for always ready to provide assistance, Dr. Kyril Solntsev for helping me with the collection and interpretation of time-resolved fluorescence data, and Dr. Loretta Crow for helping me with the group's chemical inventory supervision. I also wish to thank all members of the Tolbert research group for being extremely friendly and helpful.

I would like to thank all my friends Vu, Diem, Tuan, Vinh, Chau for being true friends in the ups and downs of life.

LIST OF TABLES

LIST OF FIGURES

LIST OF ABBREVIATIONS

AFM	Atomic force microscopy
BFA	Breath figure array
C_{60}	Fullerene
CdSe	Cadmium Selenide
$CHCl_3$	Chloroform
CS_2	Carbon disulfide
DCF	Drop-coated film
EL	Electroluminescence
ET	Energy transfer
F8BT	Poly(9,9-dioctylfluorene-co-benzothiadiazole)
FRET	Fluorescence resonance energy transfer
HOMO	Highest occupied molecular orbital
LB	Langmuir-Blodgett
LCST	Lower critical solution temperature
LED	Light-emitting diode
LUMO	Lowest unoccupied molecular orbital
MEH-PPV	Poly(2-methoxy-5(2'-ethylhexyloxy)-1,4-phenylenevinylene)
MiRC	Microelectronic research center
M_n	Number-average molecular weight
M_w	Weight-average molecular weight
NRA	Nuclear-reaction analysis
P3HT	Poly(3-hexylthiophene)

PEDOT	Poly(3,4-ethylene dioxythiophene)
PF	Poly(9,9-dialkylfluorene)
PFO	Poly(9,9-dioctylfluorene)
PPS	Poly(*para*-phenylene)-*block*-polystyrene
PPV	Poly(phenylene vinylene)
PS	Polystyrene
PSS	Poly(styrene sulphonic acid)
PT	Poly(alkylthiophene)
PV	Photovoltaic
RDDI	Resonant dipole-dipole interaction
SEM	Scanning electron microscopy
SNOM	Scanning near-field optical microscopy
SPS	Star polystyrene
THF	Tetrahydrofuran
TPP	*meso*-tetraphenylporphyrin
UCST	Upper critical solution temperature
XRD	X-ray diffractometry

LIST OF SYMBOLS

$A_a(v)$	Acceptor's absorption spectrum
$E_d(v)$	Donor's emission spectrum
F	Fluorescence intensity of an energy donor in presence of an acceptor
F_d	See F_o
F_d^*	See F
F_o	Fluorescence intensity of an energy donor in absence of an acceptor
G	Gibbs (free) energy
H	Enthalpy
I	Ionization potential
K_a	Association constant of complexation
k_B	Boltzmann constant
k_{ET}	Energy transfer rate
k_{nr}	Rate of non-radiative excited-state relaxation
k_q	Bimolecular quenching rate constant
k_r	Rate of radiative excited-state relaxation
K_{sv}	Stern-Volmer quenching constant
L	Sum of van der Waals radii of donor and acceptor molecules
n	Refraction index of a material
N_a	Avogadro number
N_B	Number of segments per molecule B
P_n	Exciton population in electronic state n
Q	Fluorescence quencher
r	Donor-acceptor separation distance

r_{ij}	Distance between *i* and *j*
R_o	Förster radius
S	Entropy
T	Temperature
v	Frequency of light
V	Segment volume
α	Polarizability
γ	Surface energy
ε_A	See $A_a(v)$
ε_{ij}	Contact energy between *i* and *j* segments
κ^2	Dipole orientation factor
ρ	Donor chromophore density
τ	Excited-state lifetime of an energy donor in presence of an acceptor
τ_d	See τ_o
τ_d^*	See τ
τ_o	Excited-state lifetime of an energy donor in absence of an acceptor
φ_A	Overall volume fraction of component A
Φ_{PL}	Photoluminescence quantum yield
χ	Flory-Huggins segment-segment interaction parameter
Ψ_X	Fluorescence intensity of component X

SUMMARY

The study of energy transfer in mixtures or blends of light-emitting conjugated polymers has great implications not only in energy-saving applications such as organic light-emitting diodes (LEDs) and photovoltaic (PV) technology but also in improving our understanding of the fundamental science underlying the interactions between light and matter. However, research in this field of study is often complicated by the different modes of phase separation and dewetting in the films, membranes, and microstructured surfaces of the blends as a consequence of a host of parameters ranging from the chemical and physical properties of the polymers and their blends, the interactions among the polymers and between the polymers and the substrates, to the kinetics and thermodynamics involved in the preparation of these structures. Obviously, any further advancement in this area requires a better understanding of the correlation of the morphological structures of the polymer-polymer and polymer-dye blends and their optoelectronic properties. Such knowledge will allow industrial applications to be tailored accordingly. For instance, polymer blends having bicontinuous nano-sized phase separation pattern would be beneficial in PV applications as charge carriers can be extracted at the interface. This type of phase separation, on the other hand, is detrimental to LEDs and organic lasers because the formation of donor-acceptor pairs is too insufficient for energy transfer to be efficient.

Here we report a study on the correlation of thin film morphology and energy transfer efficiency of three systems of blends, namely, PFO-P3HT, PFO:MEH-PPV, and PFO-TPP. Two sets of films were prepared and studied: one consists of thin films

fabricated by drop casting from carbon disulfide (CS_2) and chloroform ($CHCl_3$) solutions of the polymer-polymer or polymer-dye mixtures, and the other is comprised of microstructured films having ordered hallow bubble arrays on surface. These microstructured surfaces were prepared by blowing moist air over a drop of the blend solution to induce condensation of water into droplets which grow and pack into hexagonal arrays without coalescence. After the solvent and the water droplets evaporate, the cavities that are left behind by the water droplets form arrays of spherical air bubbles on the surface of the polymer film. This study was done under a hypothesis that the high solvent evaporation rate involved in the process of bubble array formation kinetically inhibits the modes of phase separation that are observed in thin films prepared by drop coating where the solvent evaporates at a much slower rate.

Using fluorescence energy transfer as a means to study phase separation, we found that phase separation in the breath figures of the polymer-polymer and polymer-dye blends is influenced by a number of factors, including material transport dynamics, solubility of the blend components in the solvents, interactions of the solvents with the substrates, and the diffusion rates of the blend components. Phase separation in direction perpendicular to the substrate surface is more extensive in the breath figures cast from carbon disulfide solutions compared to those cast from chloroform solutions. However, lateral phase separation into donor-rich and acceptor-rich domains is observed in samples prepared from either solvent. The classification of the phase-separate morphology is made difficult by the highly non-equilibrium states of the systems.

Phase separation in the drop-coated films, on the other hand, is determined mainly by the solvent evaporation rates. While solvents evaporate rapidly in the breath figure

formation process, they do so at slower rates in the drop-coating procedure and thereby enable the blend components to de-mix in both vertical and lateral directions and to form aggregates and crystals. The time it takes for the solvent to dry in the drop-coating process is too short for equilibrium to be established and, consequently, the phase behavior resembles neither spinodal decomposition nor nucleation and growth, the two types of phase-separate morphology often observed in systems at equilibrium. These findings were confirmed by fluorescence microscopy, AFM, and XRD.

This dissertation is organized as follows. The first three chapters introduce bubble array formation, fluorescence energy transfer, and phase separation in polymer blends, respectively. All experimental results are presented in chapter four and are discussed in relation to the models reviewed in the first three chapters. The thesis is concluded with a sketch of the future research directions on the subject.

CHAPTER 1

INTRODUCTION TO POLYMERIC BUBBLE ARRAYS

1.1 Historical Background

The process of water vapor condensing into droplets on cold solid surfaces was first studied by Aitken and Rayleigh in 1911.[1,2] It was not until 1986 that this commonly observed fogging phenomenon was investigated further by Knobler and Beysens, and they found that these water droplets, termed breath figures, also formed non-coalescent semi-ordered arrays on thin films of oil.[3] Water droplets with size approaching 100 μm were reported in these studies.

In 1994, Francois and co-workers discovered a procedure for forming highly ordered arrays of air bubbles on the surfaces of star polystyrene (SPS) and poly(*para*-

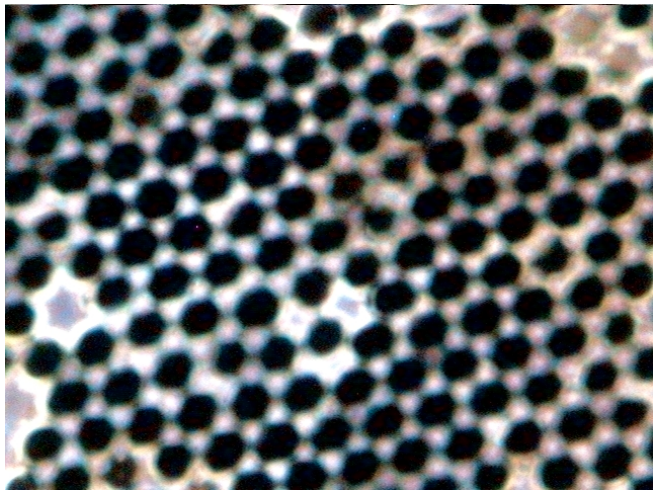

Figure 1.1 Bubble arrays of poly(9,9-dioctylfluorene) cast from CS_2 solution. (0.7 wt% polymer concentration. Bubble size ~7 μm).

phenylene)-*block*-polystyrene (PPS) **1.**[4] The preparation of the breath figure arrays (BFAs) involves the exposure of a drop of the polymer solution in carbon disulfide (CS_2) to a flow of moist air, thereby allowing the water vapor to condense into droplets on the surface of the polymer solution which, at the same time, is being concentrated by the evaporation of the solvent. After all of the solvent and the water droplets have evaporated, the surface of the polymer film is left with an imprint of the water droplets with hole sizes varied from 0.2 to 10 μm. Following the success story of PS-containing polymers, Jenekhe and Chen reported their observation on the formation of multilayered interconnected bubble arrays of polyquinoline-PS block copolymer **2** with bubble sizes of 2-4 μm when cast from CS_2 solution.[5]

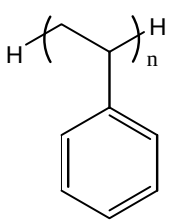

PS

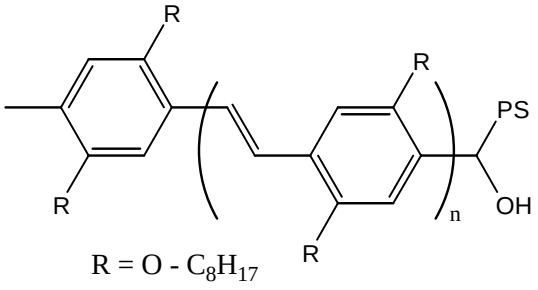

R = O - C_8H_{17}

1

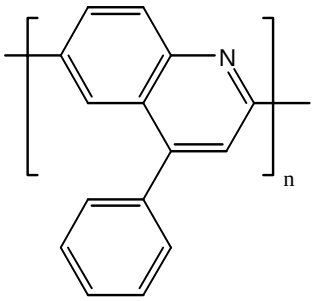

2

Realizing the breath figure formation as a dynamic templating method, Hadziioannou and co-workers prepared bubble arrays from carbon disulfide solutions of PS-containing block copolymers of poly(phenylene vinylene) and used these BFAs as templates for the fabrication of vapor-deposited arrays of mutually connected aluminum cups with dimensions of 3-5 μm.[6]

All these studies share some similar parameters. First, carbon disulfide was the only solvent reported to have the capability of facilitating the formation of BFAs. Second, the presence of polystyrene sequence in the polymers, particularly rod-coil block polystyrenes, seemed to be necessary for the bubble array formation. However, Srinivasarao and others reported the fabrication of highly ordered bubble arrays of linear monocarboxy-terminated polystyrene from not only CS_2 but also from benzene and toluene.[7] Furthermore, Srinivasarao was able to show that, contrary to previous reports, samples prepared from heavier-than-water solvents such as CS_2 give monolayer of arrays of open air bubbles on polymer surface while those prepared from solvents less dense than water produce multilayered bubble arrays. Recently, Han and co-workers reported their study on the formation of high-quality bubble arrays on surface of linear polystyrene prepared from chloroform.[8] Arrays of holes having diameter in the range of 2-5 μm were fabricated from polystyrene that lacks polar terminating groups. Russell and others also used chloroform solution of polystyrene to prepare bubble arrays decorated with CdSe nanoparticles wherein the self-assembly of the CdSe nanoparticles was done *in situ*.[9]

Since the dimensions of the bubble cavities prepared by the breath figure method can be dynamically controlled, polymeric bubble arrays may find such potential uses as microlens arrays,[10,11] picoliter beakers for microanalysis,[12-14] and superhydrophobic surfaces.[15] Self-assembly of nanoparticles into microarrays by way of bubble array formation has been demonstrated[9, 16-17] and may find applications in sensor, filtration, and catalysis.[18,19] Stand-alone films of polymeric bubble arrays can be stretched or compressed[20] to obtain non-spherical pores which may be useful in cell growth. Because of their porous nature, BFAs can be used as sacrificial templates for the fabrication of

microporous films of metals simply by chemically reducing metals onto the bubble arrays.[6] Films of bubble arrays can also be used in photonic band gap applications as the pore size can be made comparable to the wavelength of visible light and the refractive index of the scaffolding material can be fine-tuned.[21,22]

1.2 Experimental Parameters

Bubble array formation is dependent upon a number of parameters, including polymer structure, polymer molecular weight, solvents, concentration, relative humidity, and the speed of airflow. Moreover, it is somewhat an unresolved matter when it comes to the question of what really determine the bubble size and the size distribution of bubbles in the arrays, as well as whether or not the bubbles are multilayered and mutually connected. The variables will now be discussed.

1.2.1 Polymer Structures

It was found that polymers of varying structures formed BFAs. As mentioned above, early studies[23-24] claimed that only star-shaped polystyrenes or block polymers of polystyrenes could form BFAs of decent quality. Lately, however, there have been reports on the formation of bubble arrays from linear polystyrenes,[7-9] a variety of star-shaped polymers such as **3**-**5** [25-27], polyionic polymers **6** and **7**,[28] and conjugated polymers (which will be discussed in the next section). It is clear that the polymer structures are not the only factor that determines whether or not BFAs will form. For example, linear non-functionalized PS forms bubble arrays when cast from chloroform and toluene but not from CS_2 while carboxy-terminated PS does so when CS_2 is used as solvent.[7-8] It is

intriguing that PS with glucose or carboxylate terminating groups form BFAs but ester-terminated PS does not.[29] Similarly, breath figure formation in block copolymer of PS-polyacrylate was found to be dependent on the ratio of the two blocks.[30]

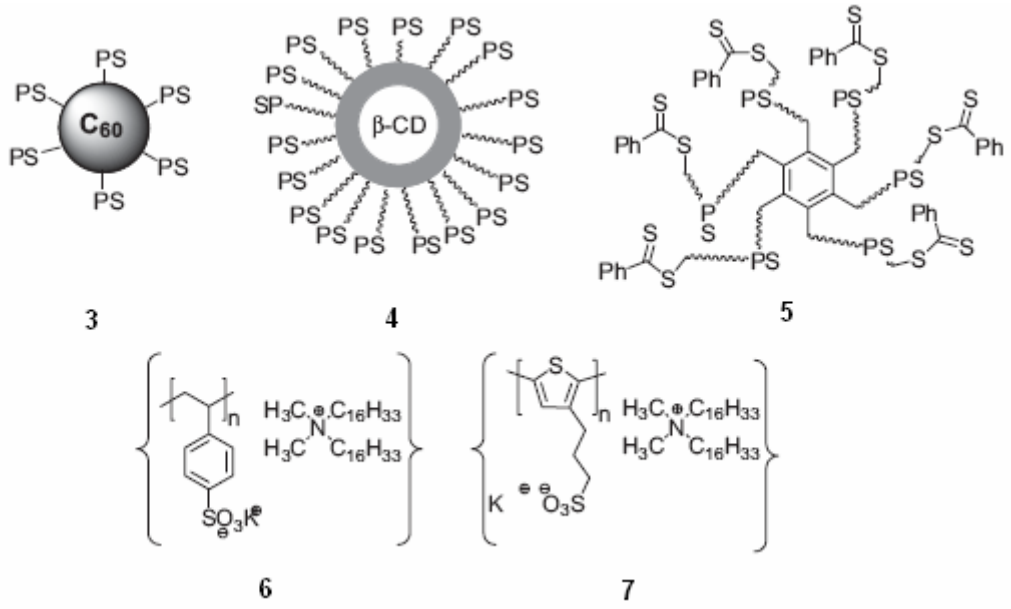

Polymer molecular weight also plays an important role in the formation of BFA. It was claimed that linear PS in toluene formed bubble arrays of better quality with higher molecular weight.[8] In another report, PS-grafted fullerene $C_{60}(PS)_6$ **3** was observed to form well-ordered bubble arrays only when the number-average molecular weight M_n of each PS branch was in the range of 3500-35000 g/mol.[31] It will be shown in chapter 4 that there is an inverse relation between polymer molecular weight and concentration in order to form BFAs.

1.2.2 Solvent

For many polymer and nanoparticle systems, carbon disulfide has been the solvent of choice. There are exceptions, however, as in the case of regular PS prepared from $CHCl_3$ mentioned above. Other solvents that have been successfully used for the

preparation of BFAs include toluene, benzene, and xylene.[29] Amyl acetate has also been used to prepare bubble arrays of nitrocellulose[7,32-34] while Freon-type solvents have been found to be more suitable for surfactant-stabilized nanoparticles and fluorinated polymers.[35,36] BFAs of conjugated polymers in solvents such as methylene chloride and CS_2/pentane mixtures have been reported by Srinivasarao, Bunz, and co-workers.[37] Interestingly, tetrahydrofuran (THF) is not a good solvent for the preparation of breath figures although BFAs of good quality of poly(methyl methacrylate) as well as carboxylate-terminated PS have been prepared in dry air from THF that contains a small amount of water.[38]

1.2.3 Concentration

So far the preparation of BFAs followed a trial-and error process where the concentration of a polymer or a nanoparticle system was changed systematically until ordered bubble arrays were observed. A review of published data indicates a concentration range of 0.1-100 mg/L although a range of 0.1-10 mg/L is more common.[7,9,29] However, experiments done with polymer concentration as high as 40 g/L have been reported.[26] Again, it does not make much sense to talk about polymer concentration without taking into account the polymer molecular weight as the formation of breath figures depends on the viscosity of the polymer, and this will be discussed further in the section on the mechanism of BFA formation below.

1.2.4 Relative Humidity and Airflow Speed

Because the formation of BFAs necessitates water condensation into droplets, one may think that high humidity would facilitate the development of bubble arrays. However, experiments showed that a relative humidity between 70% and 85% works

best.[9,29] Lower humidity does not lead to water condensation while higher humidity causes coagulation of the rapidly growing water droplets and results in disorders.[9] Similarly, too high or too low an airspeed disrupts the bubble-forming process. Generally, an airflow of 150-300 m/min gives the best results[37] although successful preparation of BFAs at air speed of 30 m/min has been reported.[7]

1.2.5 Factors Influencing Bubble Size

There is still not a clear answer on what parameters really determine the size of the bubbles in BFAs. Srinivasarao and others found that bubble size decreased from 6 μm to 0.5 μm when airflow velocity was increased from 30 m/min to 300 m/min.[7] Smaller bubble size was also observed to correlate with high polymer concentration[28,38] and low humidity[23,24]. The dimensions of the air cavities, moreover, seem to depend on the materials being used. Stenzel and co-workers obtained BFAs with pore diameter of 250 nm from PS-grafted cyclodextrin **4**.[23,24,26,30] However, identical conditions gave pore size of 750 nm in the case of polymer **5**. Furthermore, when the end groups in **5** were changed to $–O-C_8H_2F_{17}$ groups, the size of the air bubbles was reduced to 450 nm. Thus more data are needed in order to find a relationship between air bubble diameter and the experimental factors.

1.3 Bubble Arrays of Conjugated Polymers

Conjugated polymers hold great promise for numerous potential applications in optoelectronics. Thus it is of no surprise that a number of research groups have attempted to prepare BFAs of this class of materials.[29] Bubble arrays of modest to excellent quality

of some conjugated polymers were fabricated and studied. Monolayered arrays of interconnected air bubbles in polymers **8-11** were prepared from CS_2, dichloromethane, and CS_2/pentane mixtures. These interconnected pores may be used to study the sieving process of infiltrated DNA and other materials as demonstrated by Hoagland and co-workers.[39] Air bubbles could also be prepared to be isolated from one

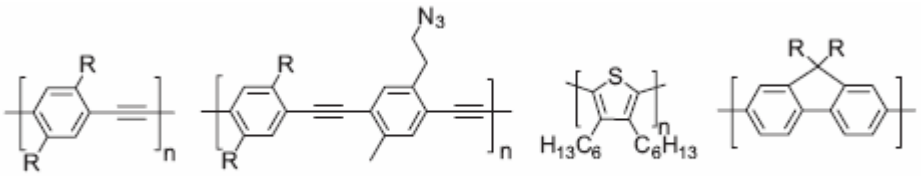

8 **9** **10** **11**

another[12], which may find applications as picoliter wells for analysis of small quantities of analytes. As these studies can attest, BFAs can be prepared not only in PS and PS-derivatized star polymers but also in rigid conjugated polymers having no polar functional groups.

1.4 Current Opinions on the Mechanism of the Formation of Polymeric Bubble Arrays.

The seemingly simple process of the breath figure formation contains intricate details that are not yet well understood and an exact mechanism is still being sought. Nevertheless, some explanations based on temperature gradient effects have been put forth. Using microscopy to observe the bubble-forming process and temperature measurements, Srinivasarao proposed a mechanism **(Figure 1.2)** according to which the

flow of moist air causes evaporative cooling that reduces the temperature on the surface of the polymer solution to near 0^{o}C, which brings about the condensation of water from the air into small droplets or nuclei that grow with time. When these non-interacting water droplets attain certain size, they organize and crystallize into highly mobile hexagonally ordered arrays as driven by the air flow and the convection currents (due to evaporation of solvent) on the solution surface **(Figure 1.4)**. When the temperature between the surface and the droplets approaches similarity, the water droplets sink into the polymer. The whole process may repeat to form multilayered bubble arrays. In

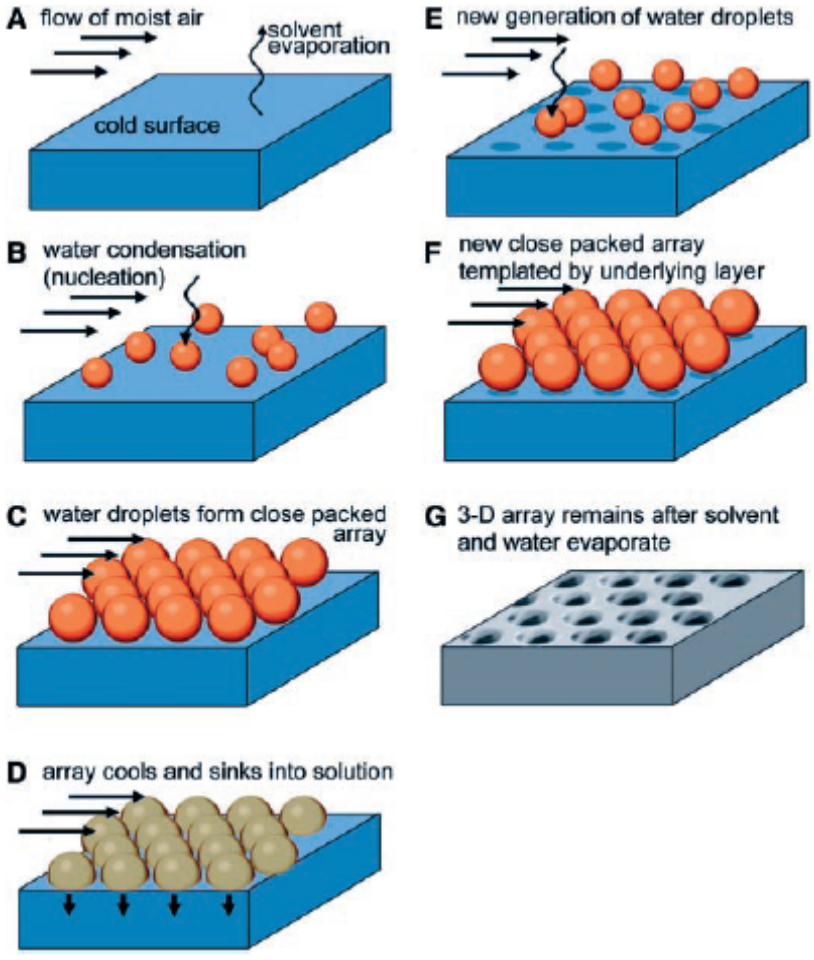

Figure 1. 2 Bubble array formation mechanism proposed by Srinivasarao. (Figure taken from Ref. 7).

this model, the bubbles are not in contact with the polymer solution but rather levitate on the polymer surface. This levitation and the non-coalescence behavior are explained by a combination of a thermocapillary effect and Marangoni convection,[40-42] both being involved by virtue of the presence of temperature gradient between water droplets and the surface of the polymer solution.[7]

Another mechanism proposed by Pitois and Francois suggests that the water droplets do not hover above the solution surface but come in contact with it.[43,44] The authors maintain that the water droplets are each encapsulated by a thin film of the polymer they come in contact with and thereby can avoid coalescence. In this case, too, thermocapillary and Marangori convections are invoked to explain the non-coalescence behavior of the water droplets.

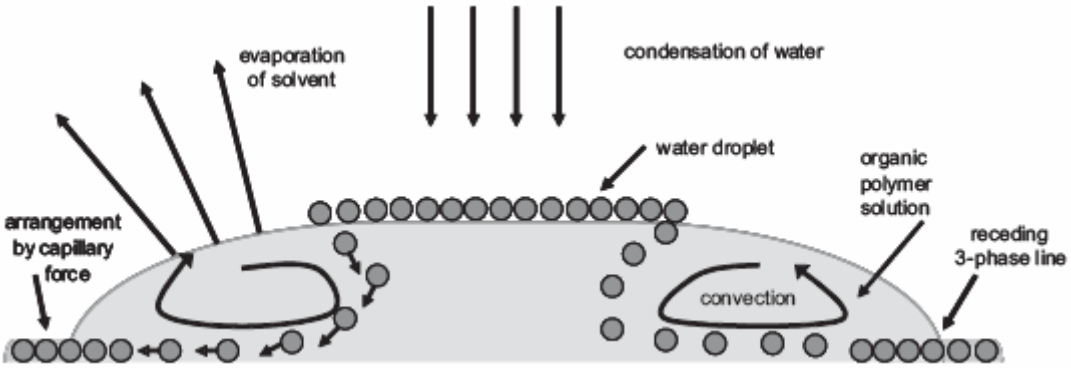

Figure 1.3 Bubble array formation mechanism proposed by Shimomura. (Figure copied from Ref. 29).

Yet another idea[28] held by Shimomura asserts that the Marangori and thermocapillary convections cause the initial water droplets to submerge in polymer

solutions and subsequently rearrange themselves into hexagonally packed arrays **(Figure 1.3)**. However, microscopy data taken during the bubble-array formation process by Srinivasarao and others show rather convincing evidence that the water droplets move about and collide elastically on the surface of the polymer solution **(Figure 1.4)**.

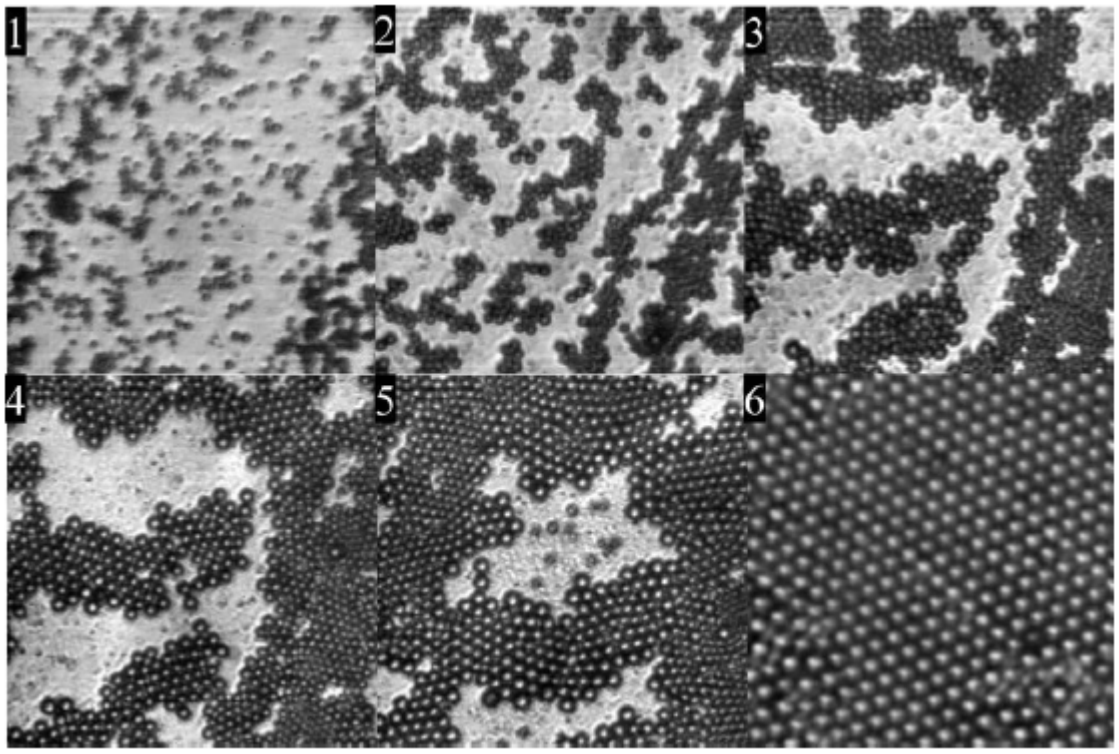

Figure 1.4 Real-time micrographs showing the dynamics of the bubble array formation process. (Figure copied from Ref. 32).

1.5 References

[1] Aitken, J. *Nature* **1911**, *86*, 516

[2] a) Rayleigh, L. *Nature* **1911**, *86*, 416. b) Rayleigh, L. *Nature* **1912**, *90*, 436.

[3] a) Knobler, C. M., Beysens, D., *Europhys. Lett.* **1988**, *6*, 707. b) Steyer, A., Guenoun, P., Beysens, D., Knobler, C. M., *Phys. Rev. B: Condens. Matter Mater. Phys*. **1990**, *42*, 1086.

[4] Widawski, G., Rawiso, M., Francois, B. *Nature* **1994**, *369*, 387.

[5] Jenekhe, S. A., Chen, X. L. *Science* **1999**, *283*, 372.

[6] a) de Boer, B., Stalmach, U., Nijland, H., Hadziioannou, G. *Adv. Mater*. **2000**, *12*, 1581. b) de Boer, B., Stalmach, U., van Hutten, P. F., Melzer, C., Krasnokov, V. V., Hadziioannou, G. *Polymer* **2001**, *42*, 9097.

[7] Srinivasarao, M., Collings, D., Phillips, A., Patel, S. *Science* **2001**, *292*, 79.

[8] Peng, J., Han, Y., Li, B. *Polymer* **2004**, *45*, 447.

[9] Böker, A., Lin, Y., Chiapperini, K., Horowitz, R., Thompson, M., Carreon, V., Xu, T., Abetz, C., Skaff, H., Dinsmore, A. D., Emrick, T., Russell, T. P. *Nature Materials* **2004**, *3*, 302.

[10] Yabu, H., Shimomura, M. *Langmuir* **2005**, *21*, 1709.

[11] a) Jones, C. D., Serpe, M. J., Schroeder, L., Lyon, L. A. *J. Am. Chem. Soc*. **2003**, *125*, 5292. b) Kim, J., Serpe, M. J., Lyon, L. A. *Angew. Chem. Int. Ed*. **2005**, *44*, 1333.

[12] Erdogan, B., Song, L., Wilson, J. N., Park, J. O., Srinivasarao, M., Bunz, U. H. F. *J. Am. Chem. Soc*. **2004**, *126*, 3678.

[13] a) Lapos, J. A., Ewing, A. G. *Anal. Chem*. **2000**, *72*, 4598. b) Clark, R. A., Hietpas, P. B., Ewing, A. G. *Anal. Chem*. **1997**, *69*, 259.

[14] a) Pris, A. D., Porter, M. D. *Nano Lett.* **2002**, *2*, 1087. b) Chiu, D. T., Wilson, C. F., Ryttsen, F., Stromberg, A., Farre, C., Karlsson, A., Nordholm, S., Gaggar, A., Modi, B. P., Moscho, A., Garza-Lopez, R. A., Oewar, O., Zare, R. N. *Science* **1999**, *283*, 1892.

[15] Yabu, H., Takebayashi, M., Tanaka, M., Shimumora, M. *Langmuir* **2005**, *21*, 3235.

[16] a) Li, J., Peng, J., Huang, W., Wu, Y., Fu, J., Cong, Y., Xue, L., Han, Y. *Langmuir* **2005**, *21*, 2017. b) Shah, P. S., Sigman, M. B., Stowell, C. A., Lim, K. T., Johnston, K. P., Korgel, B. A. *Adv. Mater*. **2003**, *15*, 971.

[17] Yonezawa, T., Onoue, S., Kimizuka, N. *Adv. Mater*. **2001**, *13*, 140.

[18] Nam, J. –M., Thaxton, C. S., Mirkin, C. A. *Science* **2003**, *301*, 1884.

[19] Perez, J. M., O'Loughin, T., Simeone, F. J., Weissleder, R., Josephson, L. *J. Am. Chem. Soc*. **2002**, *124*, 2856.

[20] Nishikawa, T., Nonomura, N., Arai, K., Hayashi, J., Sawadaishi, T., Nishiura, Y., Hara, M., Shimomura, M. *Langmuir* **2003**, *19*, 6193.

[21] a) John, S. *Phys. Rev. Lett*. **1987**, *58*, 2486. b) Yablonovitch, E. *Phys. Rev. Lett*. **1987**, *58*, 2059.

[22] Busch, K., John, S. *Phys. Rev. Lett*. **1999**, *83*, 967.

[23] Stenzel, M. H. *Aust. J. Chem*. **2002**, *55*, 239.

[24] Hernendez-Guerrero, M., Davis, T. P., Barner-Kowollik, C., Stenzel, M. H. *Eur. Polym. J*. **2005**, *41*, 2264.

[25] Lu, L., Jenekhe, S. A. *Macromolecules* **2001**, *34*, 6249.

[26] Lord, H. T., Quinn, J. F., Angus, S. D., Whittaker, M. R., Stenzel, M. H., Davis, T. P. *J. Mater. Chem.* **2003**, *13*, 2090.

[27] Barner-Kowollik, C., Dalton, H., Davis, T. P., Stenzel, M. H. *Angew. Chem. Int. Ed*. **2003**, *42*, 3664.

[28] Maruyama, N., Koito, T., Nishida, J., Sawadaishi, T., Cieren, X., Kjiro, K., Karthaus, O., Shimumora, M. *Thin Solid Films* **1998**, *327*, 854.

[29] Bunz, U. H. F. *Adv. Mater*. **2006**, *18*, 973-989.

[30] Stenzel, M. H., Davis, T. P. *Aust. J. Chem*. **2003**, *56*, 1035.

[31] Francois, B., Ederle, Y., Mathis, C. *Synth. Met*. **1999**, *103*, 2382.

[32] Barrow, M. S., Jones, R. L., Park, J. O., Srinivasarao, M., Williams, P. R., Wright, C. J. *Spectroscopy (Amsterdam, Neth.)* **2004**, *18*, 577.

[33] Peng, J., Han, Y., Li. B. *Polymer* **2004**, *45*, 447.

[34] Govor, L. V., Bashmakov, I. A., Kiebooms, R., Dyakonov, V., Parisi, J. *Adv. Mater*. **2001**, *13*, 588.

[35] Shah, P S., Sigman, M. B., Stowell, C. A., Lim, K. T., Johnston, K. P., Korgel, B. A. *Adv. Mater.* **2003**, *15*, 971.

[36] Su, P. Y., Hu, J. C., Cheng, S. L., Chen, L. J. *Appl. Phys. Lett.* **2004**, *84*, 3480.

[37] Song, L., Bly, R. K., Wilson, J. N., Bakbak, S., Park, J. O., Srinivasarao, M., Bunz, U. H. F. *Adv. Mater.* **2004**, *16*, 115.

[38] Park, M. S., Kim, J. K. *Langmuir* **2004**, *20*, 5347.

[39] Nykypanchuk, D., Strey, H. H., Hoagland, D. A. *Science* **2002**, *297*, 987.

[40] Dell' Aversana, P., Banavar, J. R., Koplik, J. *Phys. Fluids* **1996**, *8*, 15.

[41] Dell' Aversana, P., Tontodonato, V., Carotenuto, L. *Phys. Fluids* **1997**, *9*, 2475.

[42] Schatz, M. F., Neitzel, G. P. *Annu. Rev. Fluid. Mech*. **2001**, *33*, 93.

[43] Pitois, O., Francois, B. *Eur. Phys. J. B* **1999**, *8*, 225.

[44] Pitois, O., Francois, B. *Colloid Polym. Sci.* **1999**, *277*, 574.

CHAPTER 2

INTRODUCTION TO ENERGY TRANSFER (ET)

2.1 Historical Background

Since the discovery of the electroluminescence (EL) of poly(*p*-phenylenevinylene) (PPV)in 1990,[1] intensive research has been focused on light-emitting π-conjugated polymers due to their enormous potential applications in color displays[2], white-light electroluminescence devices[3], sensors[4], and organic lasers.[5] Fundamental to these applications are the energy transfer (ET) processes in host-guess or donor-acceptor systems comprised of polymer-polymer, polymer-dye, and dye-dye blends. Blending enables different colors to be achieved without having to synthesize new materials.[6] Moreover, the quantum yield is often enhanced in a blend because self-absorption (by the donor) is minimized due to the red shift in the emission (from the acceptor) as a result of ET. The emission spectra of conjugated polymers usually have large full width at half maximum due to inhomogeneous broadening and vibronic couplings while many highly fluorescing dyes display narrower emission bands. Thus another advantage offered by blending, especially in polymer (donor)-dye (acceptor) blends, is the production of fine narrow emission peaks that are essential to full-color displays and lasers.

Energy transfer is also being exploited for controlling energy flow, which is critical in photosynthesis and photovoltaic applications. Directional energy flow is generally achieved by stacking chromophores in thin film heterostructures[7] or by linking

chromophores with continually decreasing band gaps along polymer chains.[8] A recent study by Tolbert and others based on a composite made by grafting MEH-PPV, an orange-red light-emitting polymer, to pre-oriented hexagonally arrayed pores of silica glass shows that excitation energy is transported preferentially parallel to the pore direction (**Figure 2.1).** [9]

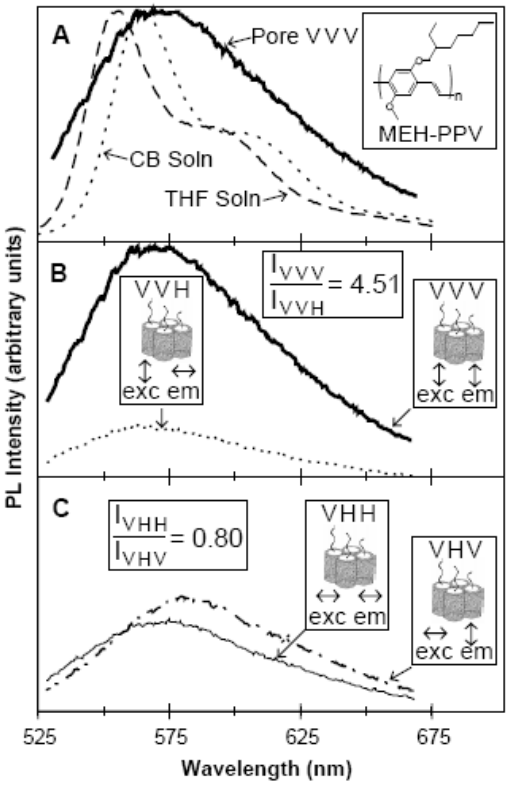

Figure 2.1 Directional energy flow in MEH-PPV/silica composite. Figure copied from Ref. 9.

Energy transfer from a donor to an acceptor may involve electron exchange in a process known as Dexter ET or it may be induced by dipole-dipole interactions. The latter process, known as Coulombic or Förster ET, has received tremendous attention from both theoretical and experimental view points as this mode of ET, besides playing a

key role in photosynthesis, is often observed in donor-acceptor blends of light-emitting materials and is relevant to advanced optoelectronic technology. Concerning the processes involving resonant dipole-dipole interaction (RDDI), excitation energy transfer depends on the donor-acceptor separation, d. When the donor and acceptor are far apart with $d > \lambda/10$, the coupling is mediated by a real photon and the transfer is radiative. On the other hand, when donor and acceptor are close, the coupling is mediated by a virtual photon and the (Förster) transfer is nonradiative.

The study of fluorescence (Förster) resonance energy transfer (FRET) has a long history and may be said to begin with Perry who in 1918 proposed a mechanism based on resonance.[10] Dipole-dipole interactions were not mentioned in the proposed mechanism. Nevertheless, the theory gained support when Cario and Frank reported their finding in 1922 according to which a mixture of mercury and thallium atomic vapors exhibit an emission peak at 535 nm, which is characteristic of thallium, when it was excited with 254 nm light, which corresponds to the mercury resonance line. The involvement of dipole interactions was implicated in a study by Gaviola and Pringsham in 1924 in which progressive depolarization of the emission was observed to correlate with increasing the concentration of a fluorescing species in a viscous solvent. Based on these results, a quantum theory of resonance energy transfer was formulated two years later by Kallmann and London. This theory was based on the Coulombic interactions between the donor and acceptor and introduced a parameter R_o, which is the intermolecular separation at which energy transfer process competes equally with all other decay processes. The relationship between R_o and the spectral overlap between the emission spectrum of the donor and the absorption spectrum of the acceptor was qualitatively proposed in 1932 by Perrin who

worked out a quantum mechanical theory of energy transfer between molecules of the same species in solutions. The first quantitative theory of resonance energy transfer was formulated by Förster in the later 1940's.[11] According to this theory, the criterion for a FRET is a spectral overlap between the donor emission spectrum and the acceptor absorption spectrum, and the spectral overlap is proportional to the parameter R_o, which is now generally known as the Förster transfer radius. Furthermore, the rate of energy transfer is inversely proportional to the sixth power of the intermolecular separation of the donor and acceptor.

Since then, numerous experiments have been performed to check the validity of Förster theory and satisfactory results have been obtained in binary blend systems comprised of small molecules. However, recent studies on polymer-polymer and polymer-dye blends have found the energy transfer behavior in significant disagreement with the theory (see below). The deviations mainly come from assumptions in the theory wherein the molecules are treated as hard spheres and the distribution of the donor and acceptor are uniform. Experimentally, these assumptions are rarely met in the solid-state structures of polymer-polymer and polymer-dye blends because of the non-spherical nature of polymer molecules and the inhomogeneity of the structures caused by phase separation. These recent findings will be discussed further after some theoretical considerations concerning the processes involved in energy transfer are presented.

2.2 Theoretical Considerations

The relaxation of a molecule from its electronically excited state to the ground state is a complex process and dependent upon the nature of the molecule, its thermodynamic state, and the environment surrounding it. Some materials relax by giving off light in a process called fluorescence. When an excited fluorophore is surrounded by other molecules either of the same or different species, fluorescence accompanying the relaxation may be quenched by energy transfer to nearby molecules. If the fluorophore is a conjugated polymer, the excited state may have a longer-than-expected lifetime as the exciton may migrate along the polymer chain before the condition is right for energy transfer to take place. In order to understand better the dynamics of energy transfer and fluorescence quenching, the different processes involved in the relaxation of an excited molecule are now reviewed.

2.2.1 Relaxation of an electronically excited molecule.[12]

When a molecule is electronically excited by radiation or electric discharge, an electron in one of the occupied molecular orbitals is promoted to one of the unoccupied molecular orbitals, depending on the excitation energy. Associated with these electronic energy levels are the vibrational energy levels. After the molecule is brought to its electronically excited state, it may relax to lower excited state or the ground state following different paths as shown in the Jablonski diagram (**Figure 2.2**). (For simplicity, only relaxation to the ground electronic state or the LUMO is discussed). First, the excited molecule undergoes vibrational relaxation to the ground vibrational state of the electronically excited state. From there, it may emit radiation and relax to one of the

vibrational states of the ground electronic state. The emission of radiation is referred to as fluorescence. In this process, the multiplicity does not change and the relaxation is from a singlet to a singlet state. However, the excited molecule may undergo a change of multiplicity from a singlet to a triplet excited state in a process called intersystem crossing, which occurs at a point where the two potential-energy curves of the excited singlet state S_1 and the excited triplet state T intersect. The relaxation, thus, involves a triplet to singlet transition. This radiative process, termed phosphorescence, is a slow process (greater than 100 ns as compared to 1-10 ns for fluorescence) and is formally forbidden due to the change of multiplicity in the transition. Phosphorescence is more commonly found in materials that have heavy atoms, where considerable spin-orbit

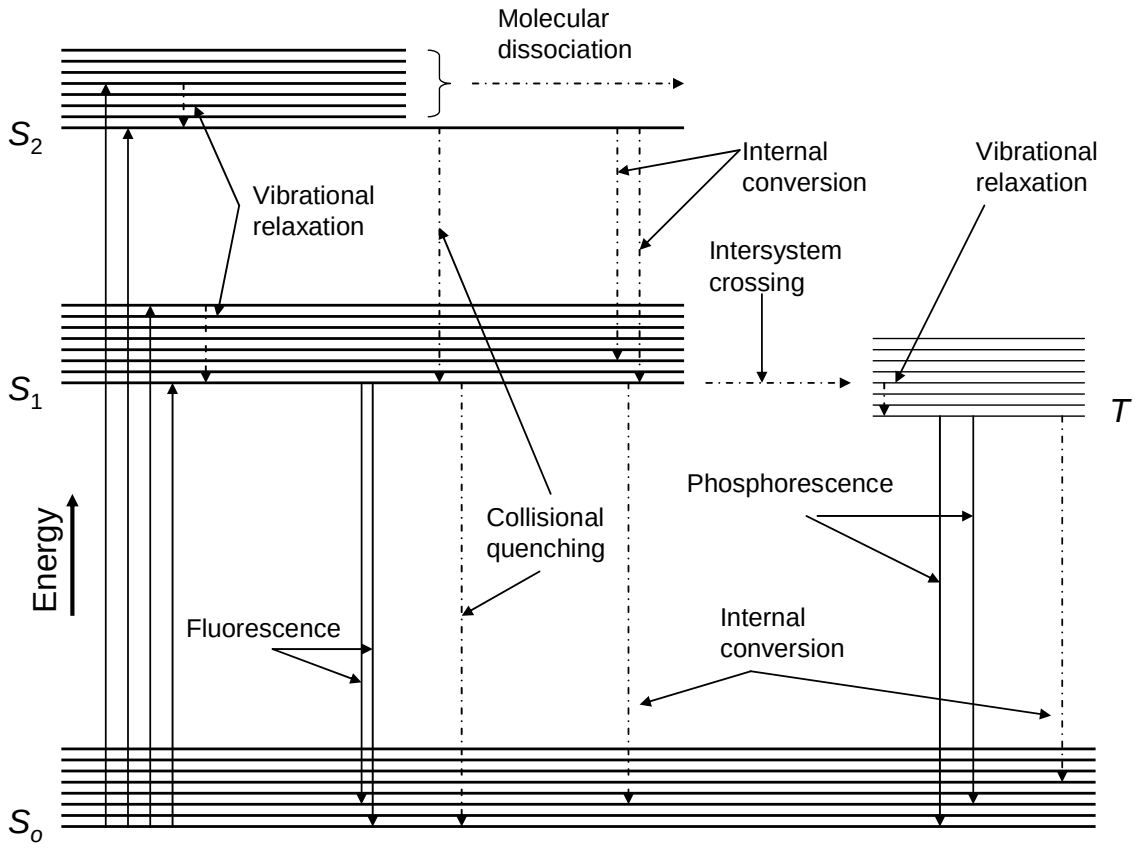

Figure 2.2 Jablonski diagram. (Dotted arrows indicate non-radiative relaxations).

coupling takes place. The phosphorescence is lower in energy than the fluorescence emission, which in turn is of longer wavelength than observed in the absorption. The shift to longer wavelengths in a fluorescence process is called the Stokes shift and comes from the fact that absorption generally occurs from the ground vibrational state whereas fluorescent emissions often end up in excited vibrational states (**Figure 2.2**).

Besides radiative relaxations, an electronically excited species can also undergo non-radiative transitions leading to repopulation of the ground state through a process called internal conversion. An extreme case is where the absorption energy is so high that the molecule dissociates upon vibration, although for polyatomic molecules vibrational redistribution of the energy takes precedent. In addition, vibrational energy can be dissipated by collision of the excited molecule with other molecules which allows relaxation to the ground vibrational state within the same electronic state. Another process involving collisions between molecules is appropriately called collisional quenching, where the excited molecule passes to the electronic ground state and the energy is converted to translational and internal energy, which is eventually dissipated as heat. Since these processes involve collisions, their rates depend on the frequency of collisions and, therefore, are very high in solid state. Non-radiative relaxation can also occur by conversion of the electronic energy into vibrational energy within the molecule itself. However, this mode of relaxation is observed more frequently in the gas phase where the chance of molecular collisions is small.

2.2.2 Fluorescence quenching and FRET[10]

When an electronically excited molecule undergoes collisions with other molecules, it may make a transition to the ground state by converting the energy into heat

as discussed above. The transition is non-radiative and, therefore, no fluorescence is observed. This is not the only process that reduces the fluorescence intensity of a material; other quenching routes include energy transfer, charge transfer, photoreaction, including photobleaching, and the formation of complexes (static quenching). In the simplest case of collisional (dynamic) quenching (**Figure 2.3**), the reduction of fluorescence is a function of the quencher concentration as shown by the Stern-Volmer equation

$$\frac{F_o}{F} = 1 + K_{sv}[Q] \qquad (2.1)$$

where F_o and F are the fluorescence intensities in the absence and presence of quencher, respectively, K_{sv} is known as the Stern-Volmer quenching constant, and $[Q]$ is the concentration of the quencher. Thus a plot of F_o/F versus $[Q]$ should yield a straight line with a slope of K_{sv} and is often called a Stern-Volmer plot. The K_{sv} is directly proportional to the excited-state lifetime τ_o of the fluorescing species in the absence of a

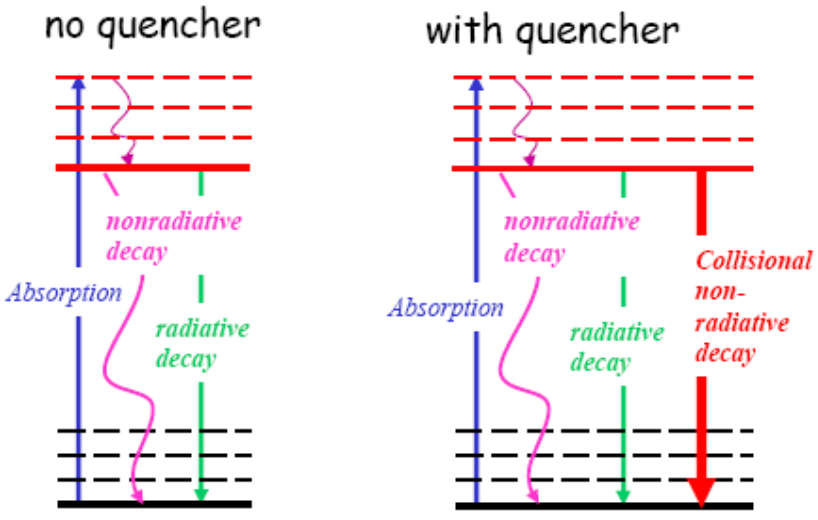

Figure 2.3 Dynamic quenching.

quencher according to the relation

$$K_{sv} = k_q \tau_o \quad (2.2)$$

where k_q is the bimolecular quenching rate constant and proportional to the sum of the diffusion coefficients of the fluorophore and the quencher. For dynamic quenching, the reduction in the excited-state lifetime of a fluorophore is also related to the quencher concentration, or $F_o/F = \tau_o/\tau$, where τ is the excited-state lifetime of the fluorophore in the presence of a quencher. Thus,

$$\frac{\tau_o}{\tau} = 1 + k_q \tau_o [Q] \quad (2.3)$$

and a plot of τ_o/τ versus $[Q]$ should also be linear. However, the behavior of collisional quenching will be significantly affected if static quenching is involved.

There are situations where some molecules of a fluorophore form stable complexes with molecules of either the same or different species, and the resulted complexes do not fluoresce. For this static quenching process, the K_{sv} is replaced by an association constant of the complex K_a in the Stern-Volmer equation. However, the excited-state lifetime of the system is not affected because the quenching does not affect the uncomplexed molecules and therefore $\tau_o = \tau$. Consequently, if a system involves both dynamic and static quenching processes, the Stern-Volmer equation will become

$$\frac{F_o}{F} = (1 + k_q \tau_o [Q])(1 + K_a [Q]) \quad (2.4)$$

and a plot of F_o/F versus $[Q]$ will have an upward curvature as schematically illustrated in **Figure 2.4a**. However, as the excited-state lifetime of the sample is unaffected by static quenching, the plot of τ_o/τ versus $[Q]$ retains its linearity. The Stern-Volmer plot may take the form of a curve as shown in **Figure 2.4b** when the system undergoes only

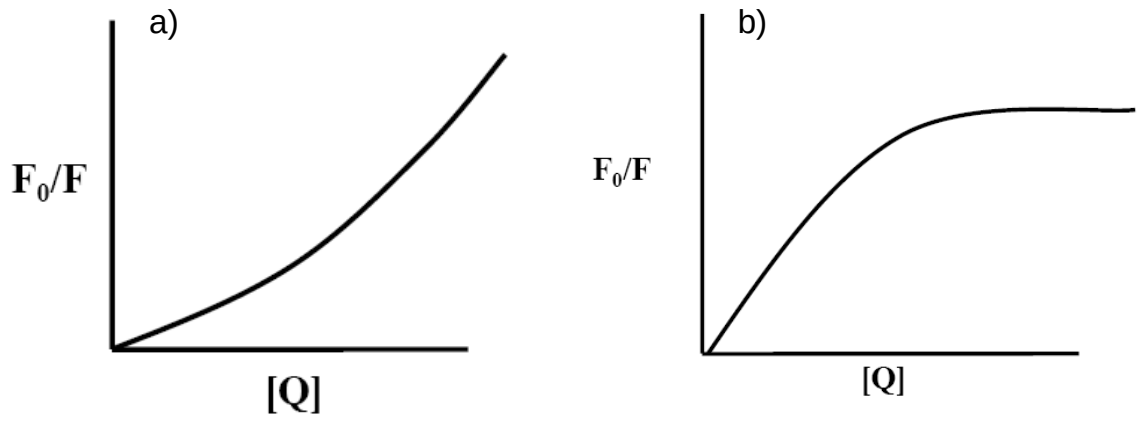

Figure 2.4 Non-linear Stern-Volmer plots. (See text for explanation).

collisional quenching. This behavior happens when some of the fluorophores are inaccessible to the quencher.

The quenching processes just discussed all reduce the fluorescence intensity. However, if the quencher is a fluorophore whose excitation energy is comparable to the emission energy of the quenched then the system fluorescence is not quenched but shifted to longer wavelengths because the quencher now emits fluorescence as it relaxes from an excited state where the excitation is induced by the energy transfer from the initial fluorophore (the donor). If the donor and the acceptor are far apart, the ET process is mediated by emission by the donor and reabsorption by the acceptor. When the donor and acceptor are close, i.e., close to the Förster radius, however, the energy is transferred without emission from the donor. This ET process may be mediated by a virtual photon or it may involve electron exchange.

The electron-exchange interaction in Dexter ET process requires the donor and the acceptor to be within 15-20 Å of each other and it is schematically represented in **Figure 2.5a**. The rate of Dexter-type ET process is[13]

$$k_{ET} = \frac{d}{dt} P_n = \frac{2\pi}{\hbar} Z^2 \int_0^\infty E_d(v) A_a(v) dv \qquad (2.5)$$

where P_n represents the population of excitons in electronic state n, E_d (v) stands for the donor emission spectrum, $A_a(v)$ represents the acceptor absorption spectrum, and Z^2 is a parameter related to orbital interactions and can be expressed as

$$Z^2 \propto e^{\frac{-2r}{L}} \qquad (2.6)$$

where r being the donor-acceptor distant and L is the sum of the van der Waals radii of the donor and acceptor molecules. The integral represents the normalized spectral overlap. Thus the energy transfer rate decreases rapidly with small increase in the donor-acceptor distance and it varies as $e^{-2r/L}$.

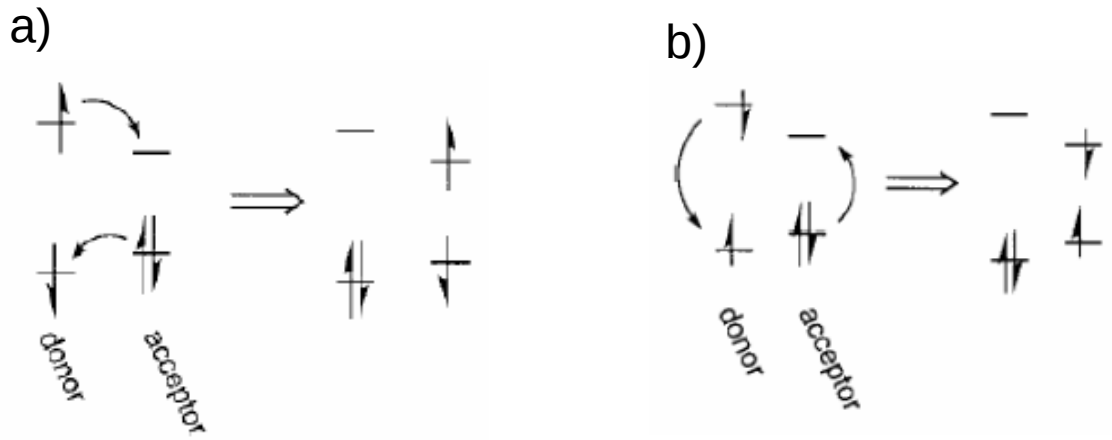

Figure 2.5 Dexter (a) and Förster (b) ET processes.

Förster-type energy transfer can occur at a much larger donor-acceptor distance (up to 10 nm) than Dexter process. This is because the transfer is mediated by dipole-dipole interactions and does not involve electron exchange (**Figure 2.5b**). The process is enabled by resonance (**Figure 2.6**) and depends on the orientation of dipoles as well as sufficient spectra overlap. Since it has to compete with other radiative and non-radiative relaxation modes, its quantum yield is defined as

$$\Phi_{PL} = \int_0^\infty F_d(v)dv = \frac{k_{ET}}{k_{ET} + k_{nr} + k_r} = \frac{k_{ET}}{1/\tau_d^*} \tag{2.7}$$

where $F_d(v)$ represents the donor emission spectrum, k_{ET}, k_{nr}, and k_r are the rates of energy transfer, non-radiative transitions, and radiative transitions, respectively, and τ^*_d is the excited-state life of the donor and defined as $\tau^*_d = 1/(k_{ET} + k_{nr} + k_r)$ whereas the donor lifetime in the absence of ET is $\tau_d = 1/(k_{nr} + k_r)$. Equation 2.7 can be simplified to

$$\Phi_{PL} = 1 - \frac{\tau_d^*}{\tau_d} = 1 - \frac{F_d^*}{F_d} \tag{2.8}$$

where F^*_d and F_d represent the fluorescence intensity of the donor in the presence and absence of FRET, respectively. Thus the Förster ET efficiency is directly related to the energy transfer rate (equation 2.7), which was first derived by Förster in the following expression.

$$k_{ET} = \frac{d}{dt}P_n = \frac{0.5291\kappa^2}{n^4 N_a r^6 \tau_d} \int_0^\infty F_d(v)\varepsilon_a(v)\frac{dv}{v^4} \tag{2.9}$$

where κ^2 represents an orientation factor, n the refractive index of the material, N_a the Avogadro number, r the donor-acceptor separation distance, $F_d(v)$ and $\varepsilon_a(v)$ are the donor emission and acceptor absorption spectrum expressed as functions of wavelength,

respectively. The integral represents the degree of spectral overlap. Thus in contrast to Dexter ET, the rate of energy transfer in Förster process is inversely proportional to the sixth power of the donor-acceptor separation. When this distance is such that the probability of energy transfer equals that of direct donor decay (without ET), it is generally known as the Förster radius and defined as

$$R_o^6 = \frac{0.5291\kappa^2}{n^4 N_a} \int_0^\infty F_d(v)\varepsilon_a(v)\frac{dv}{v^4} \tag{2.10}$$

Equations 2.9 and 2.10 can be combined to give the well-known Förster transfer rate expression,

$$k_{ET} = \frac{1}{\tau_d}\left(\frac{R_o}{r}\right)^6 \tag{2.11}$$

Energy transfer is essentially a dynamic quenching process, and when equation 2.11 is combined with equation 2.3, the energy transfer efficiency is revealed to be reduced in half when R_o = r. Thus the Förster radius can also be viewed as a donor-acceptor separation at which 50% of the excitation energy is transferred to the acceptor.

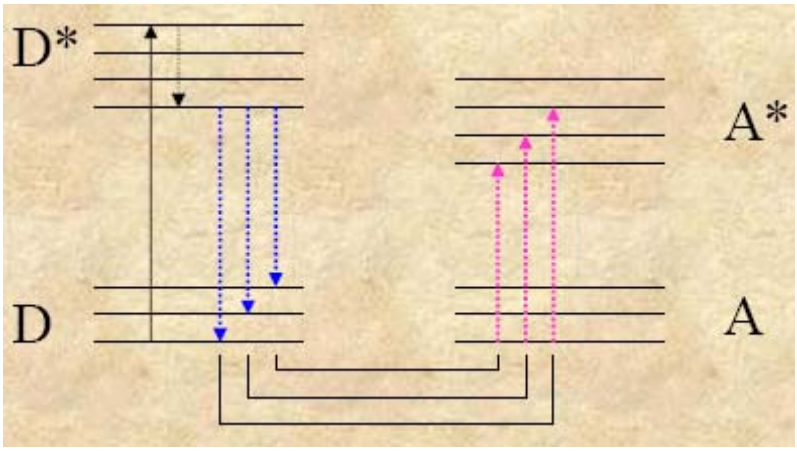

Figure 2.6 Resonance-coupled transitions.

Experimentally, a fluorescence quenching process is generally accepted to come from Förster energy transfer if the Förster critical radius extracted from lifetime measurements (equations 2.3 and 2.11) matches the figure obtained from the spectral overlap (equation 2.10). However, since molecules are treated as hard spheres in the theory while polymer molecules can have many different conformations, significant deviations have been found recently in systems containing fluorescent polymers as will now be discussed.

2.3 Energy Transfer in Polymer-Polymer and Polymer-Dye Blends

Resonance-coupled energy transfer has been attracting a great deal of attention and the Förster model has enjoyed tremendous success in systems of small molecules in solution or in self-assembled monolayer structures. An excellent example comes from a recent report by Andrew and Barnes of the effect of optical cavity on the rate of energy transfer.[14] The study was performed on a donor-acceptor pair comprised of a europium (III) complex and a cyanine derivative with the donor-acceptor separation being controlled by layers of 22-tricosenoic acid using Langmuir-Blodgett (LB) technique. The system not only allows the calculation of the Förster critical radius to be about 14 nm but also shows a direct dependence of the energy transfer rate on the photonic mode density as afforded by the optical cavity formed by sandwiching the donor-acceptor layers between two thermally evaporated silver mirrors (**Figure 2.7**). It is to be noted that energy transfer between planes such as presented in LB structures follows a rate law that is proportional to R^{-4} instead of R^{-6} in systems having isotropic dipole distribution.[15]

While the Förster radius can be calculated with accuracy for energy transfer between small molecules, it often involves some uncertainty when energy transfer is to or from a polymer because of the possibility of exciton migration along the polymer chains. For example, a value of R_o = 3.3 nm was calculated by Shoustikov and others for the energy transfer from tris(8-hydroxyquinoline)aluminum (Alq_3) to *meso*-tetraphenylporphyrin(TPP).[16] Yet, when Alq_3 is replaced by poly(9,9-dioctylfluorene)

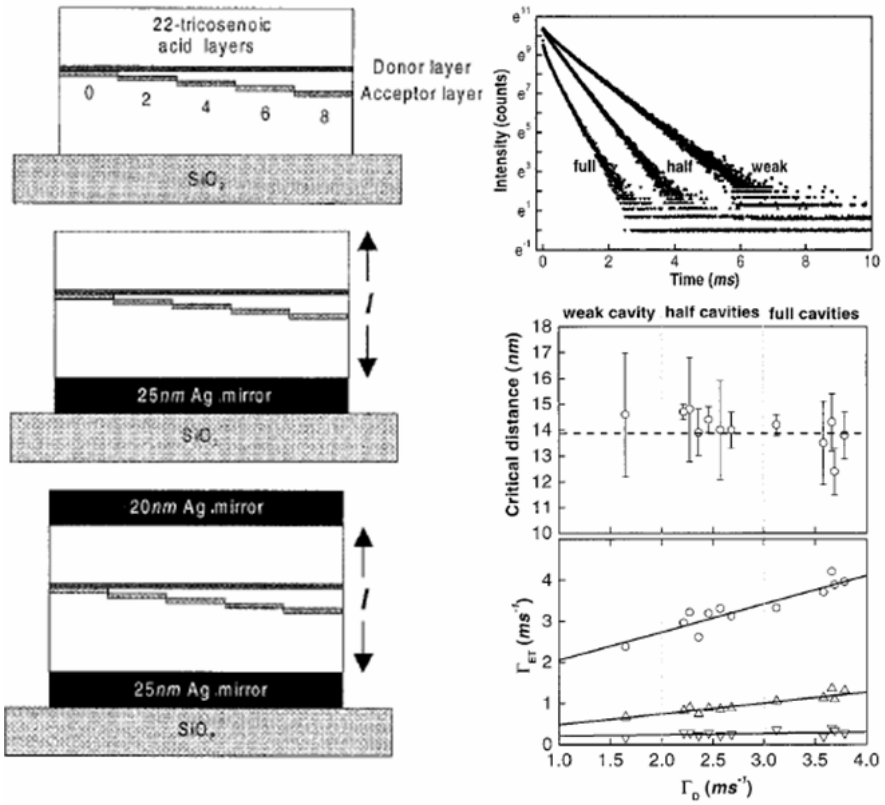

Figure 2.7 Energy transfer in optical cavity. Left from top to bottom: weak, half, and full cavities. Top right: Excited-state decays of the donor. Middle right: Förster radius predicted (dashed line) and measured (open circles) from the cavities. Bottom right: Dependence of energy transfer rate on donor emission rate in absence of acceptor with the donor and acceptor separated by four layers (O), six layers (Δ), and eight layers (V) of 22-tricosonic acids. Figure copied from Ref. 14.

(TPP), a value of R_o = 4.8 nm is obtained from spectral overlap calculations whereas excited-state lifetime measurements give a slightly smaller figure of 4.2 nm.[17] Although the greater R_o values observed in the PFO case was attributed to a greater spectral overlap between PFO and TPP as compared to that between Alq_3 and TPP, the discrepancy calls for some modifications in the approach to the model as applied to energy transfer in polymer blends.

In a number of publications, Bradley and co-workers addressed the deviations of experimental results from the Förster theory and suggested models based on point-surface and surface-surface dipole interactions for dye-polymer and polymer-polymer blends, respectively, instead of the point-point dipole interactions assumed in the theory.[18] From a study of the energy transfer in PFO-Nile Red blends, the measured data suggested an ET rate that is proportional to R^{-3} instead of R^{-6} as predicted by the Förster theory (**Figure 2.8a**).[18a] A modified rate expression based on point-surface dipole interaction was suggested (**Figure 2.8b**).

$$k_{ET} = \frac{\overline{R}_o^3}{\tau_d r^3} \qquad (2.12)$$

$$\text{with } \overline{R}_o^3 = \frac{\pi \rho R_o^6}{6} \qquad (2.13)$$

where $\overline{R}_o$ is the Förster radius for molecule-surface interaction and ρ is the donor chromophore density. When ρ is taken to be 0.14 nm^{-3} for PFO (estimated from monomer density), the modified Förster radius $\overline{R}_o$ was found to be 4.2 nm, which yields an R_o value of 3.2 nm. This figure is comparable to the number (3.6 nm) obtained from the spectral overlap integral, which confirms the observation of $k_{ET} \propto R^3$.

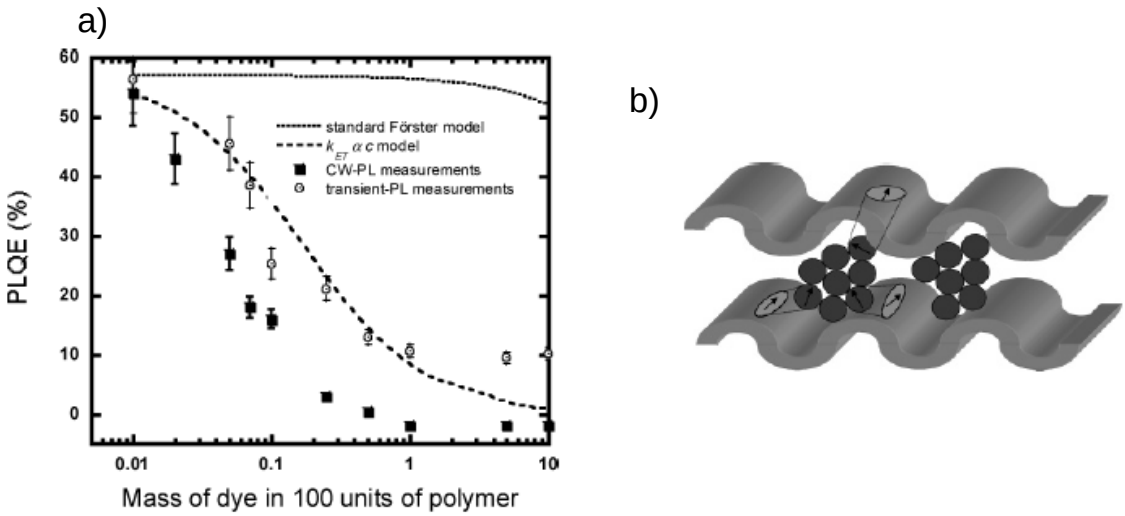

Figure 2.8 Deviation from Förster ET model (a) and representation of point-surface dipole interaction in dye-polymer blend (b). Figures copied from Ref. 18a.

Evidence of excitation energy migration before transfer is also observed by Bradley and co-workers in a study of the donor-acceptor blends composed of PFO and poly(9,9-dioctylfluorene-co-benzothiadiazole) (F8BT).[18b] Excited-state decay measurements at low temperature (12 K) revealed a two-step process that was reasoned to be an exciton migration step (~20 ps) followed by a Förster energy transfer step (~12 ps). The energy transfer behavior of this blend system was investigated further in LB structures (**Figure 2.9**) and the excited-state lifetimes measured at different spacer lengths pointed to an ET process with $k_{ET} \propto R^{-2}$, where R being the separation distance between the donor layer and the acceptor.[18d] This is, again, contradictory to the predicted behavior of $k_{ET} \propto R^{-6}$ by Förster for pointlike dipole interactions and $k_{ET} \propto R^{-4}$ by Kuhn for energy transfer between two planes.

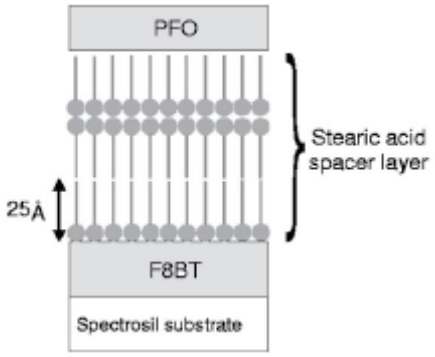

Figure 2.9 BL structured PFO-F8BT film. Figure copied from Ref. 18d.

In all these studies, a discrepancy between experimental data and theory caused by phase separation of the blend components was suspected. However, taking phase separation problem into an expression for energy transfer rate presents a great challenge, since the inhomogeneity of phase separation does not permit theoretical treatment from a viewpoint of density distribution. Likewise, a proper model for the rate of energy transfer in polymer-polymer blends has to take into account the distribution of the dipole moments of the donor and acceptor and their orientation with respect to one another.

2.4 References

[1] Burroughes, J. H., Bradley, D. D. C., Brown, A. R., Marks, R. N., MacKay, K., Friend, R. H., Burn, P. L., Holmes, A. B. *Nature* **1990**, *347*, 539.

[2] a) Tasch, S., Brandstäter, C., Meghdadi, F., Leising, G., Froyer, G., Athouel, L. *Adv. Mater.* **1997**, *9*, 33. b) Berggren, M., Dodabalapur, A., Slusher, R. E., Bao, Z. *Nature* **1997**, *389*, 466. c) Greenham, N. C., Moratti, S. C., Bradley, D. D. C., Friend, R. H.,

Holmes, A. B. *Nature* **1993**, *365*, 628. d) Veinot, J. G. C., Marks, T. J. *Acc. Chem. Res.* **2005**, *38*, 632.

[3] Alam, M. M., Jenekhe, S. A. *Macromol. Rapid Commun.* **2006**, *27*, 2053.

[4] Chen, L. McBranch, D. W., Wang, H., Helgeson, R., Wudl, F., Whitten, D. G. *Proc. Natl. Acad. Sci. U.S.A*. **1999**, *96*, 12287.

[5] O'Carroll, D., Lieberwirth, I., Redmond, G. *Nature Nanotechnology* **2007**, *2*, 180.

[6] Berggren, M., Inganäs, O., Gustafsson, G., Rasmusson, J., Anderson, M. R., Hjertberg, T., Wennerström, O. *Nature* **1994**, *372*, 444.

[7] a) Kaschak, D. M. *et al. J. Am. Chem. Soc.* **1999**, *121*, 3435. b) Kaschak, D. M., Mallouk, T. E. *J. Am. Chem. Soc.* **1996,** *118*, 4222.

[8] Fox, M. A. *Acc. Chem. Res*. **1999**, *32*, 201.

[9] Nguyen, T. Q., Wu, J., Doan, V., Schartz, B. J., Tolbert, S. H. *Science* **2000**, *288*, 652.

[10] Valeur, B. *Molecular Fluorescence*, Wiley-VCH Publishers, **2002**.

[11] a) Förster, T. *Ann. Phys.* **1948**, *2*, 55. b) Förster, T. *Disc. Farad. Soc.* **1959**, *27*, 7. c) Förster, T. Delocalized excitation and excitation transfer, in *Modern Quantum Chemistry, Part III*, ed. O. Sinanoglu, Academic Press, New York, **1965**, pp. 93–137.

[12] Laidler, K. J. and Meiser, J. H. *Physical Chemistry, 3rd edition.* Houghton Mifflin Company (Boston, MA), **1999**.

[13] a) Dexter, D. L. *J. Chem. Phys.* **1953**, *21*, 836. b) Naqvi, K. R. *J. Phys. Chem.* **1981**, *85*, 2303.

[14] Andrew, P. and Barnes, W. L. *Science* **2000**, *290*, 785.

[15] Kuhn, H. *J. Chem. Phys*. **1970**, *53*, 101.

[16] Shoustikov, A., You, Y., Burrows, P., Thompson, M. E. Forrest, S. R. *Synth. Met.* **1997**, *1*, 217.

[17] a) Virgili, T., Lidzey, D. G., Bradley, D. D. C. *Adv. Mater.* **2000**, *12*, 58. b) Cerullo, G., Stagira, S., Zavelani-Rossi, M., De Vilvestri, S., Virgili, T., Lidzey, D. G., Bradley, D. D. C. *Chem. Phys. Lett.* **2001**, *335*, 27.

[18] a) Cabanillas-Gonzalez, J., Fox, A. M., Hill, J., Bradley, D. D. C. *Chem. Mater.* **2004**, *16*, 4705. b) Buckley, A. R., Rahn, H. N., Hill, J., Cabanillas-Gonzalez, J., Fox, A. M., Bradley, D. D. C. *Chem. Phys. Lett.* **2001**, *339*, 331. c) Hill, J., Heriot, S. Y., Worsfold, O., Richadson, T. H, Fox, A. M. Bradley, D. D. C. *Synth. Met.* **2003**, *139*, 787. d) Hill, J., Heriot, S. Y., Worsfold, O., Richardson, T. H., Fox, A. M. *Phys. Rev. B* **2004**, *69*, 041303(R).

CHAPTER 3

INTRODUCTION TO PHASE SEPARATION IN FILMS OF CONJUGATED POLYMER BLENDS

3.1 Overview

Conjugated polymers, especially those containing aromatic or heterocyclic moieties, possess useful electronic, optoelectronic, and photonic properties that are being applied in various devices, including light-emitting diodes (LEDs),[1-3] photovoltaic cells (PVs),[4-5] thin film transistors,[6] and electrochromic cells.[7] Novel phenomena that arise from intermolecular interactions, self-organization, and confinement effects in blends of conjugated polymers are of fundamental and technological interest.[8] Moreover, changing the physical and optoelectronic properties of a system by blending different polymers is more economical in terms of chemical synthesis and material process. Recently, LEDs and PVs based on blends of conjugated polymers have been found to be more efficient compared to layer-by-layer deposition of homopolymers because the phase separation in thin films of the blends created nanosized self-assembled heterojunctions where exciton dissociation (in PVs) or charge recombination (in LEDs) were facilitated.[9] In order for blends of conjugated polymers to be developed into useful technological materials for electronics and photonics, a better understanding of the interactions in conjugated polymer blends such as ground-state charge transfer,[10] photoinduced charge transfer,[4] exciplex formation,[11] energy transfer,[9,12] enhanced charge transport,[13] and exciton

confinement[14] is necessary. Such an understanding in turn requires knowledge in the control of thin film morphology of conjugated polymer blends.

It is a well known phenomenon in polymer science that mixtures of dissimilar polymers often result in phase separation of the blended components due to the low entropy of mixing between different polymers.[8] While conjugated polymers are relatively novel materials and our understanding of the phase behavior in their blended films is still very poor,[8,12b] phase separation in films of "conventional" polymer blends, on the other hand, has been extensively studied in the past three decades from both theoretical and experimental viewpoints.[17-20] The morphology of thin films of polymer blends is determined by a host of competing non-equilibrium processes that include solvent evaporation, demixing, phase coarsening, local ordering, and, especially, surface dewetting.[8,12b] Since the first finding of a complete-partial wetting transition near a critical point of a linear mixture by Cahn in 1977,[21] the effect of wetting on phase separation has been intensively studied[22-25] as it was realized that an understanding of thin-film morphology of polymer blends would be of great important not only in fundamental areas of interest such as material transport, hydrodynamics, wetting and dewetting of material on a surface, surface segregation, and others, but also in practical applications of material processing, including thin-film coating, morphological control of nanomaterials, and composite materials.

As mentioned above, our understanding of surface wetting and phase separation phenomena has come mainly from studies of mixtures of non-conjugated amorphous polymers. Blends of conjugated polymers present a greater challenge as these materials can self-organize into crystalline structures due to their π-π interaction ability. Therefore,

the following discussion focuses on classical polymers only. Some observations on the phase separation behavior in thin films of semiconductor polymers will be presented subsequently.

3.2 Phase Separation Dynamics

Phase separation occurs because the materials (polymers or blends thereof) in a system (thin films) re-organize themselves in such a way as to minimize the overall free energy of the system. In the initial stage of phase separation, the surface layer formation process depends on how long it takes for the component with lower surface energy to diffuse to the surface (i.e., the substrate, which is assumed to be of a material different from those in the blends). The non-equilibrium mixture separates into phases having different energy of interaction with the surface in order to lower the total free energy. Thus at this stage, one is dealing with the surface wetting process where the growth of the wetting surface layer can be monitored by a depth-profiling technique, and the growth rate may be modeled as a function of diffusibility.[26] However, there is not only the energy cost of the interactions between the polymer(s) with the surface but also of the inter-phase and polymer-solvent interactions. Accordingly, at the onset of phase separation, hydrodynamic transport of materials enables each phase to segregate to minimize its surface of contact. The dynamics is complex but can be categorized into two phase separation behaviors: nucleation and growth and spinodal decomposition.[8, 27] In order to better follow these processes, a popular theory called the Flory-Huggins mean-field theory[28-31] is now presented.

Polymer-polymer phase behavior in equilibrium was theoretically studied decades before experimentalists had the technological means to obtain data for comparison. Conventionally, the study of thermodynamics of phase separation in a blend of polymers A and B begins with an approximation of the energy of mixing, represented by the Flory-Huggins segment-segment interaction parameter χ,[32]

$$\chi = \frac{1}{k_B T}\left[\varepsilon_{AB} - \frac{1}{2}\left(\varepsilon_{AA} + \varepsilon_{BB}\right)\right] \qquad (1)$$

where a segment is defined as a repeat unit or monomer, k_B is the Boltzmann's constant, and ε_{ij} represents the contact energy between the i and j segments. From Eq. 1, a favorable mixing is expected when χ is negative, that is, interaction between A and B results in a lower energy of the system compared to the combined A-A and B-B interactions. On the other hand, the overall energy of the system is increased when χ is positive, that is, mixing A and B is unfavorable. For most non-polar classical polymers such as polyethylene and polystyrene where interactions are via van der Waals force, the contact energy is represented by[32]

$$\varepsilon_{ij} = -\sum_{i,j} \frac{3}{4} \frac{I_i I_j}{I_i + I_j} \frac{\alpha_i \alpha_j}{r_{ij}^6} \qquad (2)$$

where r_{ij} is the segment-segment separation, and α and I are the polarizability and ionization potential, respectively. In mixtures where the individual components are

arranged randomly with no preferred segment orientation, there is no volume change and Eqs. 1 and 2 can be rewritten as

$$\chi = \frac{3}{16}\frac{I}{k_B T}\frac{z}{V^2}(\alpha_A - \alpha_B)^2 \qquad (3)$$

In this equation, a cubic lattice is assumed with $I_i = I_j = I$ and all contacts are neglected except for those from the z nearest-neighbor segments. The segment volume V is defined so that the number of segments per polymer molecule is $N = \rho VL/M$, where ρ and M are the density and molecular weight of the polymer, and L is the Avogadro's number.

The assumptions made in Eq. 3 cause significant deviations from experimental data because, in reality, most polymer mixtures have $\Delta V \neq 0$ due to some extent of anisotropic segment interactions. These effects are usually taken into account with an assumption that[33-34]

$$\chi = \alpha T^{-1} + \beta \qquad (4)$$

where α and β stand for experimentally determined enthalpy and excess entropy coefficients for a particular component. It can seen from Eq. 4 that if α is positive and β is negative, then decreasing T will increase χ, resulting in an upper critical solution temperature (UCST). Conversely, a negative α and a positive β will give rise to a lower critical solution (see below) temperature (LCST). These most simplified scenarios are illustrated in **Figure 3.1**. Experimentally, these behaviors have recently been observed

with critical mixtures of poly(vinyl methyl ether) and polystyrene displaying a LCST and those of poly(ethylene-propylene) and polyisoprene showing a UCST.[49,50]

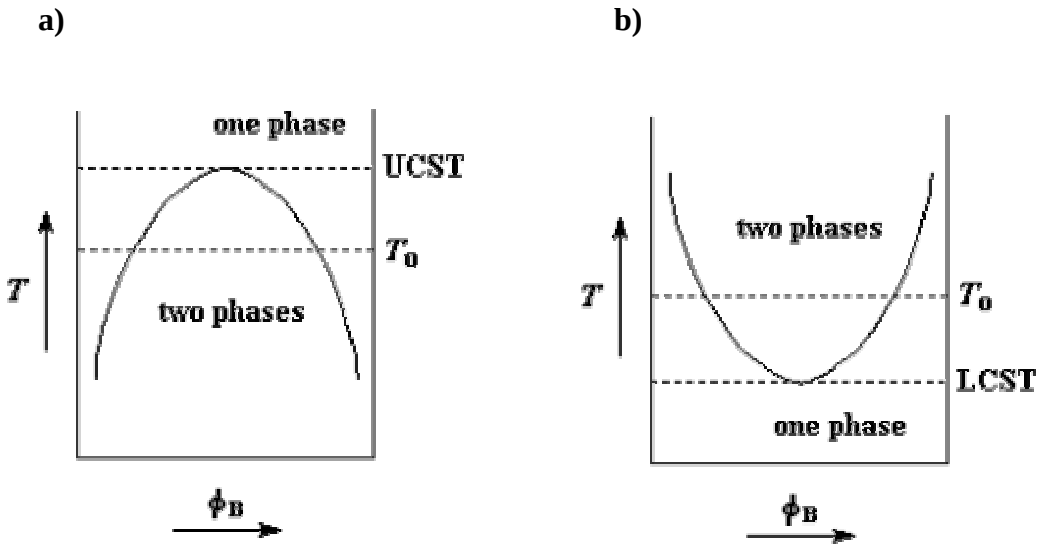

Figure 3.1 Illustrations of UCST and LCST.

Macroscopically, the behavior of a phase separation system in equilibrium is thermodynamically governed both by enthalpy ($H = U + PV$ with U, P, and V being the system energy, pressure, and volume, respectively) and entropy S that together determines the Gibbs free energy of the system.

$$G = H - TS \qquad (5)$$

We want to know how the free energy of the system is changed upon mixing two dissimilar polymers together. However, the analysis would be tremendously complicated if the system involves conjugated polymers which may crystallize or interact

anisotropically and thereby inhibit analysis by a mean-field approach. Thus Flory[28,29] and Huggins[30,31] dealt with the simplest case of polymer mixing—that of two classical linear homopolymers, and they independently estimated the change in free energy per segment ΔG_m in mixing random walk polymer chains on an incompressible lattice to be

$$\frac{\Delta G_m}{k_B T} = \frac{\phi_A}{N_A} \ln \phi_A + \frac{(1-\phi_A)}{N_B} \ln(1-\phi_A) + \phi_A (1-\phi_A) \chi \qquad (6)$$

where φ refers to the overall volume fraction of a component. (In an incompressible lattice, $\varphi_A + \varphi_B = 1$). This equation is a mean-field theory[35] with the first two and the third terms on the right represent the entropy ΔS_m and enthalpy ΔH_m of mixing, respectively. Under the assumed conditions, mixing tends to increase the entropy and so does the use of small N. The behavior of enthalpy depends on the sign of χ.

The dynamics of phase separation in a polymer blend system will be more easily studied with the help of a phase diagram, which can be constructed using the conditions at equilibrium, stability boundary, and critical point that are evaluated at constant temperature and pressure.[32,36]

$$\text{Equilibrium: } \frac{\partial \Delta G_m(\phi_A')}{\partial \phi_A} = \frac{\partial \Delta G_m(\phi_A'')}{\partial \phi_A} \qquad (7)$$

$$\text{Stability: } \frac{\partial^2 \Delta G_m}{\partial \phi_A^2} = 0 \qquad (8)$$

$$\text{Criticality: } \frac{\partial^3 \Delta G_m}{\partial \phi_A^3} = 0 \qquad (9)$$

where the superscripts refer to different phases. In the case where $N_A = N_B = N$, the theroretical phase diagram is represented in **Figure 3.2**.

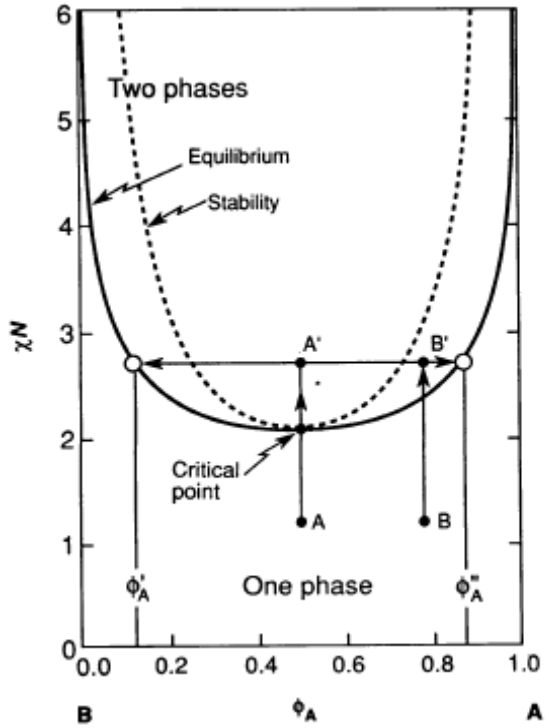

Figure 3.2 Theoretical phase diagram for a symmetric binary mixture of linear homopolymers. (Figure copied form Ref. 27).

The composition and segment-segment interaction at the critical point can be found by combining Eqs. 8 and 9 to yield

$$\phi_c = \frac{N_A^{1/2}}{N_A^{1/2} + N_B^{1/2}} \tag{10}$$

and

$$\chi_c = \frac{(N_A^{1/2} + N_B^{1/2})}{2N_A N_B} \tag{11}$$

Using the theoretical phase diagram, the phase-separation dynamics can be predicted as follows. If a homogenous mixture is brought to the metastable region, such as from point B to B' in **Figure 3.2**, a minority phase will develop via nucleation and growth (**Figure 3.3**) as predicted by classical nucleation theory.[37] The initial small droplets grow larger from the diffusion of material from the supersaturated medium and, once the composition of the supernatant reaches equilibrium with $\phi_A^{"}$, they continue to grow by coalescence as, at this stage, growth by diffusion is extremely limited by the viscosity of the polymers. In this mode of phase separation, the polymer mixture in the metastable region has to overcome the free energy barrier in order to form a new phase.

In the second scenario where a homogenous mixture is brought into an unstable region such as from point A to A' in the phase diagram, a free energy barrier is absent and the mixture spontaneously separates into a bicontinuous two-phase structure (**Figure 3.4**) in a process termed spinodal decomposition.[38] As in the case of phase separation by nucleation and growth where the initial droplets grow larger in order to reduce interfacial area (which in turn minimizes interfacial surface tension), the features resulted from spinodal phase separation continue to grow by coarsening in an effort to lower the interfacial area while maintaining the bicontinuous morphology.

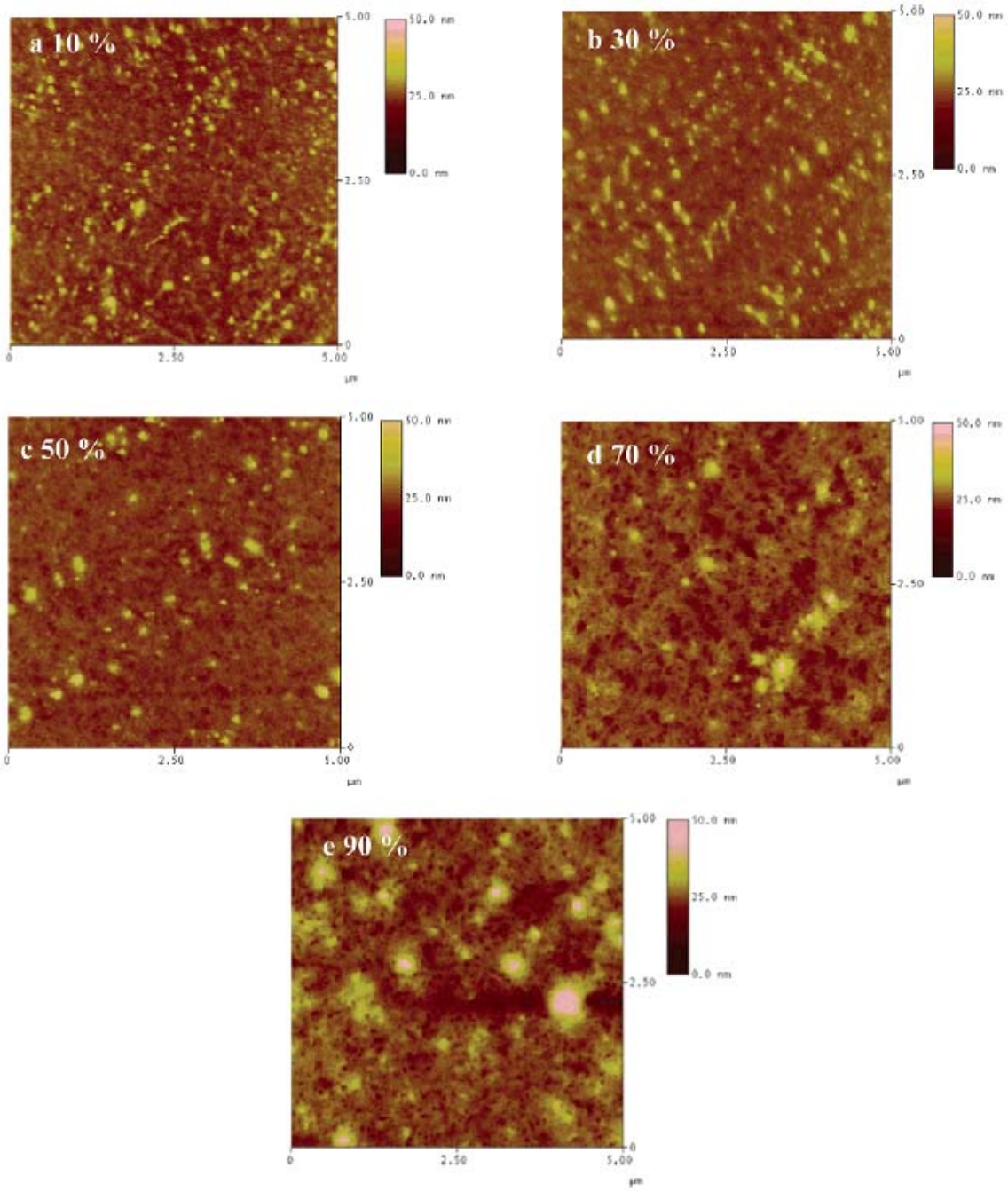

Figure 3.3 AFM tapping mode topographic images of spin-coated thin films of PFO/P3HT blends showing phase separation by nucleation and growth mechanism. (the percents refer to PFO with respect to P3HT). Figure copied form Ref. 51.

Ultimately in thin films of polymer blends, interfacial interaction energy plays a vital role in the stability of the films. From Young's equation for the spreading coefficient,[39]

$$S = \gamma_B - (\gamma_{AB} + \gamma_A) \qquad (12)$$

where γ_A, γ_B, and γ_{AB} stand for surface energies of the polymer film, substrate, and film-substrate interface, respectively, it could be inferred that the film will be unstable if the coefficient *S* is negative. In terms of molecular interaction, polymer films break up in

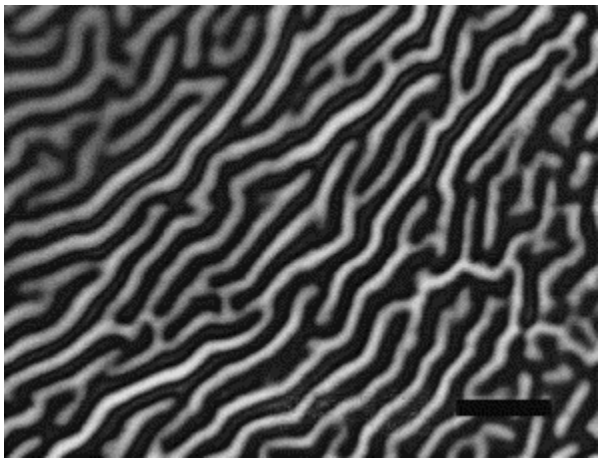

Figure 3.4 Optical micrograph of a freestanding PS film capped by evaporated SiO_2 after annealing at 483 K for 3 hours showing spinodal phase separation. Figure copied from Ref. 52.

spinodal decomposition because long-range van der Waals forces cause an amplification of film thickness fluctuations. This may sound counter-intuitive, but if the interaction

with the surrounding medium is greater from the substrate than from the film, the surface tension will destabilize the film.[21,38]

3.3 Phase Separation in Films of Conjugated Polymer Blends

Theoretical and experimental studies of phase separation in thin films of polymer blends have focused mainly on simple polymers. However, progress is being made in the areas of conjugated polymers in solid state although the main interest lies in the device performance rather than on critical analysis of thin-film morphology.[8,40] A

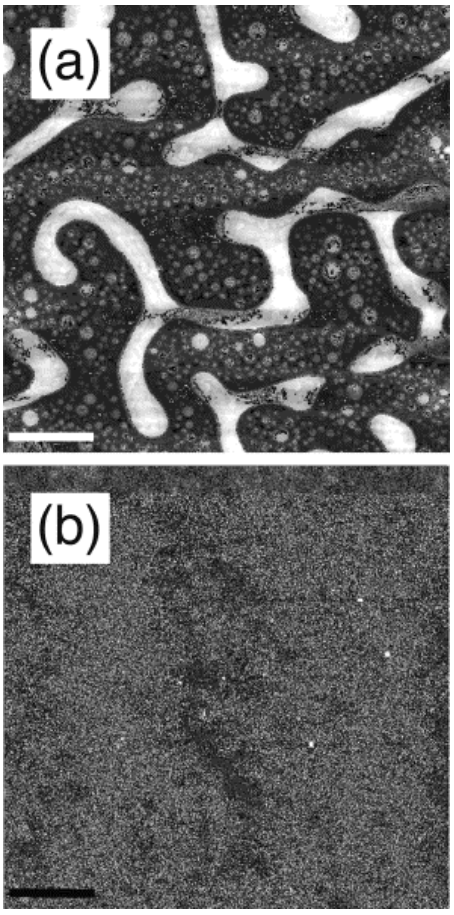

Figure 3.5 Scanning force micrographs of PFB[53]/F8BT blend films spun from xylene (a) and chloroform (b). Scale bar for both images is 10 μm. Figure copied from Ref. 54.

technologically important blend is poly(styrene sulphonic acid) (PSS) and poly(3,4-ethylene dioxythiophene) (PEDOT) has recently been studied with neutron reflectometry to obtain surface composition profile on thin-film structures.[41] One of the efforts to correlate thin-film morphology with device performance was taken by Friend and co-workers who fabricated photovoltaic cells with blends of the light-emitting alternating coplymers containing poly(9,9-dioctylfluorene) (PFO) and found the device performance

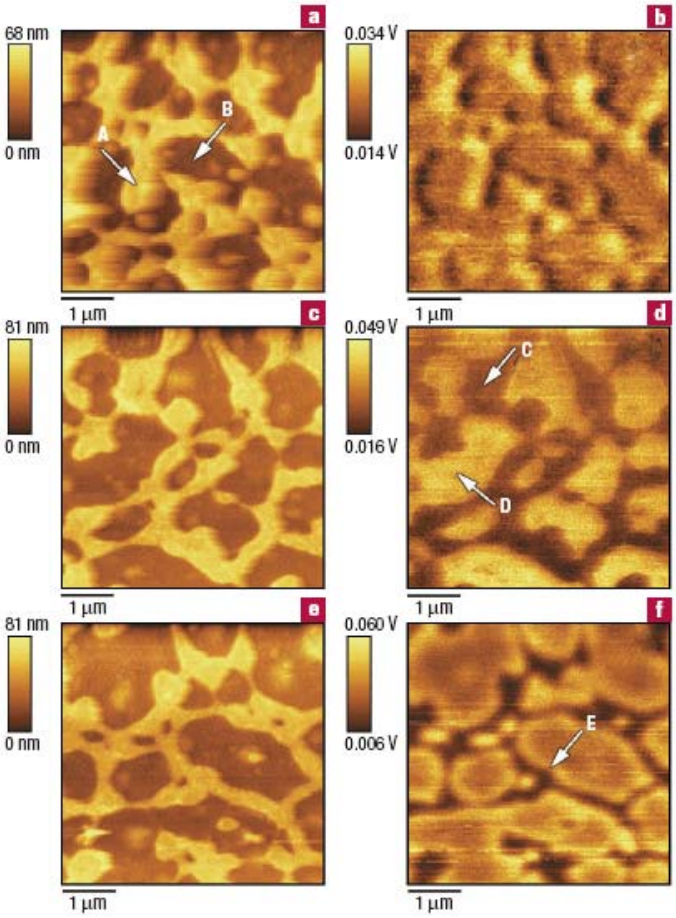

Figure 3.6 SNOM images of the transmission and fluorescence from a PFO/P8BT blend. (Images taken from different areas of the same 1:1 blend ratio sample). Figure copied from Ref. 12.

to be better when the phase separation was in short length scale.[42,43] These studies also show that thin films of the blends spun cast from different solvents display different phase-separation morphologies (**Figure 3.5**).

Since many of the semiconducting polymers are emitters of visible light, a particularly useful technique to study thin-film morphology is scanning near-field optical microscopy (SNOM). Several groups have used SNOM to study the morphology of phase-separated thin films of light-emitting polymers by exciting different areas of the thin films with light of appropriate wavelength and observing the resulting fluorescence (**Figure 3.6)**.[44-48] An example of this approach is from a study by Jones and others who used SNOM to investigate component distribution a cross the surface of spun cast thin film of a polymer blend comprised of PFO and poly(9,9-dioctylfluorene-*alt*-benzothiadiazole) (F8BT).[12] The researchers also employed ^{3}He nuclear-reaction analysis (NRA) to obtain a depth profile of the film and concluded that PFO preferentially formed a thin surface-wetting layer while F8BT diffused away from the substrate and phase separated via spinodal dewetting (**Figure 3.7**). It may be expected that the experimental data being accumulated in this area of intense research will soon enable the formulation of a theoretical model that can cope with such challenging problem as entropic fluctuations in thin films of conjugated polymers due to crystallization and local ordering.

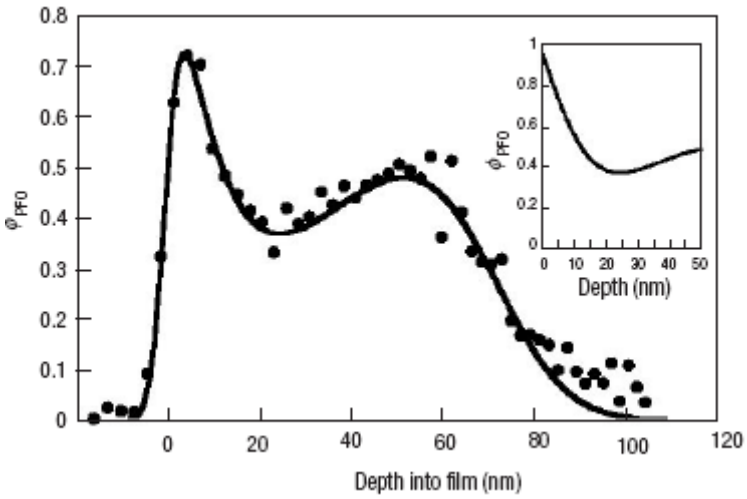

Figure 3.7 Depth Profile by ^{3}He NRA showing the distribution of PFO in PFO/P8BT blend film as a function of film depth. (Figure copied from Ref. 12).

3.4 References

[1] Friend, R. H., Gymer, R. W., Holmes, A. B., Burroughes, J. H., Marks, R. N., Taliani, C., Bradley, D. D. C., Dos Santos, D. A., Bredas, J. L., Logdlund, M., Salaneck, W. R. *Nature* **1999**, *397*, 121.

[2] a) Heeger, A. J. *Angew. Chem. Int. Ed*. **2001**, *40*, 2591. b) MacDiarmid, A. G. *Angew. Chem. Int. Ed.* **2001**, *40*, 2581.

[3] Bernius, M. T., Inbasekaran, M., O'brien, J., Wu, W. *Adv. Mater*. **2000**, *12*, 1737.

[4] a) Halls, J. J. M., Walsh, C. A., Greenham, N. C., Marseglia, E. A., Friend, R. H., Moratti, S. C., Holmes, A. B. *Nature* **1995**, *376*, 498. b) Arias, A. C., MacKenzie, J. D.,

Stevenson, R., Halls, J. J. M., Inbasekaran, M., Woo, E. P., Richards, D., Friend, R. H. *Macromolecules* **2001**, *34*, 6005.

[5] Sariciftci, N. S. *Curr. Opin. Solid-State Mater. Sci***. 1999**, *4*, 373.

[6] a) Sirringhaus, H., Tessler, N., Friend, R. H. *Science* **1998**, *280*, 1741. b)

[7] a) Sapp, S. A., Sotzing, G. A., Reynolds, J. R. *Chem. Mater*. **1998***, 10*, 2101. b)

[8] Geoghegan, M., Krausch, G. *Pro. Polym. Sci*. **2003**, *28*, 261-302.

[9] Cadby, A., Dean, R., Jones, R. A. L., Lidzey, D. G. *Adv. Mater*. **2006**, *18*, 2713-2719.

[10] Chen, X. L., Jenekhe, S. A. *Macromolecules* **1997**, *30*, 1728.

[11] a) Gebler, D. D., Wang, Y. Z., Blatchford, J. W., Jessen, S. W., Fu, D. K., Swager, T. M., MacDiarmid, A. G., Epstein, A. J. *Appl. Phys. Lett***. 1997***, 70*, 1644. b) Jenekhe, S. A., Osaheni, J. A. *Science* **1994**, *265*, 765. c) Alam, M. M., Jenekhe, S. A., *J. Phys. Chem. B* **2001**, *105*, 2479

[12] a) Berggren, M., Inganas, O., Gustafsson, G., Rasmusson, J., Andersson, M. R., Hjertberg, T., Wennerstrom, O. *Nature* **1994**, *372*, 444. b) Campbell, J., Lidzey, D. G., Jukes, P. C., Higgins, A. M., Thopmson, R. L., O'Connor, S., Grizzi, I., Fletcher, R., O'Brien, J., Geoghegan, M., Jones, R. A. L. *Nature Materials* **2003**, *2*, 616-621.

[13] a) Babel, A., Jenekhe, S. A., *J. Phys. Chem. B* **2002**, *106*, 6129. b) Babel, A., Jenekhe, S. A., *J. Phys. Chem. B* **2003**, *107*, 1749.

[14] a) Deussen, M., Scheidler, M., Bassler, H. *Synth. Met*. **1995**, *73*, 123. b) Zhang, X., Kale, D. M., Jenekhe, S. A. *Macromolecules* **2002**, *35*, 382.

[17] Gunton, J. D., San Miguel, M., Sahni, P. *Phase Transitions and Critical Phenomena;* Vol 8, ed C. Domb and J. L. Lebowitz (London: Academic), **1983**.

[18] Bray, A. J. *Adv. Phys***. 1994**, *43*, 357.

[19] Schmidt, I., Binder, K. *J. Phys*. **1985**, *46,* 1631-1644.

[20] Nakanishi, H., Pincus, P. *J. Chem. Phys*. **1983**, *79*, 997-1003.

[21] Cahn, J. W. *J. Chem. Phys*. **1977**, *66*, 3667-3672.

[22] Jasnow, D. *Rep. Prog. Phys*. **1984,** *47*, 1059

[23] de Gennes, P. G. *Rev. Mod. Phys*. **1985**, *57*, 827.

[24] Rysz, J., Budkowski, A., Bernasik, A., Klein, J., Kowalski, K., Jedlinski, J., Fetters, L. J. *Europhys. Lett*. **2000**, *50*, 35-40.

[25] Geoghegan, M., Ermer, H., Jüngst, G., Krausch, G., Brenn, R. *Phys. Rev. E* **2000**, *62*, 940-950.

[26] Jones, R. A. L., Kramer, E. J. *Phil. Mag. B* **1990**, *62*, 129-137.

[27] Bates, F. S. *Science* **1991**, *251*, 898-904.

[28] Flory, P. J. *J. Chem. Phys*. **1942**, *10*, 51.

[29] Flory, P. J. *J. Chem. Phys* **1944**, *12*, 425.

[30] Huggins, M. L. *Ann. N.Y. Acad. Sci.* **1942**, *43*, 1.

[31] Huggins, M. L. *J. Am. Chem. Soc.* **1942**, *64*, 1712.

[32] de Gennes, P. –G. *Scaling Concepts in Polymer Physics* (Cornell Univ. Press, Ithaca, NY), **1979**.

[33] Flory, P. J. *J. Am. Chem. Soc.* **1965**, *87*, 1833.

[34] McMaster, L. P. *Macromolecules* **1973**, *6*, 760.

[35] Let a represents the length of a segment in a polymer molecule, then the radius-of-gyration is defined as $R_g = a(N/6)^{1/2}$ with N being the number of segments per molecule. Thus a single molecular volume, estimated as $(4/3)\pi R_g^3$, contains a lot more than one

polymer chain and the segment-segment interactions can be safely averaged as long as there are no composition fluctuations in a range beyond R_g.

[36] Flory, P. J. *Principles of Polymer Chemistry* (Cornell Univ. Press, Ithaca, NY), **1953**.

[37] Abraham, F. F. *Homogeneous Nucleation Theory* (Academic, NY), **1974**.

[38] Cahn, J. W. *J. Chem. Phys.* **1965**, *42*, 93.

[39] Young, T. *Phil. Trans. R. Soc. Lond.* **1805**, *95*, 65-87.

[40] Moons, E. *J. Phys: Condens. Matter* **2002**, *14*, 12235-12260.

[41] Jukes, P. C. *Grazing Incidence X-ray Diffraction and Neutron Reflection Studies of Semi-crystalline Polymer Surfaces and Interfaces*. Ph.D. Thesis. University of Sheffield, 2002.

[42] Arias, A. C., MacKenzie, J. D., Stevenson, R., Halls, J. J. M., Inbasekaran, M., Woo, E. P., Richards, D., Friend, R. H. *Macromolecules* **2001**, *34*, 6005-60013.

[43] Aria, A. C., Corcoran, N., Banach, M., Friend, R. H., MacKenzie, J. D., Huck, W. T. S. *Appl. Phys. Lett.* **2002,** *80*, 1695-1697.

[44] Wei, P. K., Hsu, J. H., Fann, W. S. *Synth. Met*. **1999**, *102*, 1209-1210.

[45] DeAro, J. A. Weston, K. D., Buratto, S. K., Lemmer, U. *Chem. Phys. Lett.* **1997**, *277*, 532-538.

[46] Chappell, J., Lidzey, D. G. *J. Microsc.* **2003**, *209*, 188-193.

[47] Webster, S., Smith, D. A., Barchelder, D. N., Lidzey, D. G., Bradley, D. D. C. *Ultramicroscopy* **1998**, *71*, 275-279.

[48] Stevenson, R., Granström, M., Richards, D. *Appl. Phys. Lett.* **1999**, *75*, 1574-1576.

[49] Schwahn, D., Mortensen, K., Yee-Madeira, Y. *Phys. Rev. Lett*. **1987**, *58*, 1544.

[50] Bates, F. S. *et al*., *Phys. Rev. Lett*. **1990**, *65*, 1893.

[51] Babel, A., Jenekhe, S. A. *Macromolecules* **2003**, *36*, 7759-7764.

[52] Dalnoki-Veress, K., Nickel, B. G., Dutcher, J. R. *Phys. Rev. Lett.* **1999**, *82*, 1486-1489.

[53] PFB = poly(9,9-dioctylfluorene-*alt*-bis-N,N'-(4-butylphenyl)-bis-N,N'-phenyl-1,4-phenylenediamine).

[54] Arias, A. C. *Conjugated polymer phase separation and three-dimensional thin-film structure for photovoltaics*. Ph.D. Thesis. University of Cambridge, 2001.

CHAPTER 4

BLENDS OF POLYDIOCTYLFLUORENE (PFO) WITH POLYMERIC AND MONOMERIC ENERGY ACCEPTORS: CORRELATION OF FLUORESCENCE ENERGY TRANSFER AND FILM MORPHOLOGY IN BREATH FIGURES AND FILMS

4.1 Introduction

Light-emitting conjugated polymers are under intensive study for their potential applications in optoelectronics, printing, sensors, and other areas of advanced technology.[1-6] The polymers that have been receiving most attention include derivatives of poly(9,9-dialkylfluorene) (PFs), soluble derivatives of poly(phenylene vinylene) (PPVs), and various poly(alkylthiophene) (PTs). These polymers, now commercially available, are highly soluble in common organic solvents and therefore are attractive for solution-processed fabrications of electronic and photonic devices.[1-9] Moreover, most PFs and PPVs are efficient visible light emitters with high quantum yields (more than 50% for PFO and 15% for MEH-PPV) and being considered for photodiode and photovoltaic applications.[10-15] Polythiophenes, although having low quantum yield, have been found to have high field-effect mobility of holes.[16,17]

This study investigated film morphology and energy transfer efficiency of three different systems of donor-acceptor blends: (1) poly(9,9-dioctylfluorene) (PFO) and poly(3-hexylthiophene) (P3HT), (2) PFO and poly(2-methoxy-5(2'-ethylhexyloxy)-1,4-

phenylenevinylene) (MEH-PPV), and (3) PFO and *meso*-tetraphenylporphyrin (TPP). These materials were chosen for this study because their properties are well established, because significant overlap of PFO emission and each acceptor absorption facilitates energy transfer, emissions from the acceptors (i.e., red) are well resolved from that of the donor (i.e., blue), and because of their importance in potential technological applications.

The chemical and physical properties, as well as photophysics, of the polymers PFO, MEH-PPV, P3HT, and the red dye TPP whose structures are shown in **Figure 4.1** are relatively well characterized.[1,18-21] The blue-emitting PFO is currently attracting great attention due to its stability, high solid-state fluorescence quantum yield, and hole-transport capability with hole mobility approaching 10^{-3} $cm^2/(V\ s)$ at room temperature.[22] However, applications based on PFO such as LEDs and PVs are somewhat discouraged by its solid-state behavior due to its different crystalline forms. Depending on processing parameters such as temperature and solvent, PFO has been found to display a mesomorphic β phase, a crystalline α phase, and a closely related low-temperature crystallization α' phase.[23] These assignments of PFO crystalline phases by Su and co-workers are contradictory to those reported by many others who found the formation of a "crystalline" β phase when PFO was processed from toluene and an "amorphous" α phase in samples prepared from chloroform.[24-30] Jenekhe and co-workers take advantage of the phase separation-by-crystallization behavior of PFO to prepare quite efficient white-light electroluminescence devices from blends with the orange-red emitter MEH-PPV. They find PFO forming phase-separated crystalline domains that retard energy transfer to MEH-PPV in blended samples having less than 30% MEH-PPV and resulting in an overall white-light emission whereas samples with higher percents of MEH-PPV are

more amorphous and homogeneous with efficient energy transfer from PFO to MEH-PPV that leads to exclusive orange-red electroluminescence.[31] Like PFO, MEH-

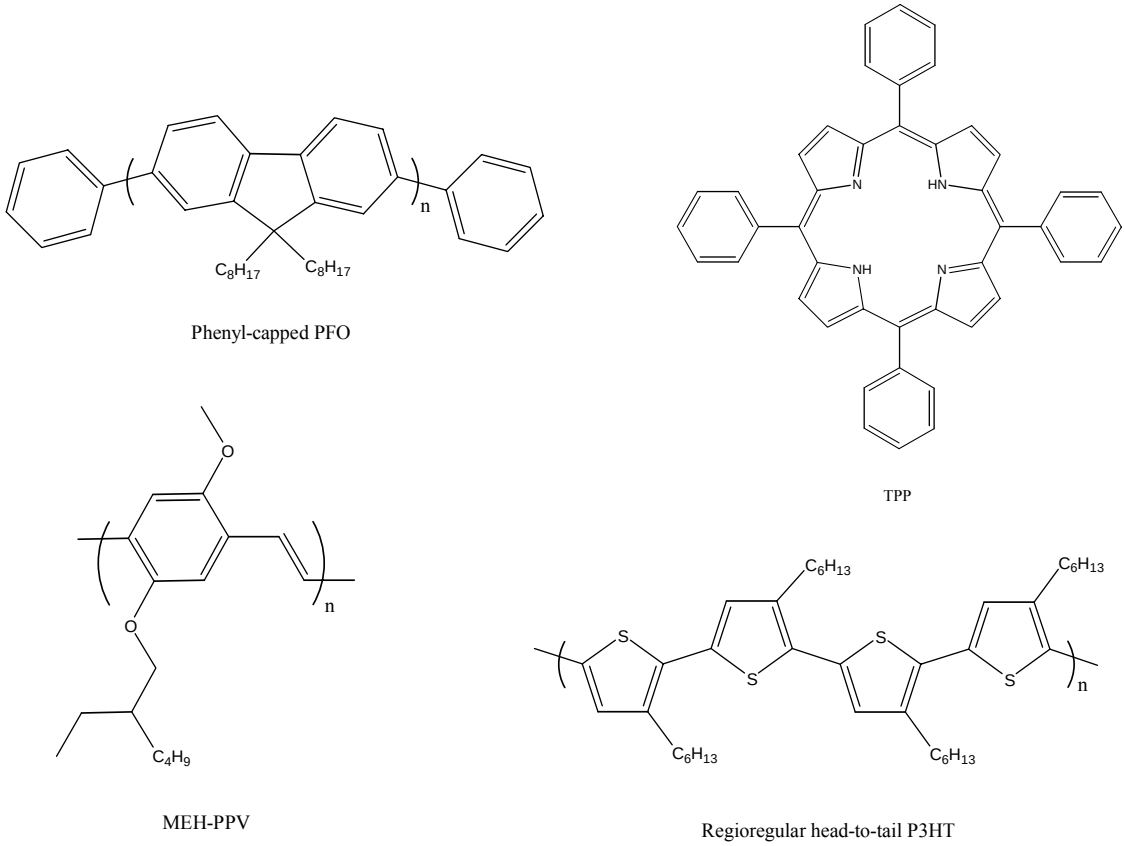

Figure 4.1 Chemical structures of the polymers and dye.

PPV is an efficient fluorescence emitter with higher than 15% quantum yield and soluble in many organic solvents. However, in the solid state, MEH-PPV tends to be amorphous, probably because of its more mobile alkoxy groups.

Another setback to the use of PFO for optoelectronic applications is due to its significant green emission that is usually assumed to come from the formation of aggregates, interchain excimers, or keto defects due to oxidative degradation.[32-35] Many attempts have been made to circumvent this problem by installing different end-groups[36] and/or attaching longer alkyl chains at the C-9 position of fluorene core.[37,38]

Regioregular P3HT attracts research interest mainly for its high hole mobility, comparable to α-Si.[16] Thin-film transistors using semiconducting polymers as the electron/hole transport materials are of immense interest for industrial and academic research alike because these devices can be fabricated at a much lower processing cost than the silicon-based analogues. Moreover, the electronic and photonic properties of polymers can be tuned simply by synthesis. Despite the low quantum yield in their solid-state fluorescence, P3HT and other polythiophenes have many interesting and useful photophysical properties.[1] In the case of regioregular P3HT, analysis of its optical absorption and fluorescence is complicated by intrachain and interchain interactions that ultimately depend on how the polymer chains align with respect to each other in the solid state.[39,40] Recently, blends of P3HT and PFO were employed to fabricate thin-film transistors and hole mobility of PFO was extrapolated from the measurements of the device performance.[41] The authors also reported their observation of fluorescence energy transfer and phase separation but did not attempt to understand these processes.

Besides polymer-polymer blends, this study also included the red dye TPP as an energy acceptor. There have been a few reports on the use of PFO-TPP blends for LEDs that show promising device performance.[19,21] Although the absorption of TPP at the emission wavelengths of PFO is rather small, energy transfer in the blended thin films shifts the blue emission of PFO to a structured red emission peak of TPP with enhanced photoluminescence of the latter. Moreover, unlike the case of polymer-polymer blends, for which Förster-type analysis is almost impossible due to complications in dipole-dipole interactions, the Förster radius can be calculated in polymer-dye blends. However, deviations still occur due to the assumptions made in the distribution of the polarity of the

polymer chains with respect to the point-like dipole of TPP.[19,21] Since macromolecular dyes such as TPP are potentially useful in photosensitized solar cell applications, their deployment as a dopant in a polymer matrix with high surface area such as in the microstructured surfaces prepared by the breath figure method may be relevant to the technological advances in the near future.

It would be interesting to observe the phase separation behavior of polymer-polymer and polymer-dye blends when they are cast into microstructured films by the breath figure (BF) method. This study was designed to do just that. As shown later in this chapter, the fast solvent evaporation rate in the bubble-forming process coupled with hydrodynamics and surface segregation[42] significantly alters the phase separation morphology of the films with surface bubble arrays compared to the films prepared by drop casting (DC). The film morphology is found to be dependent not only on the film-forming process but also on the solvents used to prepare them. A correlation of film morphology and energy transfer efficiency is investigated to reveal the distribution of components in different film structures of the blends.

4.2 Experimental

The breath figure method (see Chapter 1) was used to prepare bubble arrays of blends of PFO:MEH-PPV, PFO-P3HT, and PFO-TPP from CS_2 and $CHCl_3$ solutions as these solvents were found to facilitate the formation of the breath figure arrays (BFAs). Drop-coated films (DCFs) of these blends were also prepared from the same solvents.

The two sets of samples were studied for their morphology and fluorescence energy transfer.

4.2.1 Materials:

Phenyl-capped PFO of varying molecular weights were synthesized and kindly provided as a gift by the group of Professor Ulrich Scherf of Bergische Universität Wuppertal in Germany. Unless stated otherwise, the PFO employed in this study had M_n of 12,900 g/mol and M_w of 29,600 g/mol. MEH-PPV (average M_n 40,000-70,000 g/mol) and TPP (greater than 99.0% purity) were obtained from Aldrich. Regioregular P3HT (average M_w 87,000 g/mol, mp 230^{o}C) was purchased from Aldrich. These materials were stored in the dark and used without further purification. The synthesis of these chemicals are well known and widely reported in the literature.[43-46] Anhydrous carbon disulfide (Aldrich) and chloroform (Fisher Scientific) were used as received.

4.2.2 Sample preparation:

Samples of breath figures and drop-coated films were prepared in triplicates. For the preparation of polymeric bubble arrays, individual solutions of PFO, MEH-PPV, P3HT, and TPP in CS_2 and $CHCl_3$ were prepared. All concentrations were in weight percent with PFO in 0.4% solutions and the acceptors in 0.02% solutions. For polymer-polymer blends, samples were prepared and diluted with the same solvent in order to obtain similar overall final polymer concentrations, which depend on the molecular weight of PFO as discussed later. In the case of PFO-TPP blends, the final concentrations of the mixtures in each run all had the same PFO concentration. Each blend sample was prepared immediately before the production of breath figure structures, which involved the placement of a cover glass that contained a 30-μl drop of a mixture in a humidity-

controlled chamber and the solvent was allowed to evaporate under a flow of moist air. Housed in Professor Mohan Srinivasarao's laboratory at Georgia Institute of Technology, the humidity chamber is attached to a Caron 5037 airflow-circulator and a Dayton Speed control. After the solvent had evaporated (usually in about 10 seconds for CS_2 and 30 seconds for $CHCl_3$), the cover glass was removed from the chamber and allowed to dry under ambient conditions. All samples were prepared at room temperature (25 ^oC) with a relative humidity of 85% and an airflow speed set at 50 on the Dayton airflow controller.

Drop-coated samples were prepared from the same solutions that were used in the preparation of the BFAs above. Thus in a glovebox with limited air circulation current, a 50-µl drop of each mixture was placed on a cover glass and allowed to dry over several minutes.

4.2.3 Methods of characterization

The surface morphology of the drop-coated films and the breath-figure structured films were studied with an Olympus BX60 microscope equipped with a CRAIC-upgraded SEE 1000 spectrophotometer in Professor Mohan Srinivasarao's laboratory at Georgia Institute of Technology. This fluorescence microscope allows the observation of the fluorescence from the samples as they are excited with light from a laser source.

Surface morphology was further characterized with atomic force microscopy (AFM) and scanning electron microscopy (SEM). A Veeco AFM, located in Microelectronic Research Center (MiRC) at Georgia Institute of Technology, was employed in tapping mode with µmasch-produced NSC 16 tips. A Zeiss Ultra 60 SEM, also located in the MiRC, was used to observe the morphology of the breath-figure structured films that had been coated with a thin layer of gold prior to measurements.

The morphological properties of the blended samples were also investigated with X-ray diffractometry (XRD) using a Scintag X1 Advanced Diffraction System in Professor Angus Wilkinson's laboratory (Georgia Institute of Technology) with CuKa radiation (l = 1.54056 Å). Samples were placed in aluminum plates (2x2 cm) and data were collected in an angular range of $2\theta = 1^{o}$ to 30^{o}, where θ represents the angle of incidence.

The absorption spectra of the blended films were recorded using a Perkin-Elmer Lambda 19 UV/VIS/NIR spectrometer using transmission mode while the fluorescence emissions of the samples were measured with Spex Fluorolog 2 series spectrofluorometer. The excitation light source of the fluorometer came from a xenon lamp whose absorption maximum is at 467 nm. The fluorometer was also equipped with an RCA C 31034 photomultiplier detector. The fluorescence emissions from the prepared films were measured at an angle with respect to the incident beam and all slits were maintained at 0.5 mm. For each sample, two to four measurements were made at different areas of the sample. Each fluorescence spectrum is presented as an average of a triplicate.

Excited-state fluorescence lifetimes of the samples were studied with a Lifespec-ps manufactured by Edinburgh Instruments. This instrument, located in Professor Robert Dickson's laboratory at Georgia Institute of Technology, operates with a Hamamatsu's MCP-PMT detector and a 372 nm PicoQuant GmbH pulsed diode laser as light source (model # LDH-P-C-375). The laser source was controlled with a PDL 800-B driver and the repetition frequency was kept at 20 MHz. Decay rates were monitored in 0.50 nm increment at 466 nm, which corresponds to the second emission peak of PFO.

4.3 Breath figures of PFO and polymer-polymer and polymer-dye blends

As mentioned in Chapter 1, successful formation of polymeric surfaces decorated with ordered open air bubble arrays depends on a number of factors, and viscosity seems to play a major role. As shown in **Figure 4.2**, when a PFO polymer with M_n of 12,900 g/mol was used, a PFO concentration of 1.0 wt% in CS_2 enabled the production of close-packed hexagonally ordered arrays of air bubbles while samples cast from more concentrated solutions resulted in disordered bubble arrays or no bubbles at all. Samples of high molecular weight had to be diluted in order to prepare bubble arrays of acceptable quality. For example, breath figure arrays (BFAs) of good quality were fabricated from a 0.7 wt% solution of PFO with M_n of 23,000 g/mol in CS_2. Similarly, when M_n was increased to 65,400 g/mol, the concentration had to be lowered to 0.2 wt% to facilitate the formation of BFAs. The relationship between PFO molecular weight and the formation of BFAs is not always straightforward as bubble arrays of excellent quality were successfully prepared from 1.0% and 0.2% solutions of PFO with M_n of 12,900 g/mol in CS_2 as shown in **Figure 4.2a&b**. It is noteworthy that well-ordered BFAs were not formed on an entire film surface but came in patches that are separated by regions of disordered bubble arrays. Perhaps, the dynamics of bubble formation redistributes the polymer concentration and results in regions having a viscosity that enables the breath figure formation as well as areas where the polymer concentrations do not support the creation of BFAs.

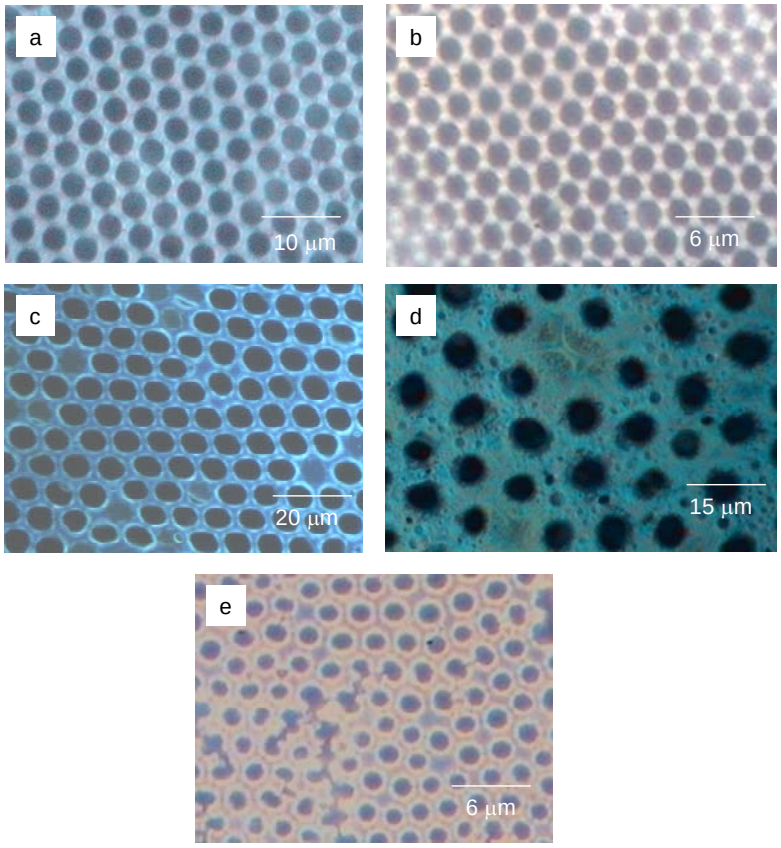

Figure 4.2 Dependence of breath figure bubble array formation on PFO molecular weight and concentration. M_n and [PFO] are: 12.9 kg/mol, 1.0% in CS_2 (a), 12.9 kg/mol, 0.2% in CS_2 (b), 23.0 kg/mol, 0.7% in CS_2 (c) 65.4 kg/mol, 0.2% in CS_2 (d), 12.9 kg/mol, 0.2% in $CHCl_3$ (e). (Optical micrographs with false colors).

Bubble arrays of PFO were not only generated from solutions in CS_2 but also from those prepared in $CHCl_3$ (**Figure 4.2e**). However, the films prepared from chloroform solutions often fractured visibly during the solvent evaporation process. The reason for the film rupture is not clear although the slower rate of evaporation of $CHCl_3$ appears to exert an impact. Observations made during the breath figure formation process reveal that, in areas where ordered water droplets have formed and little solvent has evaporated, the film that sustains the water droplets appears to swell up but subsequently

relax as more solvent evaporates. It is likely that the strain experienced by the film during the "swell and relax" process is greater when the solvent is chloroform as little of it has evaporated during the formation of the water droplets, causing the relaxation of the film to place strain on the film when all of the solvent eventually evaporates. The effect is expected to be less dramatic when the solvent is carbon disulfide as a significant fraction of this solvent has already evaporated during the formation of ordered water droplets. There may be other factors involved in the rupture of the breath figure structured films cast from $CHCl_3$ solutions and more data are needed to identify the cause.

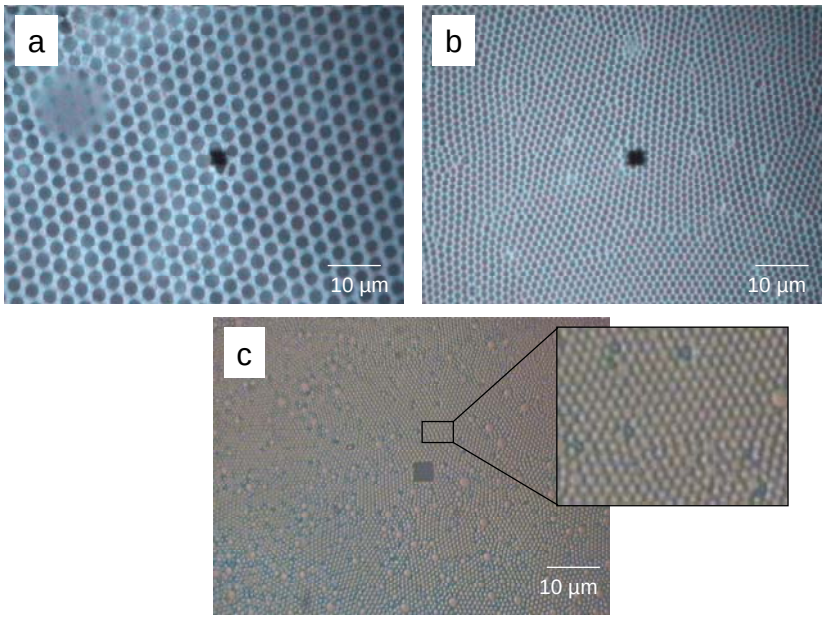

Figure 4.3 Dependence of bubble size on polymer concentration. (*a* and *b* are fluorescence micrographs taken from two different areas of the same sample cast from a 1.0% solution of PFO (M_n 12.9 kg/mol) in CS_2 and *c* is from a sample of 0.06% PFO (M_n 126 kg/mol) in $CHCl_3$ containing 12 wt% MEH-PPV with respect to PFO. The dark square in the center of each image is from the shadow of a fluorescence probe).

An interesting observation was made on the dependence of bubble size on the polymer concentration. For samples prepared from PFO with an average number molecular weight of 12,900 g/mol, the pore sizes change from 3 μm in samples prepared from a 1.0% PFO solution to 2 μm in those cast from a 0.2% solution as shown in **Figure 4.2 (a, b, e)**. Moreover, each sample may display regions of bubble arrays having different pore diameters as indicated in **Figure 4.3**. (Approximately, the bubble diameters are 3 μm, 1 μm, and 0.5 μm in *a, b,* and *c*, respectively). The bubble size can be greatly reduced if the breath figure structured films are prepared from a dilute polymer solution, provided that the average molecular weight of the polymer is relatively high in order to enable the formation of the BFAs at low concentration (**Figure 4.3c**).

The morphology of the BFAs as obtained in **Figure 4.2d** was further studied with SEM. The cross-section view of the sample shows an overall film thickness of about 20-21 μm with the bubble arrays forming a 3 μm-thick monolayer on the surface of the film. Thus looking down from the surface, each bubble is actually a hollow hemisphere of approximately 6 μm in diameter (**Figure 4.4**). These observations were confirmed by AFM although this technique is incapable of measuring thickness of more than 6.4 μm and the overall film thickness was not revealed by AFM. As shown in **Figure 4.5**, the surface of the sample is imprinted with not only well-ordered large bubbles (~6 μm) but also smaller spherical cavities with diameters ranging from about 2 μm to a few hundred nanometers. This type of breath figure structures has also been observed by others.[47]

Blending of PFO with another polymer does not seem to interfere much with the breath figure formation process although a lowering of overall quality is generally observed. However, blends of PFO with a dye such as TPP do have a negative impact on

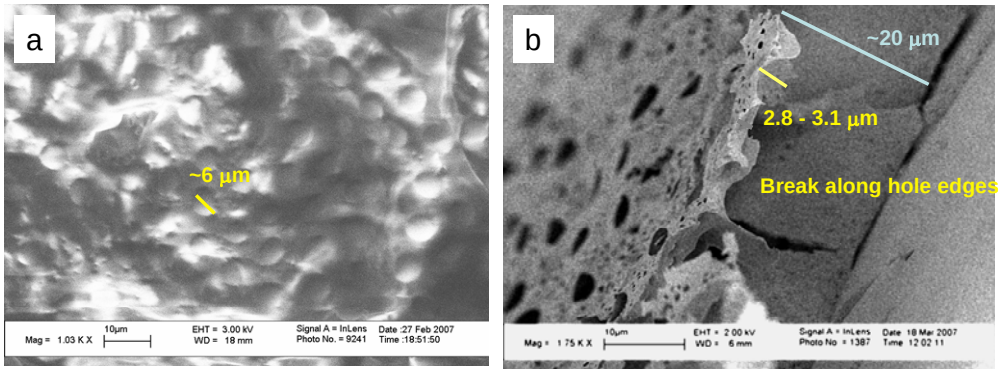

Figure 4.4 SEM images of PFO BFAs (M_n 65.4 kg/mol, 0.2% in CS_2). a) Top view with excessive charging, b) cross-section view.

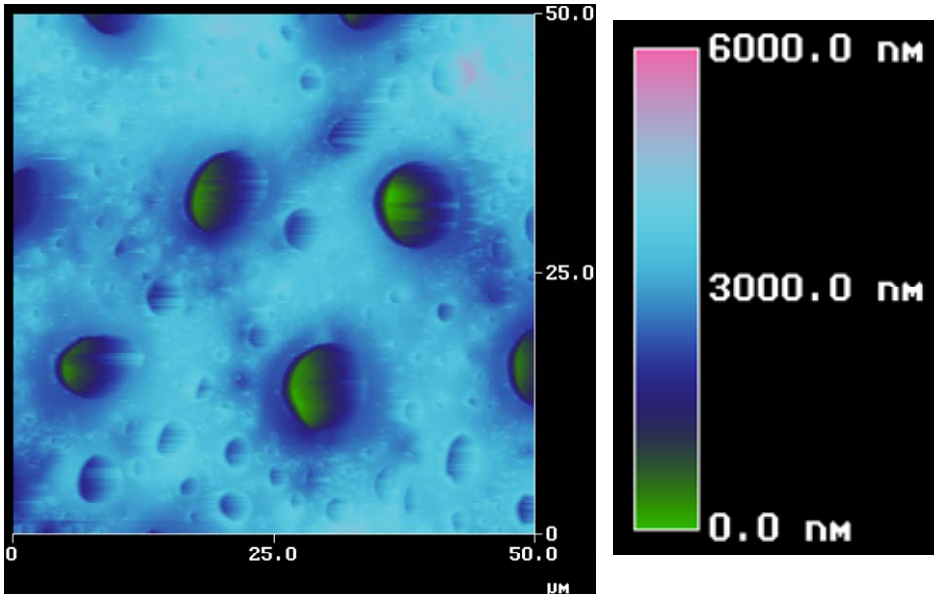

Figure 4.5 AFM image (tapping mode) of PFO BFAs (M_n 65.4 kg/mol, 0.2 wt% in CS_2).

the formation of bubble arrays as shown in **Figure 4.6**. This effect was also observed when we attempted to prepare BFAs of mixtures of PFO with rhodamine B (data not shown). The most likely explanation for this behavior is that the dye molecules, being more soluble in the solvent and having a much greater diffusibility, migrate to the surface

of the solution, which is being concentrated during the formation of the water droplets, and thereby disrupts the temperature gradient between the surface and the water droplets, resulting in localized coalescence of the droplets. This migration to the surface of the dye will be more in evidence when phase separation is discussed in the next sections.

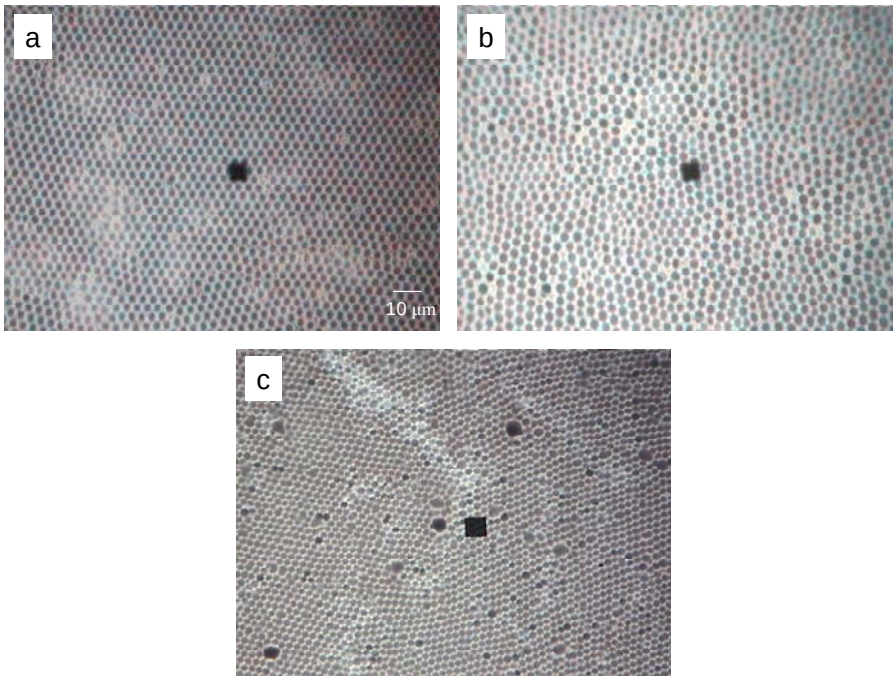

Figure 4.6 Optical micrographs of BFAs of the blends PFO-P3HT (a), PFO:MEH-PPV (b), and PFO-TPP (c) cast from 0.2 wt% PFO-in-CS_2 solutions containing 4.0 wt% of the respective blend components. (Scale bar applies to all images).

4.4 Photophysical properties of the polymers and dye

The absorption and emission spectra of PFO, MEH-PPV, P3HT, and TPP are presented in **Figure 4.7**. The absorption spectrum of PFO in chloroform consists of a sharp peak at 380 nm while that of the PFO film cast from chloroform displays a broad

absorption maximum in the range of 350-410 nm and a minor but well-resolved peak at 433 nm. This latter absorption peak has been considered to be characteristic of the β phase in the literature.[30] In another report, it is also found in the α and α' phase of PFO[23] and was reasoned to be a result of an improved conjugation of PFO chains due to better backbone coplanarity in crystal structures. However, as shown in **Figure 4.8**, this absorption around 433 nm is found in both drop-coated and breath figure structured films of PFO regardless of whether the solvent used in the casting is CS_2 or $CHCl_3$. Moreover, the morphology of PFO in the breath figure arrays is amorphous in nature as will be shown later. Thus it is more likely that this long-wavelength absorption arises from general chain aggregation.

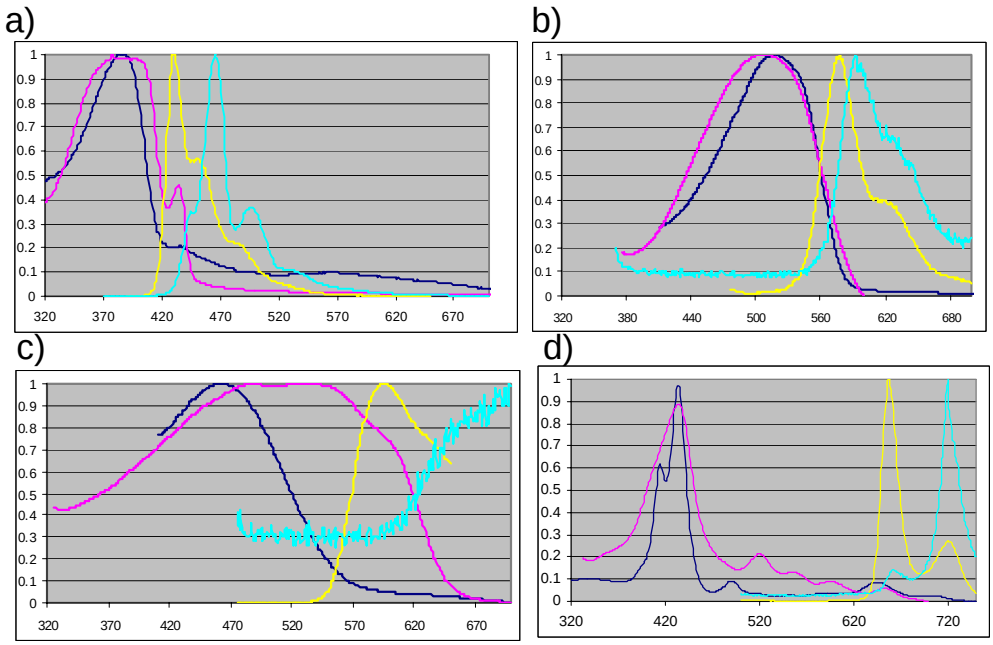

Figure 4.7 Absorption and emission spectra of the energy donor and acceptors. a) PFO, b) P3HT, c) MEH-PPV, and d) TPP [Notes: absorption from chloroform solutions (dark blue), absorption of thin films (pink), fluorescence of chloroform solutions (yellow), and fluorescence of thin films (light blue)].

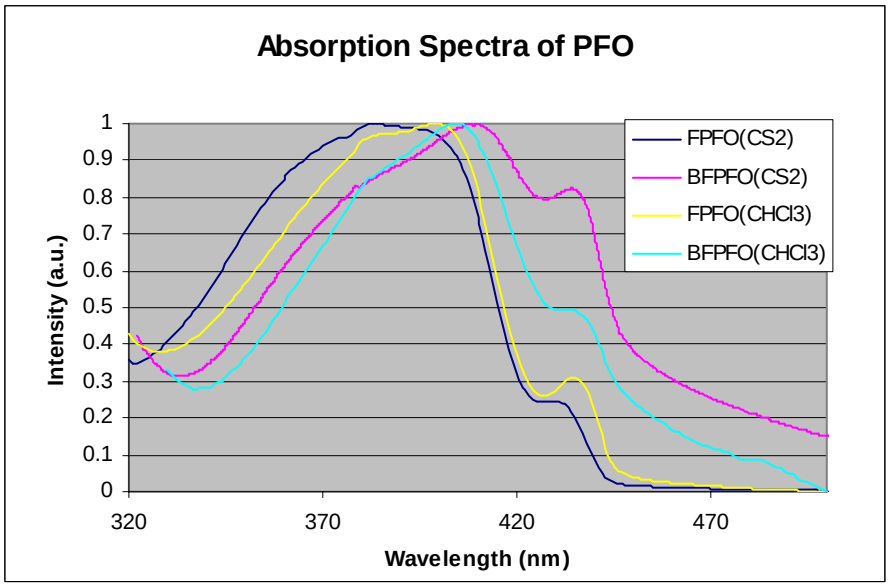

Figure 4.8 Absorption spectra of PFO samples (FPFO: drop-coated film of PFO; BFPFO: breath-figure structured PFO. Indicated in the parentheses are the solvents used for casting).

The fluorescence emission spectrum of PFO in chloroform displays three maxima near 430, 455, and 490 nm which correspond to the vibronic modes (1300-1500 cm^{-1}). The relative intensities of the three maxima have not been explainable using Frank-Condon analysis and the vibronic couplings (455 and 490 nm) to the electronic transition at 430 nm are assumed to involve several phonon modes.[27,48-49] These emission peaks are red-shifted up to 36 nm in chloroform-cast thin films of PFO (**Figure 4.7**). Moreover, the relative intensities of the three maxima are different from breath figure samples to drop-coated films. Whereas the emission spectra of PFO breath figures display three peaks in the range of 440-500 nm and a shoulder centered at 535 nm, the 0-0 peak is often missing in the emission spectra of PFO drop-coated films (**Figure 4.9**). This behavior points to a possibility of different PFO solid-state structures in the two film systems with the result

of a reduced probability of excited-state relaxation to the low-lying vibration levels of the electronic ground state in the drop-coated films. As will be discussed later, the change in the emission profiles of PFO in the two film systems leads to complications in spectral normalization and Stern-Volmer analysis.

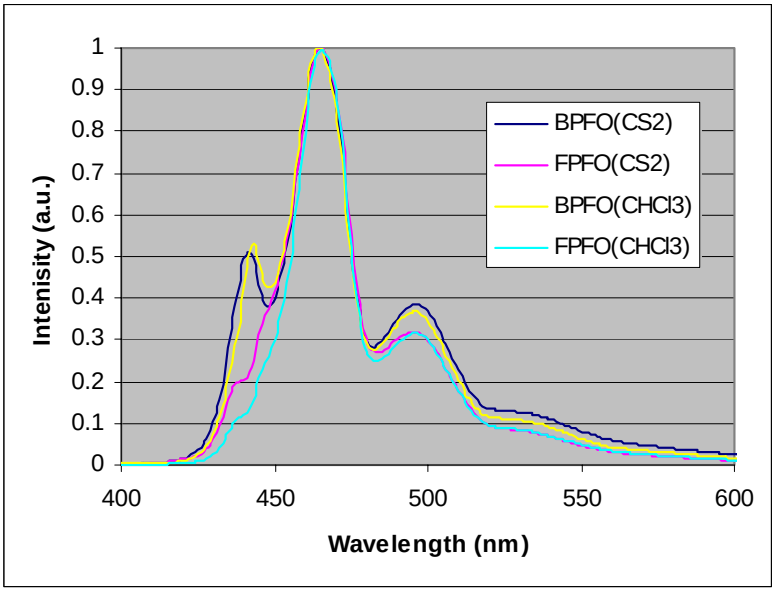

Figure 4.9 Emission Spectra of PFO as BF-structured films and DC-films cast from CS_2 and $CHCl_3$ solutions. (Excitation at 360 nm).

The absorption spectrum of MEH-PPV in chloroform solution shows a maximum at 515 nm. This peak is slightly blue-shifted and broadened when MEH-PPV is prepared as a drop-coated film as shown in **Figure 4.7**. The fluorescence profile of this polymer in chloroform consists of a maximum at 581 nm and a second vibronic transition at 625 nm. These two peaks are red-shifted to 597 and 633 nm, respectively, in the emission spectrum of thin films. Unlike PFO, the relative intensities of the two emission peaks of

MEH-PPV follow similar trend in both solution and solid state and have been found to be consistent with Frank-Condon analysis.[50]

Regioregular P3HT in chloroform solution displays a single absorption peak at 548 nm. However, its thin film absorbs in a broad range from 420 to 610 nm due to π-π stacking. The solution of the polymer in chloroform shows an emission peak at 600 nm and a shoulder at 643 nm. However, thin films of P3HT do not fluoresce at these wavelengths and instead emit very weakly above 700 nm. This behavior of P3HT has been well observed.[39,40]

The red dye TPP in solution and as thin film displays several peaks in its absorption spectrum. In chloroform solution, the spectrum shows peaks at 409, 434, 495 and 642 nm while in thin film it consists of peaks at 431, 519, and 554 nm. The peaks at 409, 434 (in solution), and 431 (in film) are typical of porphyrin Soret band absorption while the peaks at longer wavelengths have traditionally been assigned to the porphyrin Q-band absorption.[21] The fluorescence spectrum of TPP in solution shows two sharp transitions at 658 and 724 nm. In thin films, the first emission peak is slightly red-shifted (667 nm) while the second peak is somewhat blue-shifted (720 nm) and the relative intensities of the two peaks are reversed in the two systems with the first peak being the dominant emission in the solution case and much weaker in thin film. The emission profile of the TPP film is probably complicated by the interactions between the porphyrin systems because the relative intensities of the two emission peaks of TPP in blended systems, where TPP is diluted, more closely resemble those of the TPP in solution.

4.5 Fluorescence energy transfer and phase separation

From the absorption and emission spectra of the polymers and dye, it could be seen that the absorption of each energy acceptor component sufficiently overlaps the emission of the donor PFO and efficient energy transfer is expected according to Förster energy transfer criteria.[51] For clarity, these features are presented in **Figure 4.10**. In all cases, the absorption of the acceptor in the absorption region of the donor (i.e., 340-440 nm with maximum at 380 nm) is very limited, and the emissions of the acceptors in mixtures with the donor are expected to come mainly from energy transfer. However, to ensure that the fluorescence of the acceptors does not come from direct excitation, a study of the blends of polystyrene (PS)-P3HT was performed and the results are shown in

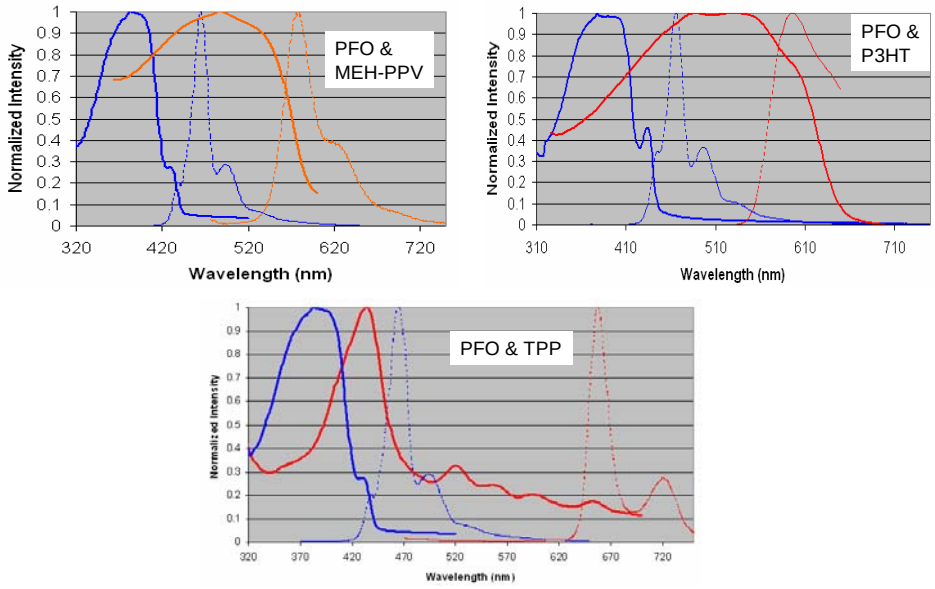

Figure 4.10 Spectral overlap of donor and acceptors. (Solid blue: absorption of PFO film, dotted blue: emission of PFO film, solid red: absorption of acceptor film, dotted red: emission of acceptor in chloroform solution).

Figure 4.11. Clearly, P3HT only fluoresces significantly when it is in solution and excited at its absorption wavelengths, which in this case is chosen to be at the 0-1 emission peak of PFO (i.e., 466 nm). When PS-P3HT solutions or thin films are excited at 360 nm, which is the energy used to excite PFO in the blends, almost no fluorescence of P3HT in the range of 590-600 nm is observed. Thus if fluorescence emission is observed in PFO-P3HT blends, it must come from the energy transfer from PFO to P3HT

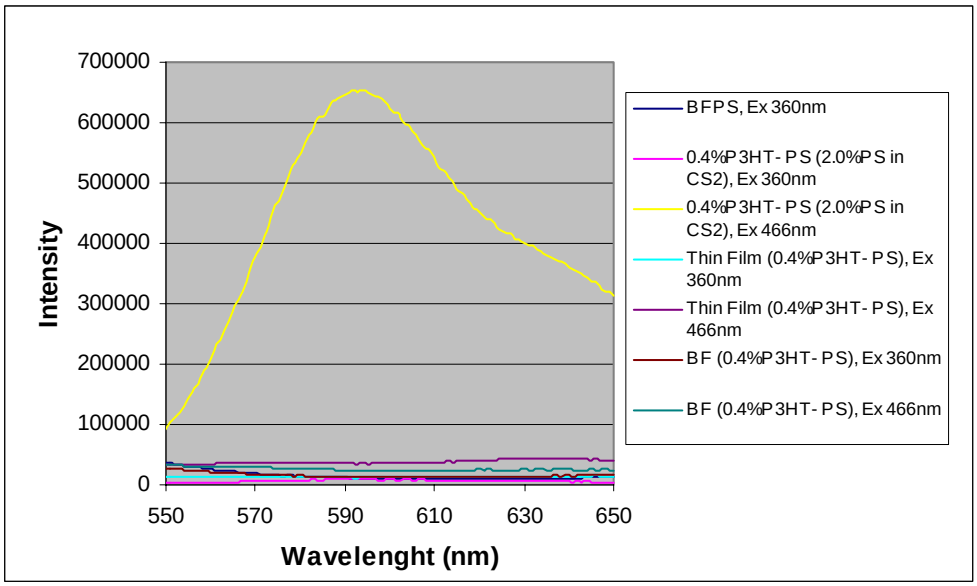

Figure 4.11 Emission spectra of PS-P3HT blends. (Notes: BF stands for breath figures, thin films are prepared by drop coating).

and not from direct excitation of P3HT with light of 360 nm. Moreover, thin films of PS-P3HT blends do not show any significant fluorescence upon excitation with light of 466 nm and, therefore, the fluorescence in the region of 590-600 nm from PFO-P3HT blends, as shown later, is not just a result of dilution of P3HT but must be the result of energy transfer from PFO in the blends. Having shown that the blend systems chosen have

spectral overlaps that facilitate efficient energy transfer, the relationship between energy transfer and phase separation in the blend systems will now be discussed.

4.5.1 PFO-P3HT

In this section, the correlation of fluorescence energy transfer and morphology of the BFAs and DCFs of PFO-P3HT blends are discussed, first the samples cast from CS_2 then those produced from $CHCl_3$ solutions.

4.5.1.1 PFO-P3HT samples cast from CS_2 solutions

The fluorescence spectra of the BFAs and DCFs of PFO-P3HT blends as prepared from CS_2 solutions are presented in **Figure 4.12**. For all three blend systems, the samples were irradiated with 360 nm light to ensure that only PFO was excited and, to be consistent, all fluorescence spectra were normalized at the 0-0 emission peak of PFO. This spectral normalization enables better observation of the quenching of PFO fluorescence in the polymer-polymer blends due to the fact that the absorption maxima of both P3HT and MEH-PPV overlap more with the 0-1 and 0-2 emission peaks of PFO. However, its drawback is twofold. First, the absorption maximum of the dye TPP overlaps better with the 0-0 emission peak of PFO and a spectral normalization at this

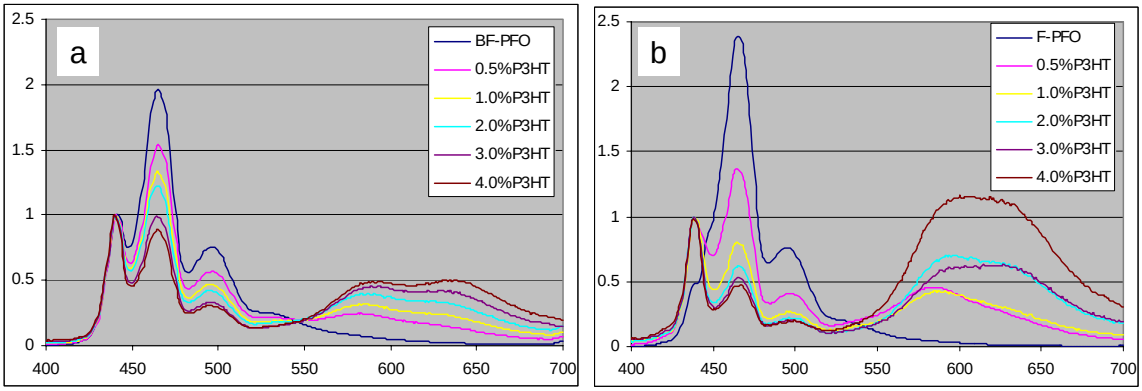

Figure 4.12 Fluorescence spectra of PFO-P3HT samples: BFAs (a) and DCFs (b).

peak coupled with a Stern-Volmer analysis performed at the 0-1 PFO emission peak tends to underestimate the quenching effects of TPP as will be shown later. Second, the fluorescence spectra of the DCFs sometimes do not display the PFO's 0-0 emission peak as mentioned before (**Figure 4.9**). Not withstanding these difficulties, the spectra were normalized at the maximum in the wavelength range of 400-450 nm because Stern-Volmer analysis is best carried out at the well-behaved 0-1 emission peak.

As evidenced from **Figure 4.12**, the reduction in the PFO fluorescence is accompanied by an enhancement of the emission of P3HT as the concentration of the latter is increased, indicating efficient energy transfer (ET) from the donor to the acceptor. Moreover, it is clear that the ET efficiency is higher in the DCFs than the BFAs (**Figure 4.13)** and that, in both cases, the emission peak of the acceptor is progressively red-shifted as its concentration in the blends is increased, suggesting a higher probability of acceptor-acceptor intermolecular interactions. To learn more about the emission near 640 nm, which resembles the fluorescence of an unblended P3HT film, the samples were

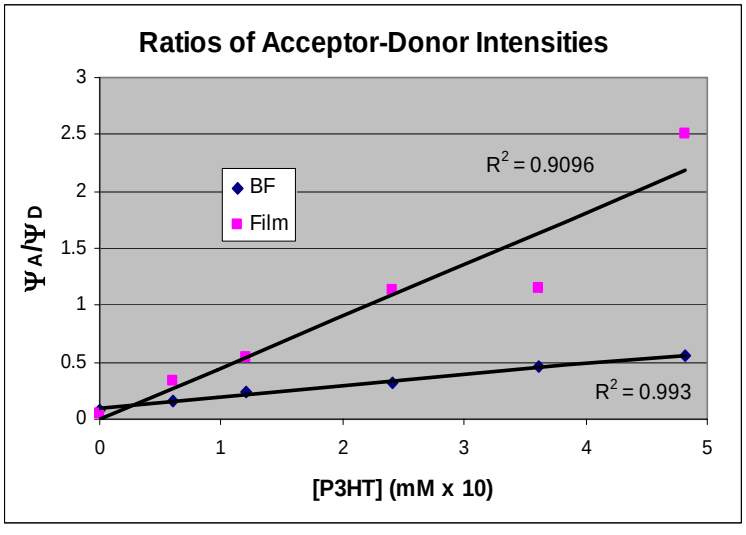

Figure 4.13 Ratios of acceptor-donor emission intensities.

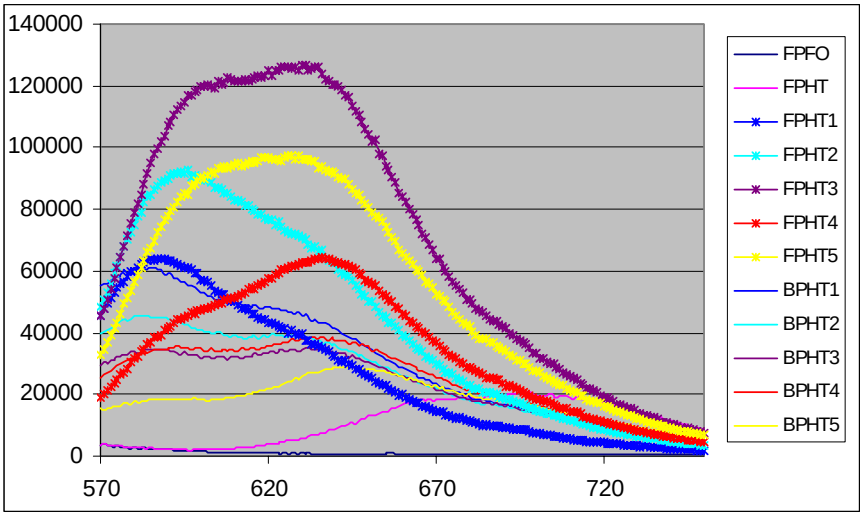

Figure 4.14 Fluorescence of PFO-P3HT samples excited at 540 nm.

excited with 540 nm light where P3HT absorbs strongly but PFO absorption is non-existent. It was found that the emission profiles (**Figure 4.14**) matched closely with those in **Figure 4.12**. Since little fluorescence is observed from unblended P3HT films regardless of the excitation energy, the behavior observed here suggests that somehow

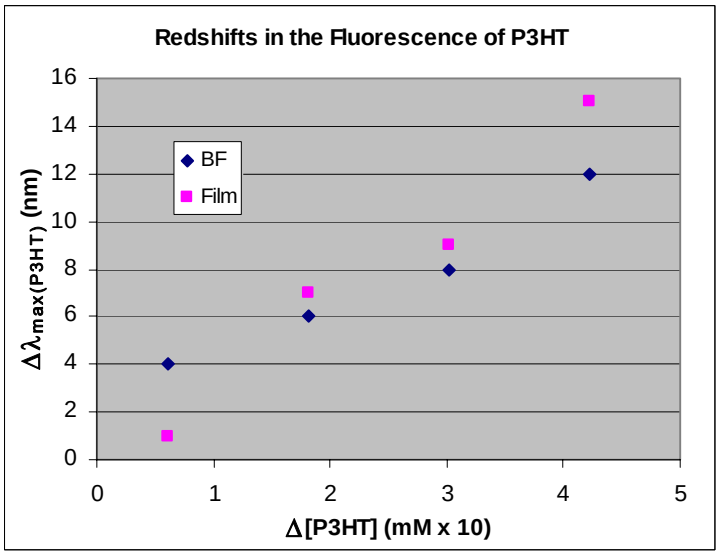

Figure 4.15 Relative positions of P3HT maximum emission peaks versus changes in concentration. (Calculations are relative to the 0.5% P3HT samples).

P3HT aggregates are effectively excited by energy transfer from PFO and their fluorescence is significantly enhanced. The nature of energy transfer from PFO to the P3HT aggregates is still unclear and difficult to understand particularly in the case of DCFs where the formation of PFO crystals (to be shown later) was observed and the extent of P3HT aggregation is greater (**Figure 4.15**).

The steady-state fluorescence data pose a question of why drop-coated films exhibit higher ET efficiency than the BF-structured films even though P3HT aggregation is more pronounced (i.e., more phase separated) in the former than the latter. A comparison of the Stern-Volmer plots and the excited-state decay profiles points to a possible answer. The excited-state lifetimes of PFO become shorter as P3HT concentration is increased, confirming the presence of energy transfer (**Figure 4.16**). Moreover, the rate of quenching of PFO fluorescence is slower in the DCFs as indicated by the extracted lifetimes (**Table 4.1**). Interestingly, the excited-state lifetimes of PFO drop-coated films are longer than those of BF-structured PFO films. Consequently, the

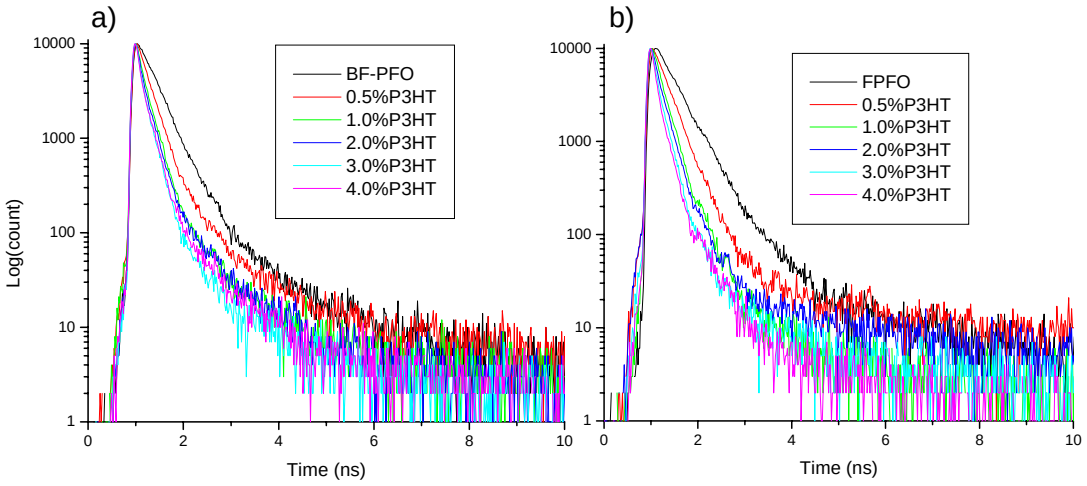

Figure 4.16 Excited-state decay profiles of PFO-P3HT BFAs (a) and DCFs (b). (λ_{pump} 372 nm, λ_{probe} 466 nm).

Table 4.1 Excited-state lifetimes of PFO-P3HT samples.

P3HT (wt%)	τ (ps) BFAs	τ (ps) DCFs
0	306.6	405.2
0.5	172.2	205.3
1.0	114.6	152.3
2.0	94.9	121.8
3.0	77.4	94.1
4.0	49.6	80.6

τ_o/τ plots, where τ_o represents the lifetime of the excited state of PFO in the unblended sample and τ is the fluorescence lifetime of PFO in the blended samples, for BFAs and DCFs of PFO-P3HT blends are highly comparable (**Figure 4.17**). The Stern-Volmer plots, on the other hand, clearly show that the fluorescence of PFO is more effectively quenched by P3HT in the drop-coated films. The discrepancy in the two types of analysis points to at least two possibilities: either the steady-state fluorescence data do not allow for a more accurate representation of the quenching behavior by Stern-Volmer analysis or the τ_o/τ plots misrepresent the underlying process by not having sufficient data points. The reliability of the excited-state lifetime data was investigated by making measurements at different segments of each sample. The averaged lifetimes of PFO in the

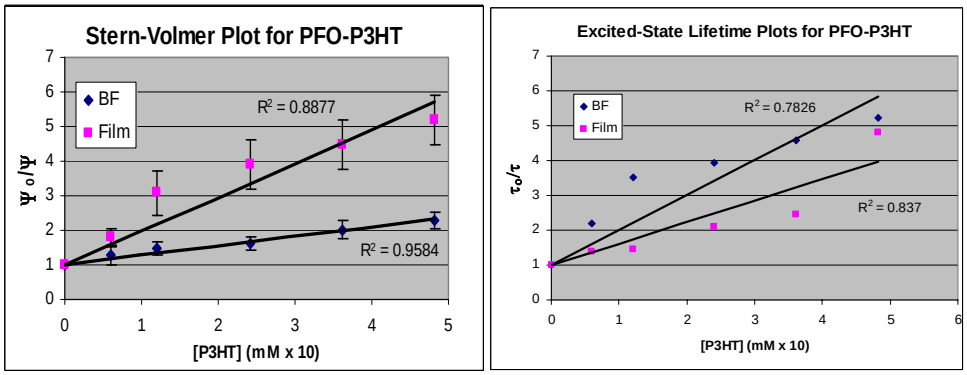

Figure 4.17 Stern-Volmer plots and τ_o/τ plots for PFO-P3HT samples.

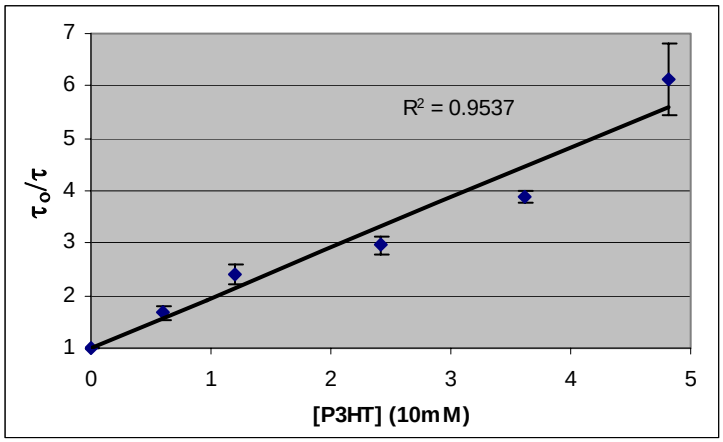

Figure 4.18 Ratios of excited-state lifetimes of PFO-P3HT BFAs.

PFO-P3HT BFAs from two sets of samples were used in the τ_o/τ plot shown in **Figure 4.18**, which closely resembles the corresponding plot in **Figure 4.17**. The reliability of the Stern-Volmer analysis, on the other hand, is more questionable due to the far-from-constant relative intensities of the three PFO vibration-coupled emission maxima as discussed before (**Figure 4.9**). All in all, the fluorescence energy transfer data show a slightly higher ET efficiency in PFO-P3HT DCFs than in BFAs, suggesting a more uniform distribution of the blend components in the former, and imply phase separation by P3HT aggregation in both systems. Moreover, since significant PFO fluorescence is still observed at high P3HT concentration, the morphology in both cases is expected to be highly inhomogeneous and contains PFO-rich domains inaccessible to P3HT molecules. The findings will now be compared to the morphological study using fluorescence microscopy.

The conditions involved in the preparation of the polymeric bubble arrays resulted in some intriguing observations of the phase separation behavior. Although the phase-separated morphology is not obvious when studied with AFM, it is clearly seen in

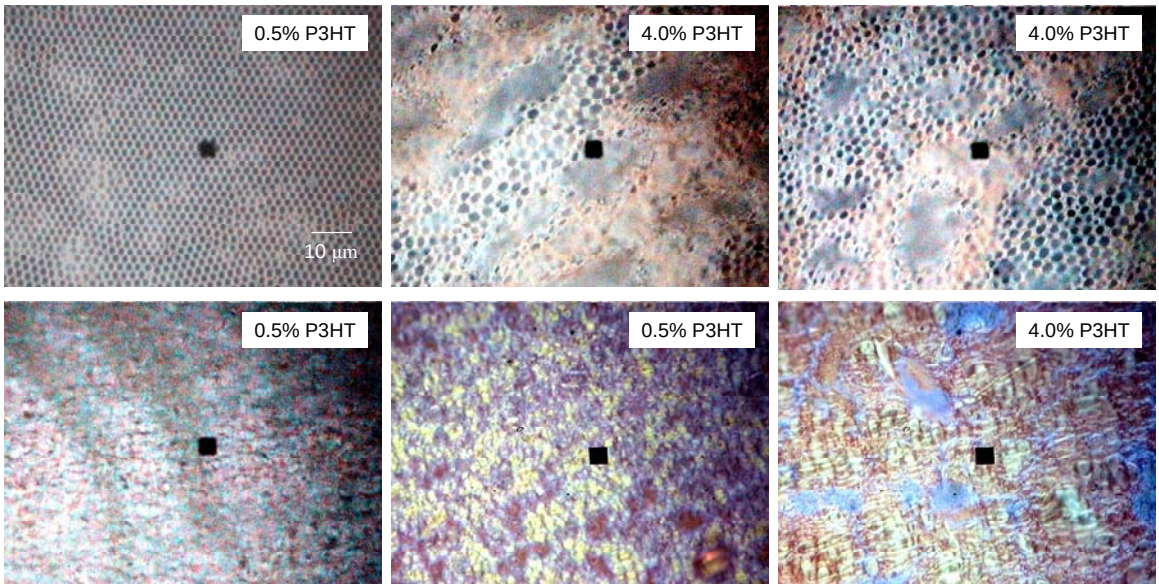

Figure 4.19 Phase separation in PFO-P3HT samples observed under a fluorescence microscope: BFAs (first row) and DCFs (second row). (Samples were excited at 365 nm).

the fluorescence micrographs as shown in **Figures 4.19** thanks to the light-emitting nature of the polymers. In the breath figures, phase separation is hard to discern in areas where well-ordered bubbles are formed. However, in regions of disordered bubbles, the surface features scattered P3HT-rich domains as revealed by the red-colored zones where air bubbles are absent. To confirm that the red areas are rich in P3HT and the blue regions consist mainly of PFO, the fluorescence spectra obtained from these spots, indicated by the dark squares in the images, were obtained and presented in **Figures 4.20** for a sample prepared from a 0.23 wt% solution of PFO with an average M_n of 65.4 kg/mol in CS_2 containing 0.86% P3HT with respect to PFO. Clearly, the emission near 590 nm is higher in areas more saturated with the red color while the fluorescence of PFO is dominant in the blue regions. It can be inferred from the fluorescence micrographs of the BFAs that the phase separation behavior is dictated mainly by a redistribution of the

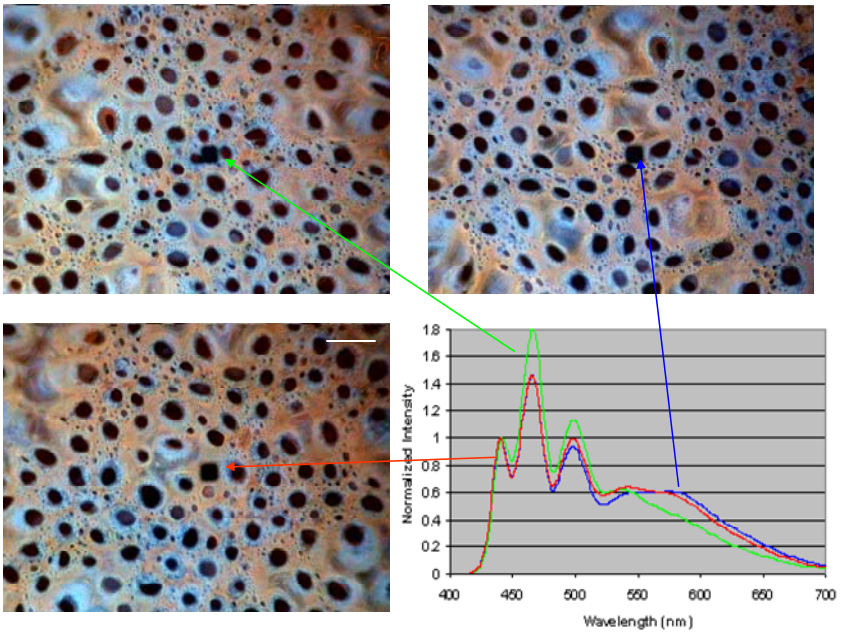

Figure 4.20 Fluorescence micrographs and spectra taken at different areas of a BF-structured sample of PFO-P3HT blend. (0.86% P3HT, λ_{ex} = 365 nm, scale bar = 12 μm).

blend composition that is resulted from the material transport dynamics during the bubble-forming process. The hydrodynamic flow is unquestionably accelerated by the flow of moist air and the resultant non-uniform evaporative cooling effect. Consequently, the partition of the blend solution during the BF-forming process into domains of varying polymer concentrations gives rise to segments of film where (i) breath figures are not formed, or (ii) well ordered bubbles develop, or (iii) ordered bubbles of smaller size are created, and (iv) PFO or P3HT is more concentrated. Furthermore, the images in **Figure 4.20** is seen to suggest that P3HT prefers to diffuse to the surface (i.e., away from the substrate) because its absence on the rims of the bubbles implies that PFO forms a thick wetting layer which is covered with a P3HT layer. Nevertheless, a depth profile analysis is needed to determine whether such a phase separation behavior does occur. The low ET

efficiency of PFO-P3HT BFAs as observed in **Figure 4.12a** is thus a result of phase separation into PFO-rich and P3HT-rich domains brought about by the material transport dynamics during the BF-forming process. The aggregation of P3HT as seen in the red-colored bubble-absent domains also explains the observation of the red-shift in the emission peaks of the P3HT in the blend samples. However, no signs of crystallization of the blend components are observed. This is far from being true for the drop-coated film samples.

The reasons the study was concerned with drop-coated films (DCFs) instead of spin-coated films are twofold. First, this study was designed to investigate the effects of solvent evaporation rates on the phase separation behavior and the process of drop coating allows the solvents to evaporate slowly. This is in contrast to the fast evaporation rates in the breath figure formation process and enables better comparison of the data obtained from the two methods. Second, the drop-coating procedure was done in an environment deficient of moist air circulation, which provides another contrasting criterion to the bubble-forming process that involves the flow of moist air on the surfaces of the polymer solutions.

The fluorescence micrographs of typical PFO-P3HT DCFs as shown in **Figure 4.19** reveal contrasting phase separation patterns to those of the breath figure analogues. In samples of low P3HT concentration, phase separation of the components as indicated by the spots of red and blue colors occurs at a rather small scale and, as a result, the distribution of the blend composition is relatively uniform throughout large areas of the films. When P3HT concentration is increased, phase separation is progressively more extensive and sizable PFO-rich and P3HT-rich domains are well defined. Moreover, the

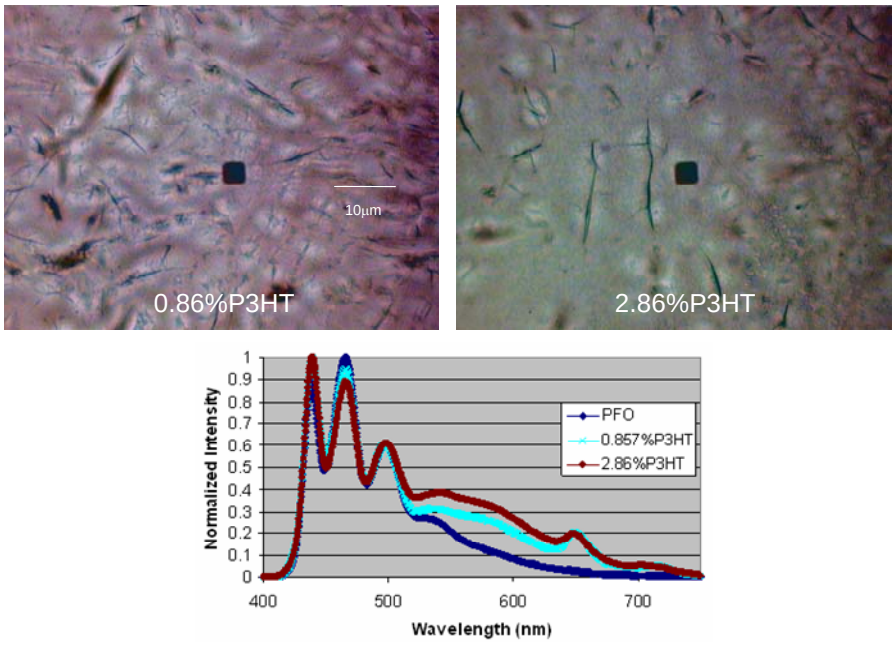

Figure 4.21 Fluorescence micrographs and spectra of PFO-P3HT DCFs. (Samples were cast from 0.23 wt% PFO-P3HT solutions in CS_2. M_n of PFO is 65.4 kg/mol).

films display dark-red features that have a crystalline texture, suggesting a more crystal-like aggregation of P3HT component that accounts for the considerable red-shift in the fluorescence of the films (**Figures 4.12 & 4.15**). Although actual crystals of P3HT are not observed in these films since a well defined emission peak at 650 nm is absent, the tendency of P3HT to form crystals in DCFs is implicated in samples cast from more concentrated blend solutions as shown in **Figure 4.21**. Due probably to the low content of P3HT crystals, their presence is not confirmed by XRD which, however, reveals the existence of PFO crystals in DCFs cast from either CS_2 or $CHCl_3$ blend solutions but not in BFAs (**Figure 4.22**). The diffraction patterns resemble those reported for the α-phase of PFO crystals.[23] Although XRD was not performed on the samples presented in **Figure 4.19**, the yellow clusters observed in the DCFs most likely represent PFO crystals or

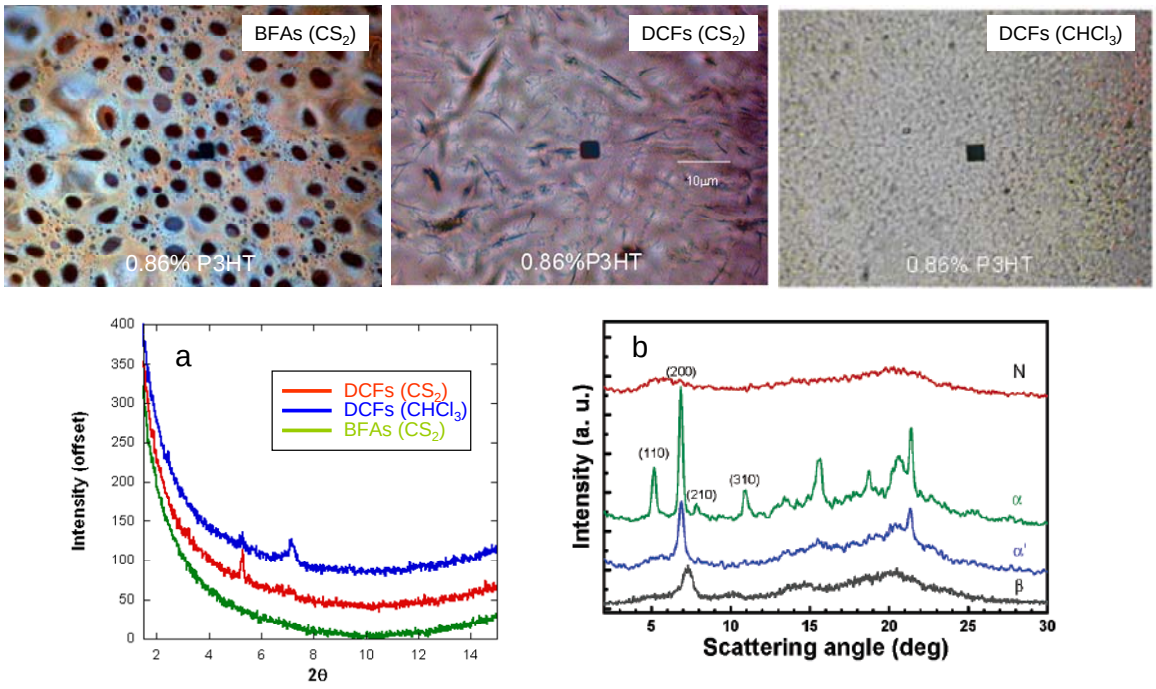

Figure 4.22 Fluorescence micrographs and the corresponding X-ray diffraction patterns of PFO-P3HT BFAs and DCFs cast from 0.23 wt% blend solutions in CS_2 and $CHCl_3$. (PFO of M_n 56.4 kg/mol was used. Figure in *b* shows XRD profiles of PFO in different phases and is copied from reference 23).

semi-crystals. Thus, the slower rate of solvent evaporation involved in the preparation of DCFs enables the blend components to phase separate by crystallization. This process is, however, limited by the rapid evaporation of such a volatile solvent as CS_2 and consequently the extent of phase separation is restricted, resulting in a slightly higher ET efficiency than in the BFAs.

The phase separation dynamics in both BFAs and DCFs systems resembles neither spinodal decomposition nor nucleation and growth mechanisms as presented in Chapter 3. This is most likely due to the non-equilibrium processes occurring in these two systems as driven by rapid solvent evaporation. If the rate of solvent evaporation

plays such a major role in the morphology of BF-structured and drop-coated films, one would expect phase separation to be more extensive when the samples are prepared from chloroform solutions, which evaporate slower than carbon disulfide. For comparison, the data obtained for PFO-P3HT BFAs and DCFs cast from $CHCl_3$ solutions will now be presented and discussed.

4.5.1.2 PFO-P3HT samples cast from $CHCl_3$ solutions

Steady-state fluorescence measurements of the PFO-P3HT samples prepared from chloroform solutions show little fluorescence from the energy acceptor component in the DCFs as compared to the BFAs even though significant quenching of the energy donor fluorescence is observed in both cases (**Figure 4.23**). The higher ET efficiency in the BFAs as compared to the DCFs is more clearly seen from the plots of acceptor-donor emission intensity ratios as shown in **Figure 4.24** where the slope of the linear fit to the data points of the BF-structured samples is much higher than that of the drop-coated samples. This is in contrast to the trends observed in samples cast from CS_2 solutions as

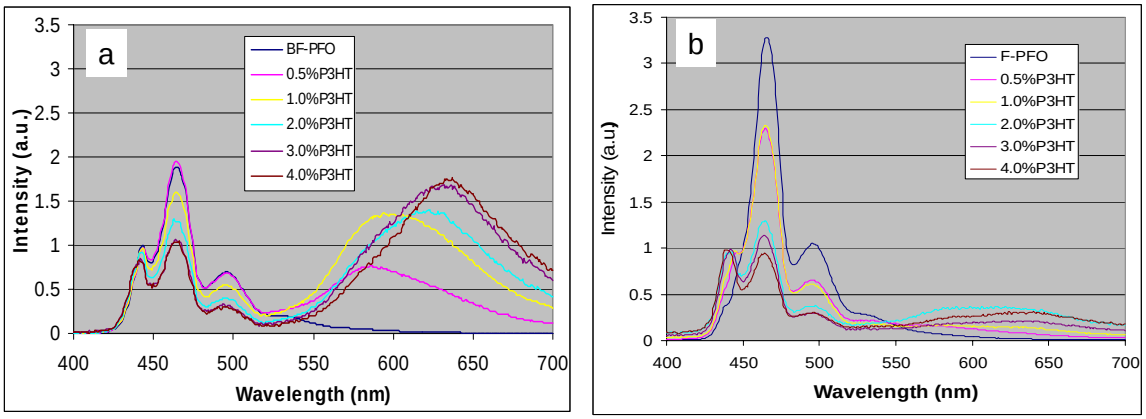

Figure 4.23 Fluorescence spectra of PFO-P3HT samples cast from $CHCl_3$ solutions: BFAs (a) and DCFs (b).

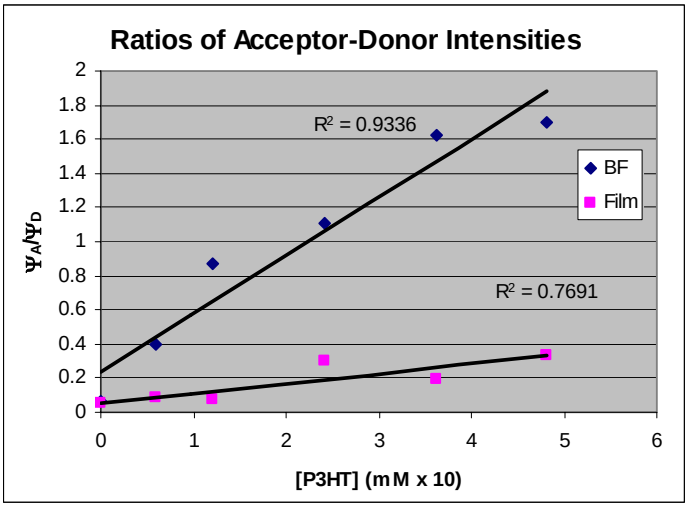

Figure 4.24 Ratios of acceptor-donor emission intensities.

discussed above. However, similar to the fluorescence profiles of the samples cast from CS_2 solutions, the emissions of the P3HT in the blend samples prepared from $CHCl_3$ are red-shifted as the P3HT concentration is increased. Again, such behavior points to a possibility of P3HT forming aggregates. Moreover, the extent of P3HT aggregation is

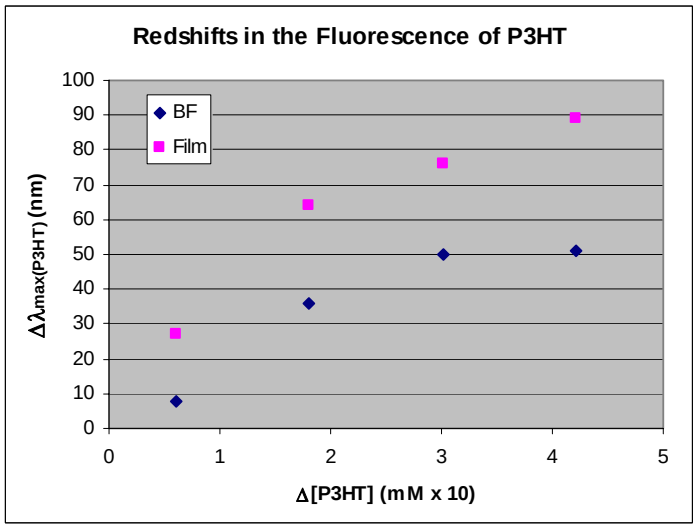

Figure 4.25 Relative positions of P3HT maximum emission peaks versus changes in concentration. (Calculations are relative to the 0.5% P3HT samples).

expected to be higher in the DCFs than in the BFAs as the emission peaks of P3HT are more red-shifted in the former than the latter (**Figure 4.25**).

The energy transfer efficiency relationship between the BFAs and DCFs as observed in the steady-state fluorescence measurements is consistent with the excited-state decay profiles as shown in **Figure 4.26**. Here, the rate of reduction in the excited-state lifetime of the energy donor as a function of acceptor concentration is slower for DCFs than BFAs. This is more obvious from the τ_o/τ plots (**Figure 4.27**) where the slope of the linear fit to the data of the BFAs is greater than that of DCFs. However, the trend is reverse in the Stern-Volmer plots which show the quenching of PFO fluorescence by P3HT to be more effective in the DCFs than BFAs. Again, the reliability of the Stern-Volmer analysis is hampered by the inconsistency in the relative intensities of the three vibration-coupled emission peaks of PFO, especially as the ratio of the 0-1 to 0-0 intensities is so much larger in the DCFs than in the BFAs (**Figure 4.23**).

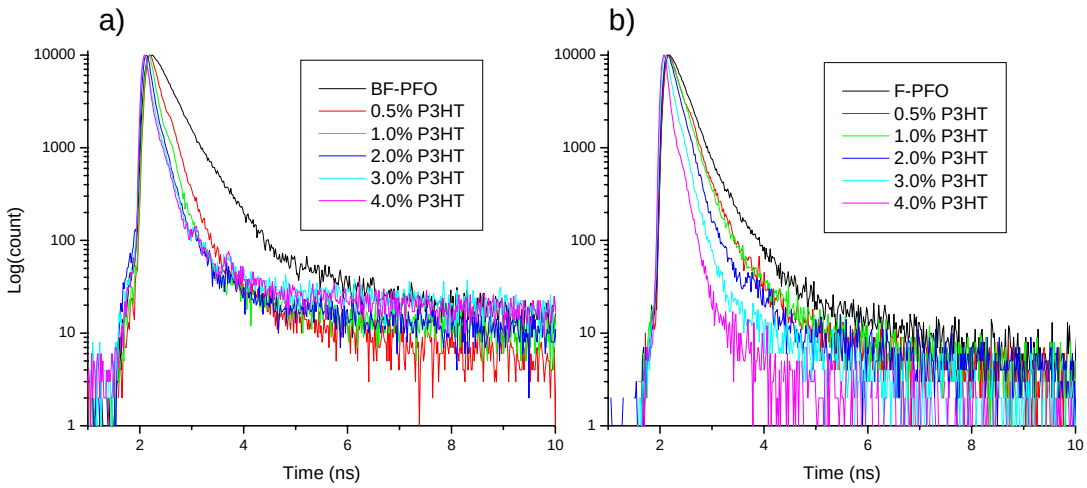

Figure 4.26 Excited-state decay profiles of PFO-P3HT BFAs (a) and DCFs (b) prepared from $CHCl_3$ solutions. (λ_{pump} 372 nm, λ_{probe} 466 nm).

Table 4.2 Excited-state lifetimes of PFO-P3HT samples cast from $CHCl_3$.

P3HT (wt%)	τ (ps) BFAs	τ (ps) DCFs
0	351.7	248.7
0.5	161.5	177.4
1.0	99.7	170.8
2.0	89.5	118.6
3.0	76.7	101.5
4.0	67.1	51.6

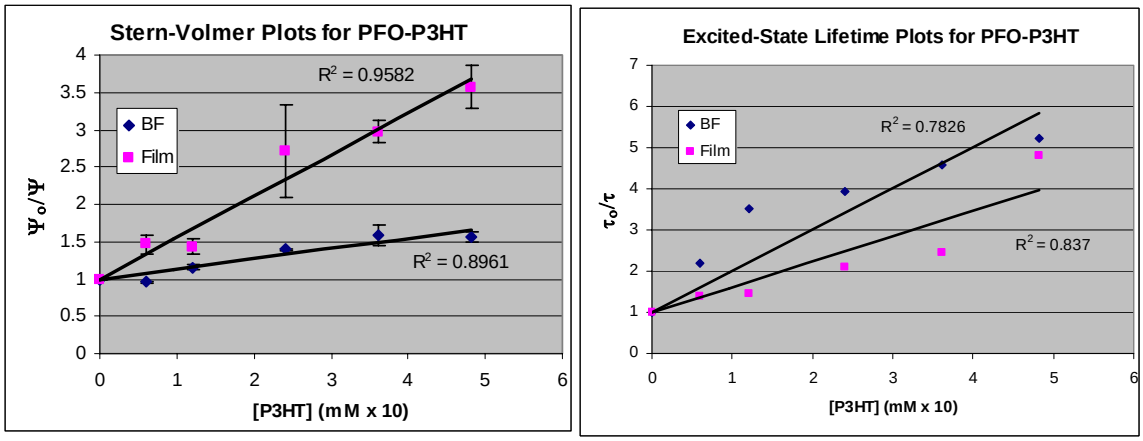

Figure 4.27 Stern-Volmer plots and τ_o/τ plots for PFO-P3HT samples cast from $CHCl_3$.

The spectroscopic data thus reveal a much higher ET efficiency in the BFAs than in the DCFs of PFO-P3HT blends prepared from $CHCl_3$ solutions. Additionally, the emission from the energy acceptor is significantly red-shifted in both systems as the acceptor concentration is increased. It is also noteworthy that the average excited-state lifetime of the unblended PFO films drop-cast from $CHCl_3$ is much shorter (c.a. 248.7 ps) than that of the BF-structured PFO films (c.a. 351.7 ps for $CHCl_3$ and 306.6 ps for CS_2) as well as of PFO films drop-cast from CS_2 (c.a. 405.2 ps). These findings suggest an underlying morphology where phase separation is more extensive in the DCFs cast from $CHCl_3$ solutions than in the BFAs.

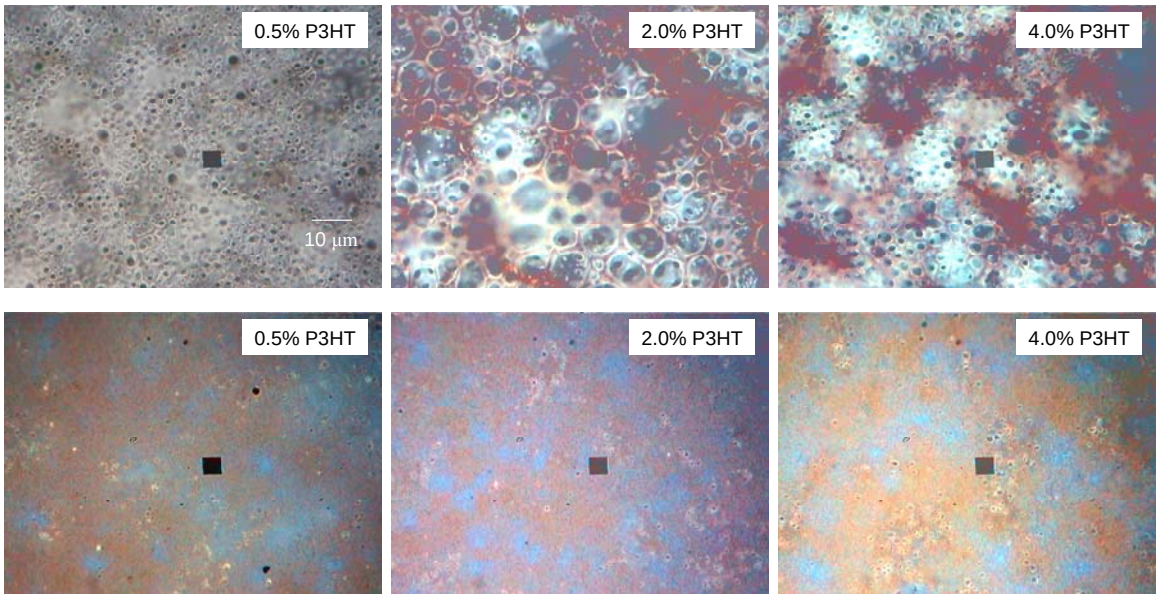

Figure 4.28 Fluorescence microscopy images of PFO-P3HT samples cast from $CHCl_3$.

The morphology of the BFAs and DCFs of PFO-P3HT blends as observed under a fluorescence microscopy is given in **Figure 4.28**. Phase separation is observed in both systems. Whereas phase behavior in the BFAs seems to be determined by the redistribution of the blend composition as similarly observed in the counterparts prepared from CS_2 solutions, film morphology in the DCFs may be characterized as resulted from the aggregation of each blend component. Evidently, changing the solvent from CS_2 to $CHCl_3$ does not change the factors that govern the phase separation mechanisms. What has been changed is that the slower solvent evaporation rate of $CHCl_3$ enables the blend components in the drop-coated films to de-mix to a greater extent and, as a result, donor-acceptor interactions are reduced. Previous studies of PFO-P3HT films spin-cast from $CHCl_3$ solutions claimed a phase separation mechanism of nucleation and growth.[41] Although a hint of that is observed in these drop-coated films, the morphology can only be classified as a segregation of the blend components.

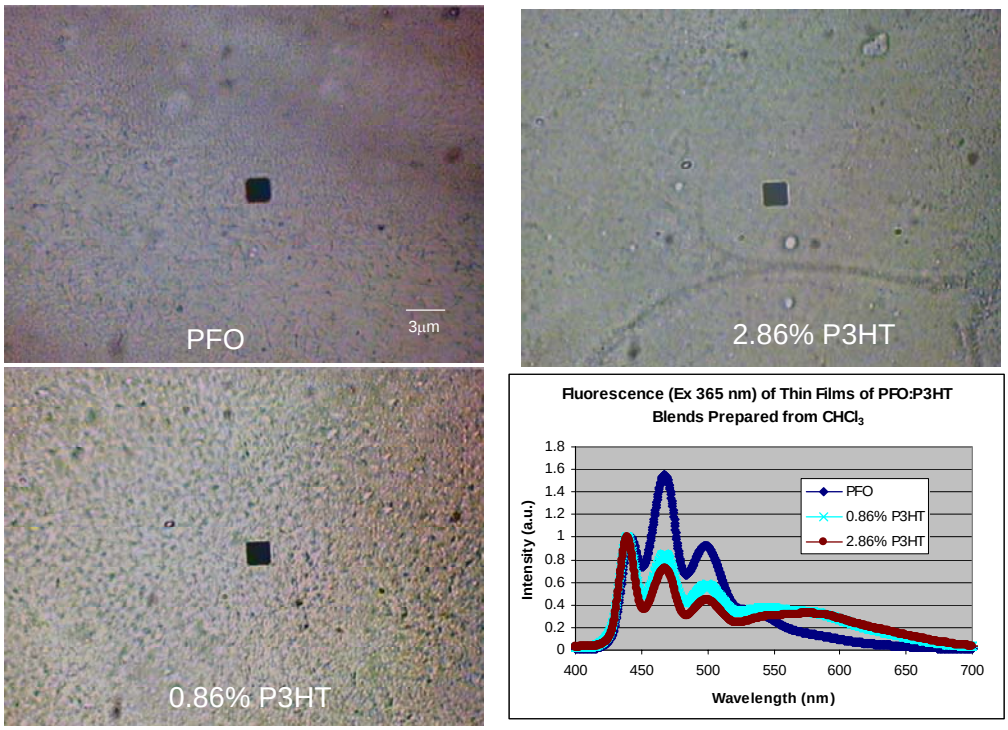

Figure 4.29 Fluorescence micrographs and spectra of PFO-P3HT DFCs cast from $CHCl_3$ solutions. (PFO with M_n of 65.4 kg/mol, polymer concentrations were 0.23 wt%).

The surface texture and the low ET efficiency of the films drop-cast from $CHCl_3$ suggest some extent of PFO crystallization. In fact, similar blend samples prepared from PFO with an average M_n of 65.4 kg/mol show extensive crystallization of PFO (**Figure 4.29**) as confirmed by XRD (**Figure 4.22**). A lack of a well-resolved emission peak at 650 nm in the fluorescence spectra (**Figure 4.23b**) rules out the possibility of P3HT crystallization although higher concentration of P3HT results in greater aggregation and the emission peak is red-shifted further toward 650 nm. While other factors such as solvent polarity and polymer solubility may play a role in the phase-separate morphology of the BFAs and DCFs, it is shown here that, the parameters involved in the preparation of breath figures (e.g., moisture and airflow velocity) and the rate of solvent evaporation

have a determining impact on the morphology and the resulting energy transfer efficiency of films of polymer blends. To learn whether the phase behavior and the spectroscopic properties of the PFO-P3HT samples apply only to this blend system, the results obtained for another polymer-polymer blend system, namely PFO:MEH-PPV, will now be presented and discussed.

4.5.2 PFO:MEH-PPV

Due to its higher quantum yield, the fluorescence of MEH-PPV as a result of energy transfer from PFO is expectedly observed to be much greater than that of the PFO-P3HT samples. Moreover, since the solubility in CS_2 and $CHCl_3$ as well as the "mixability" with PFO of MEH-PPV and P3HT are not the same, the phase separation behavior is found to be slightly different between the two blend systems.

4.5.2.1 PFO:MEH-PPV samples cast from CS_2 solutions

Steady-state fluorescence measurements reveal energy transfer to be somewhat more effective in the BFAs than DCFs of the PFO:MEH-PPV blends prepared from CS_2 solutions as shown in **Figure 4.30**. Yet, the quenching of PFO fluorescence by MEH-

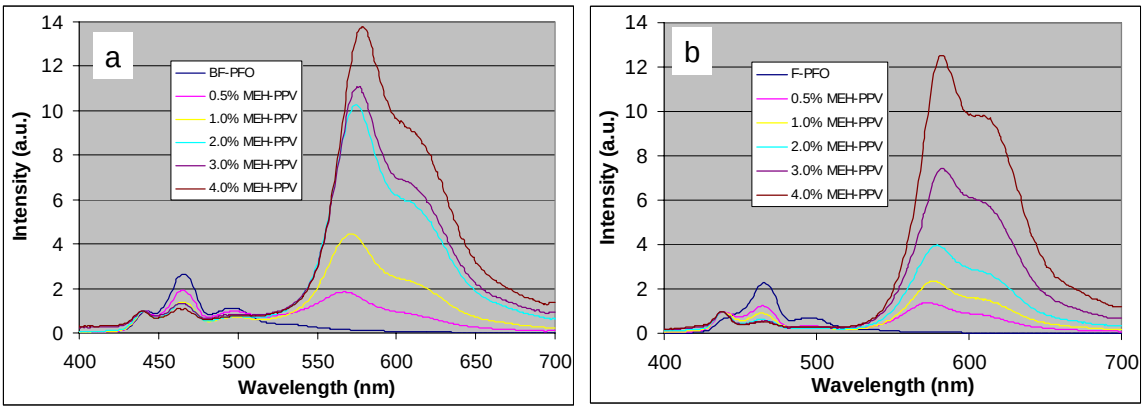

Figure 4.30 Fluorescence spectra of BFAs (a) and DCFs (b) of PFO:MEH-PPV samples prepared from CS_2 solutions.

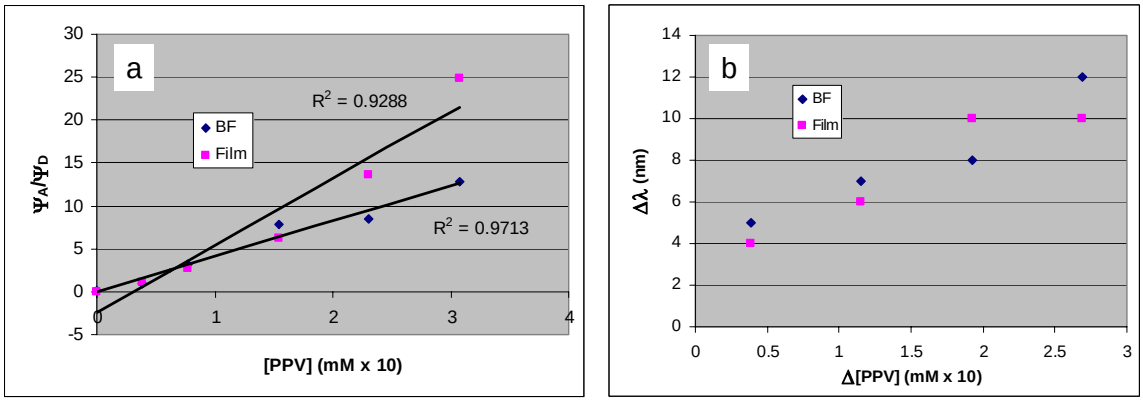

Figure 4.31 Acceptor-donor emission intensity ratios (a) and relative changes in the wavelengths at MEH-PPV emission maxima (b) of PFO:MEH-PPV samples.

PPV as indicated by the reduction in the intensity of the emission peak at 466 nm appears to be more efficient in the DCFs than BFAs. As a result, the slopes of the linear fits to the acceptor-donor emission intensity ratio plots (**Figure 4.31a**) and the Stern Volmer plots (**Figure 4.33a**) are greater for DCFs than BFAs. Why is the reduced fluorescence of the energy acceptor associated with an enhanced quenching of the donor fluorescence? This question can not simply be explained by the changes in the relative intensities of the three vibronic couplings of PFO because the effective quenching of the donor emission by the acceptor in the DCFs is further confirmed by the excited-state lifetime measurements (**Table 4.3 & Figures 4.32b & 4.33b**). Such behavior seems to suggest additional modes of quenching, such as PFO self-quench by interchain exciton migration.[19] This process, however, implies some extent of PFO crystallization in the DCFs. In fact, although the red-shifts in the emission peaks of MEH-PPV are similar in BFAs and DCFs (**Figure 4.31b**) and therefore MEH-PPV is expected to form aggregates but not crystals, the crystallization of PFO is observed in the DCFs of the blends. This will be shown after the

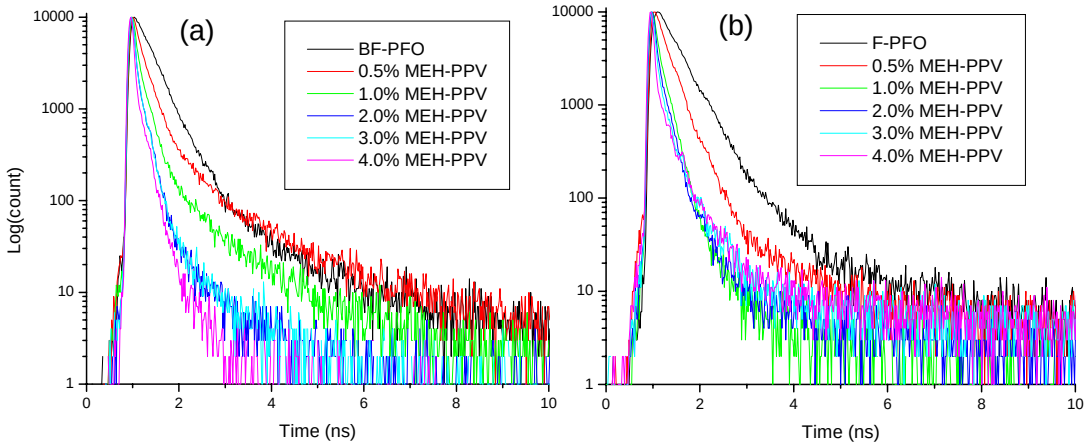

Figure 4.32 Excited-state decay profiles of BFAs (a) and DCFs (b) of PFO:MEH-PPV samples cast from CS_2. (λ_{pump} 372 nm, λ_{probe} 466 nm).

Table 4.3 Excited-state lifetimes of PFO:MEH-PPV samples cast from CS_2.

MEH-PPV (wt%)	τ (ps) BFAs	τ (ps) DCFs
0	306.6	405.2
0.5	121.3	146.2
1.0	74.3	56.1
2.0	62.5	52.9
3.0	44.2	42.9
4.0	20.5	16.6

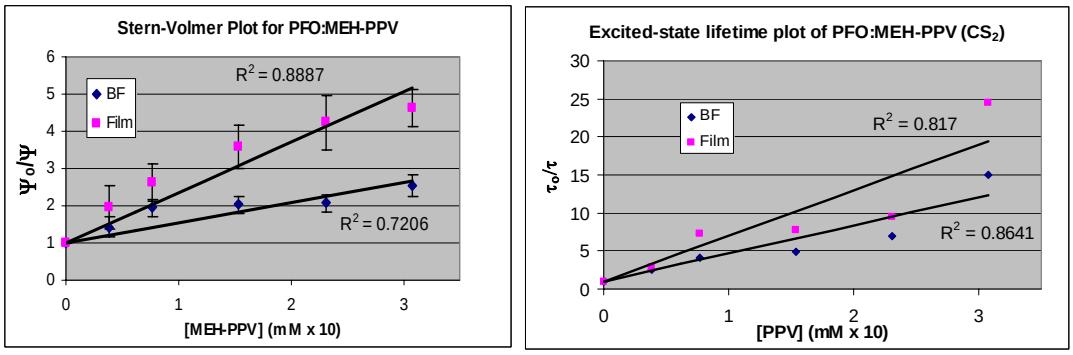

Figure 4.33 Stern-Volmer and τ_o/τ plots for PFO:MEH-PPV samples.

morphology of the BFAs is discussed.

Similar to the phase behavior observed in the BFAs of PFO-P3HT blends, the morphology of the breath figures of the PFO:MEH-PPV blends seems to be determined by the material transport dynamics during the breath figure formation process. The

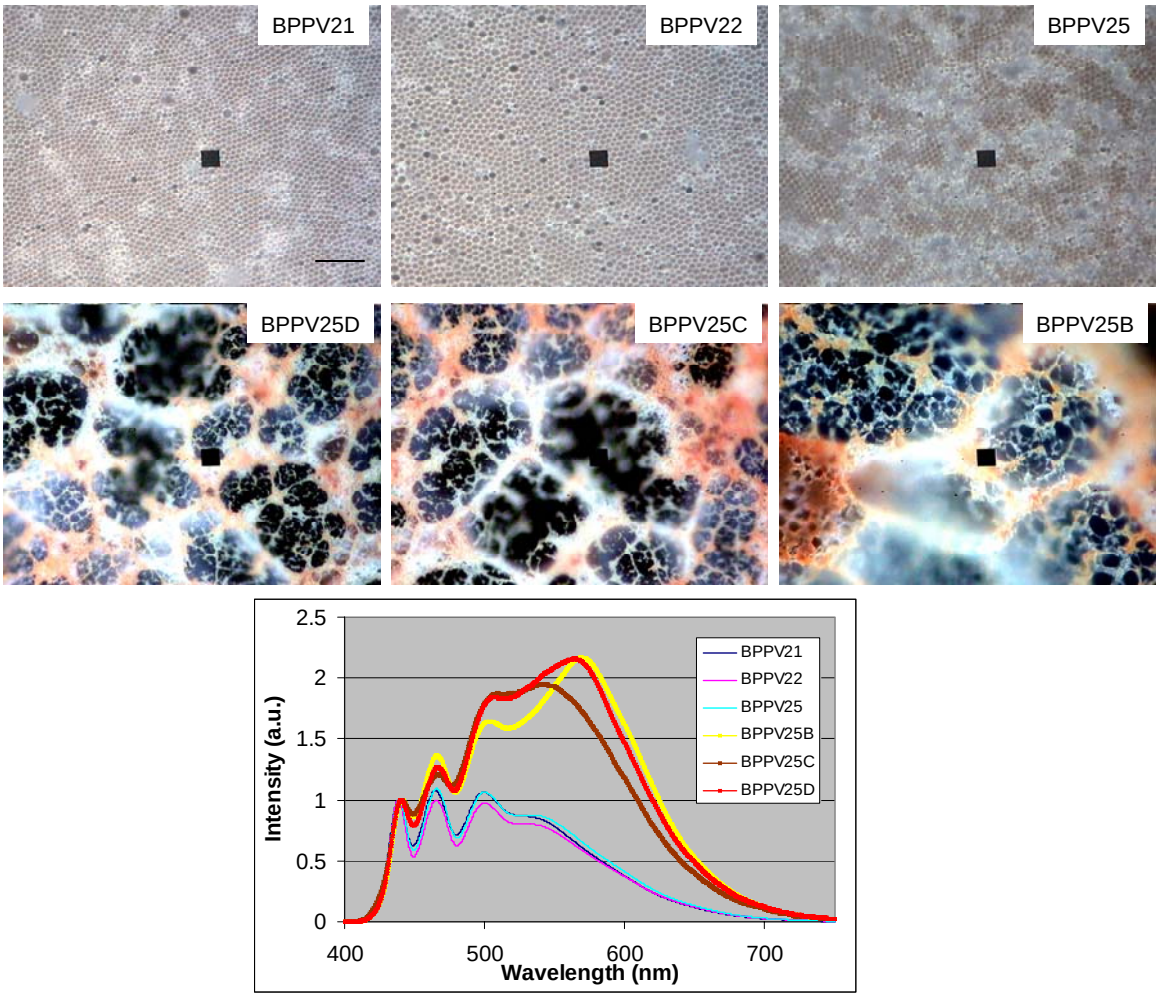

Figure 4.34 Fluorescence micrographs and spectra of BFAs of PFO:MEH-PPV cast from CS_2 solutions. (BPPV21 and BPPV22 stand for 0.5% and 1.0% MEH-PPV samples, respectively. The other four images were taken from different areas of the same 4.0% MEH-PPV sample. Scale bar = 12 μm).

fluorescence microscopy images presented in **Figure 4.34** indicate a low MEH-PPV content in areas where uniform bubble arrays are formed. Yet, in regions of disordered bubbles, MEH-PPV is concentrated in patches and the "film" appears to be composed of more than one layer of bubbles. In fact, in areas of high MEH-PPV density, a layer of air bubbles of large size (c.a. 7-20 μm) is formed on top of a layer of bubbles of smaller dimension (c.a. 2 μm) as evidenced from the microscopy images in **Figure 4.35**. Thus the redistribution of the blend composition caused by hydrodynamic flow, which, in turn, is a result of airflow and evaporative cooling of the surface of the blend solution, has the following effects. First, in areas where the blend concentration sustains an appropriate viscosity, well-ordered bubble arrays are formed with little phase separation. However, even in these areas, a significant fraction of MEH-PPV has been driven away by

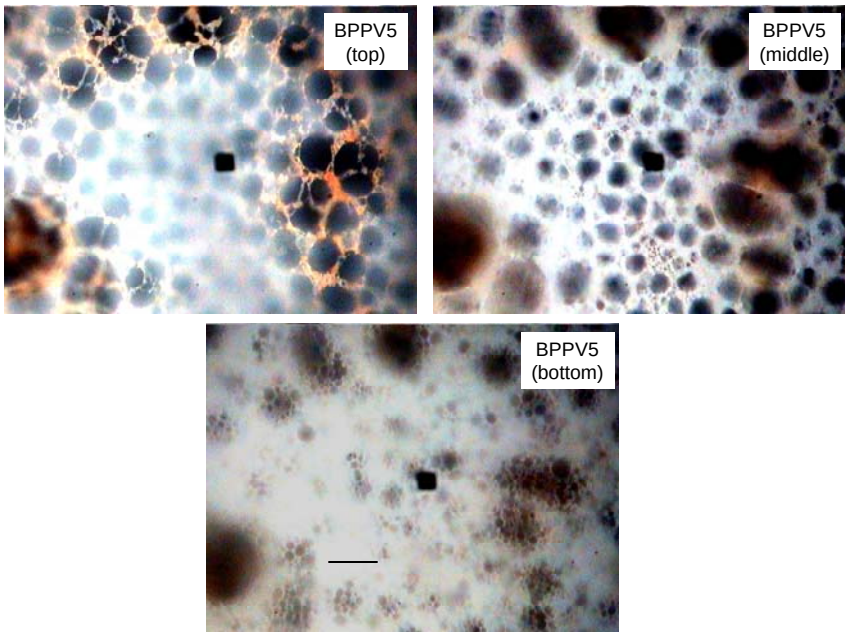

Figure 4.35 Fluorescence microscopy images of a BF-structured sample of PFO:MEH-PPV at different depths. (4.0% MEH-PPV. Scale bar = 12 μm).

hydrodynamic flow prior to the formation of the polymeric bubble arrays, resulting in little fluorescence of MEH-PPV as shown in **Figure 4.34** (sample BPPV25). Second, the flow dynamics concentrates MEH-PPV in areas where a layer of bubble arrays has been established. The excess material, being more concentrated, either does not facilitate the formation of a layer of bubble arrays (**Figure 4.34**, second row) or enables the production of large and disordered bubbles (**Figure 4.35**). Ultimately, phase separation in the BFAs of PFO:MEH-PPV blends is dictated by non-uniform redistribution of the blend components as driven by airflow, solvent evaporation, and surface cooling. However, the effects of these factors on phase separation are limited by the non-equilibrium state of the system resulted from rapid solvent evaporation and, consequently, a significant fraction of donor and acceptor molecules in close proximity is maintained and the overall energy transfer efficiency is relatively high.

The morphology of the PFO:MEH-PPV films drop-coated from CS_2, on the other hand, appears to be determined by the segregation of the blend components and partial crystallization of PFO (**Figure 4.36**). The phase behavior is thus similar to what has been observed in the PFO-P3HT films prepared from the same solvent. An absence of MEH-PPV crystals can be safely assumed as the emissions from the films are not red-shifted enough to even resemble the emission peak of an unblended MEH-PPV film, let alone the emission from a crystalline film. However, the crystallization of PFO is expected since it is observed in a separately prepared set of drop-coated films of PFO:MEH-PPV blends and confirmed by XRD measurements (**Figures 4.37 & 4.38**).

Previous study on spin-coated films of PFO:MEH-PPV from chloroform solutions claimed a phase separation by spinodal decomposition,[31] which is not observed in the

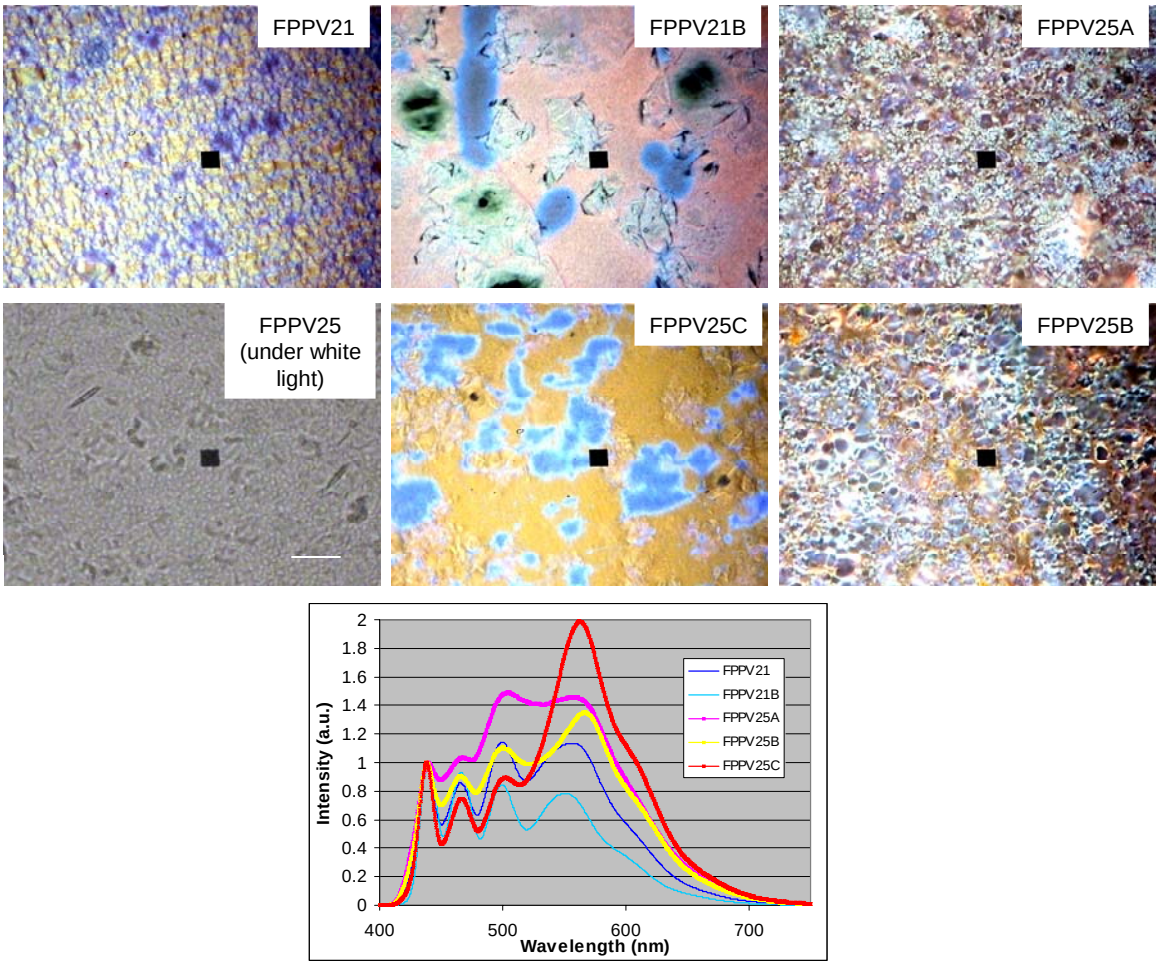

Figure 4.36 Fluorescence micrographs and spectra of PFO:MEH-PPV DFCs cast from CS_2 solutions. (Images FPPV21 and FPPV21B were taken from a 0.5% MEH-PPV film. The other four images were taken from a 4.0% MEH-PPV film. Image FPPV25 was taken under transmission mode. Scale bar = 12 μm).

films drop-coated from CS_2 solutions being reported here. However, a pattern resembling spinodal dewetting is observed in films of FPO:MEH-PPV under optical microscopy using transmission mode as shown in **Figure 4.36**. With that said, it is rather difficult to observe the complete dynamics of phase separation in non-equilibrium systems such as the drop-coated films here where the rapid evaporation of CS_2 does not allow a single

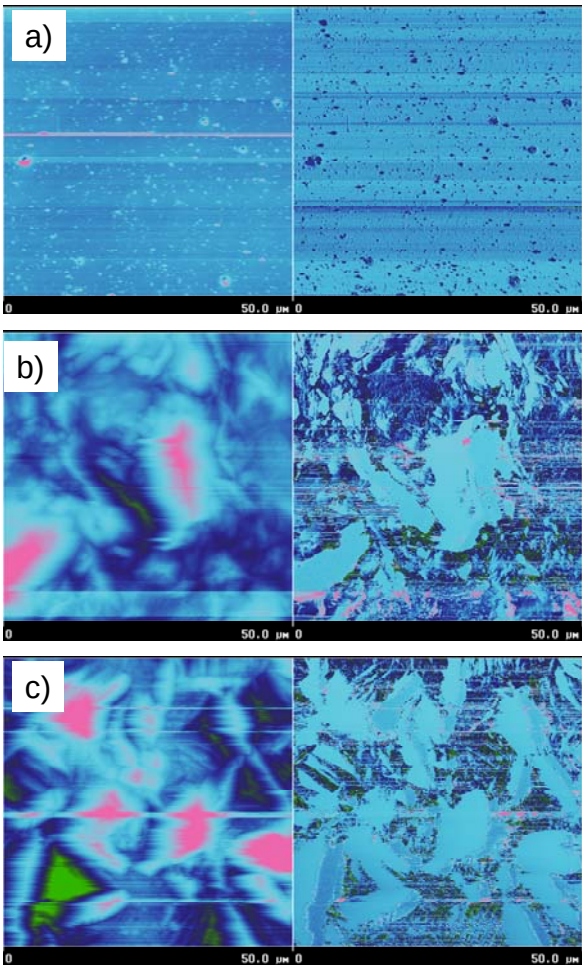

Figure 4.37 AFM images of PFO:MEH-PPV DCFs. MEH-PPV (a), PFO (b), 4.0% MEH-PPV in blend with PFO (c). Height images (left) and phase images (right). Samples were prepared from 0.23 wt% polymer solutions in CS_2. M_n of PFO is 56.4 kg/mol.

phase separation mechanism such as spinodal decomposition or nucleation and growth to exert its full effects. Whatever the mechanism may be, the PFO:MEH-PPV films drop-coated from CS_2 solutions are found to be phase separated by the segregation of the blend components with certain degree of crystallization by the PFO component. Such film morphology accounts for the slightly lower ET efficiency compared to the breath figure counterparts. Moreover, the formation of PFO crystals suggests that the fluorescence of

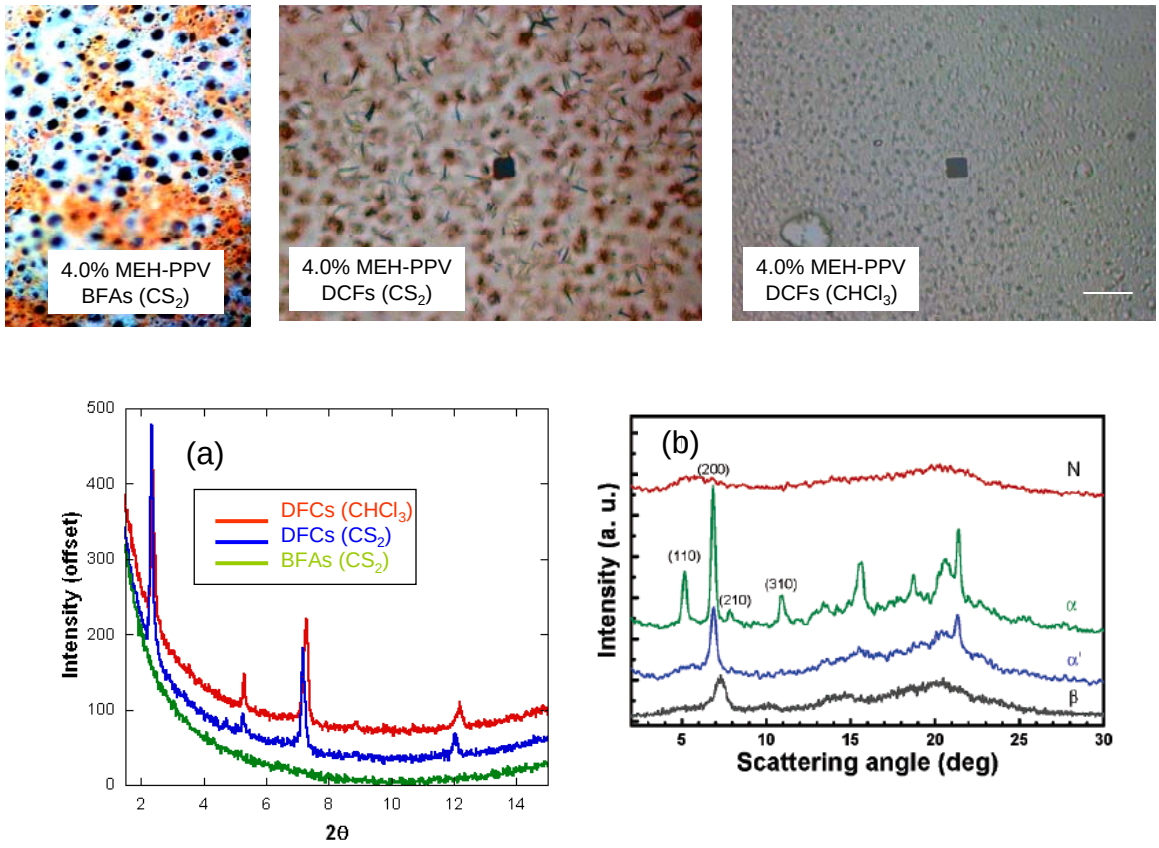

Figure 4.38 Fluorescence micrographs and the corresponding X-ray diffraction patterns of PFO:MEH-PPV BFAs and DCFs cast from 0.23 wt% blend solutions in CS_2 and $CHCl_3$. (PFO of M_n 56.4 kg/mol was used. Figure in *b* shows XRD profiles of PFO in different phases and is copied from reference 23). Scale bar = 12 μm.

PFO can also be quenched by exciton migration and lattice relaxation.[19] As in the case of PFO-P3HT blends, the longer solvent evaporation time involved in the preparation of the drop-coated films enables the blend components to phase separate by aggregation and crystallization. However, if solvent evaporation rate were the only factor determining film morphology, we would expect the ET efficiency to be much lower and phase separation to be more extensive in the films prepared from chloroform solutions. As the data presented in the next section will show, the situation is not so straightforward.

4.5.2.2 *PFO:MEH-PPV samples cast from $CHCl_3$ solutions*

The energy transfer efficiency as judged from the fluorescence spectra (**Figure 4.39**) is higher in the BFAs than the DCFs cast from chloroform solutions, in similarity to the PFO-P3HT samples. Additionally, the intensity of the acceptor emission is generally greater in samples prepared from $CHCl_3$ than those fabricated from CS_2. Such a trend implies that the rate of solvent evaporation is not the only factor determining the underlying morphology since chloroform evaporates slower than CS_2 and one would expect phase separation to be more extensive and energy transfer efficiency to be significantly reduced in the $CHCl_3$-cast samples. Perhaps, the blend components are more soluble in $CHCl_3$ and are not segregated to the extent observed in the CS_2-cast samples. However, the solubility factor seems to be relevant only to the breath figure samples as it fails to explain the highly reduced acceptor fluorescence in the $CHCl_3$-cast DCFs of PFO-P3HT blends (**Figure 4.23b**). This matter will be discussed further when morphology is studied with fluorescence microscopy.

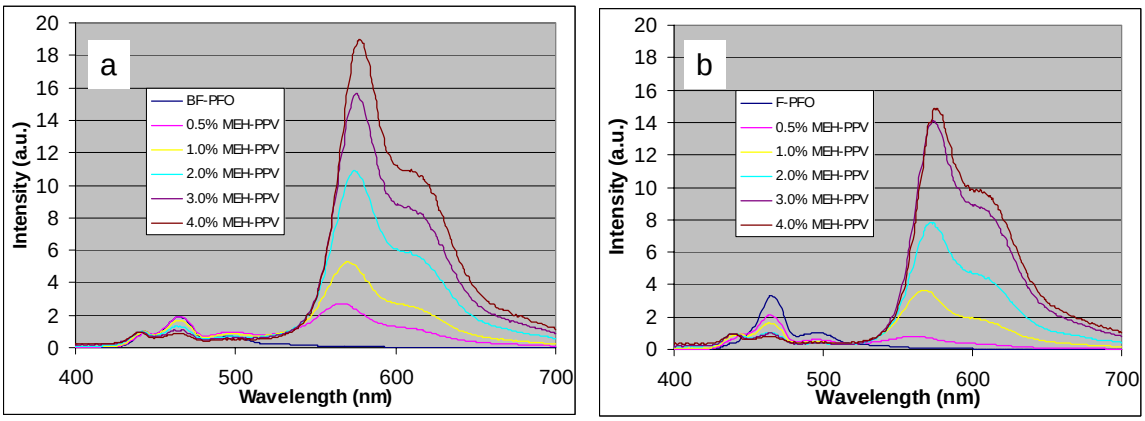

Figure 4.39 Fluorescence spectra of BFAs (a) and DCFs (b) of PFO:MEH-PPV blends cast from $CHCl_3$ solutions.

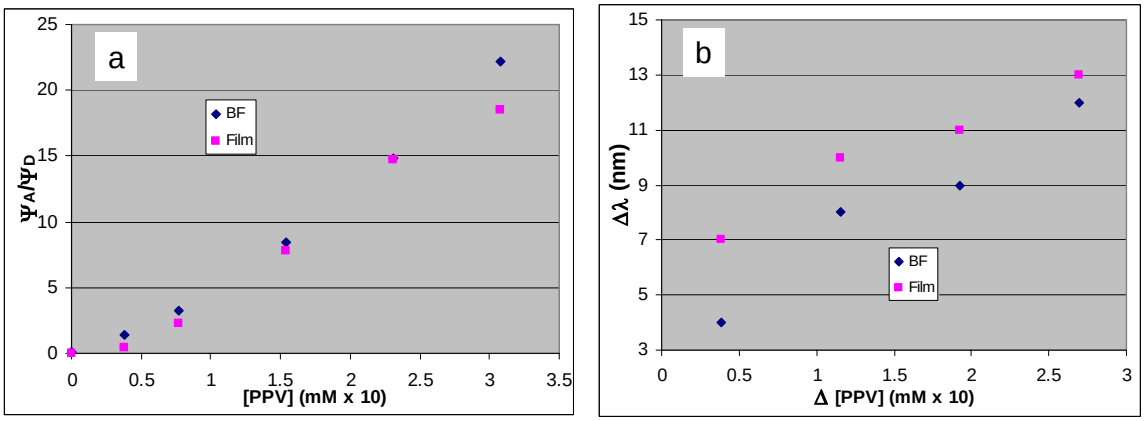

Figure 4.40 Acceptor-donor emission intensity ratio plots (a) and relative redshifts in MEH-PPV emission maxima (b) of PFO:MEH-PPV samples prepared from $CHCl_3$.

Although energy transfer is more effective in the BFAs than the DCFs, the quenching of PFO fluorescence in the latter is quite significant as indicated by the acceptor-donor emission intensity ratio plots (**Figure 4.40a**) and the Stern-Volmer plots (**Figure 4.42a**). Again, errors from the PFO non-uniform emission intensity ratios (mostly resulted from a highly reduced intensity of the 0-0 peak in the drop-coated films)

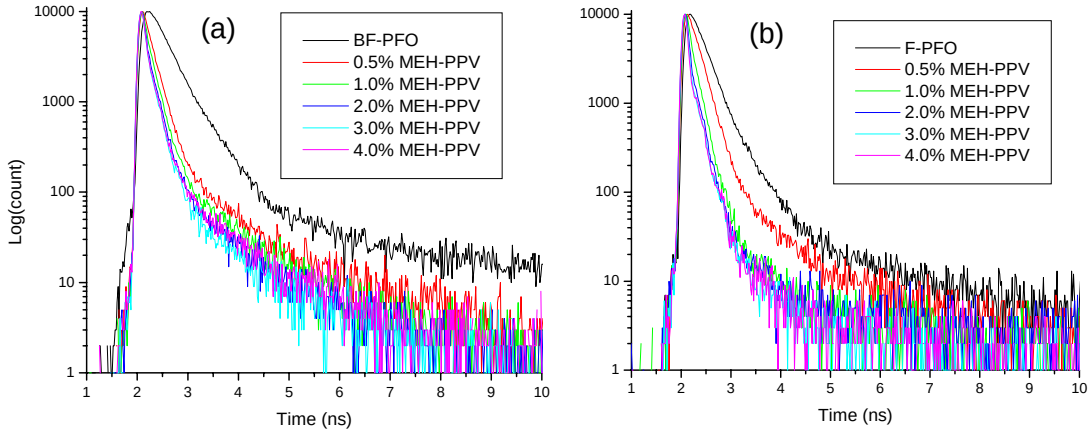

Figure 4.41 Excited-state decay profiles of BFAs (a) and DCFs (b) of PFO:MEH-PPV samples cast from $CHCl_3$ solutions.

Table 4.4 Excited-state lifetimes of PFO:MEH-PPV samples prepared from $CHCl_3$.

MEH-PPV (wt%)	τ (ps) BFAs	τ (ps) DCFs
0	351.7	248.7
0.5	131.1	140.7
1.0	99.7	87.6
2.0	72.7	50.4
3.0	62.7	37.5
4.0	64.7	30.3

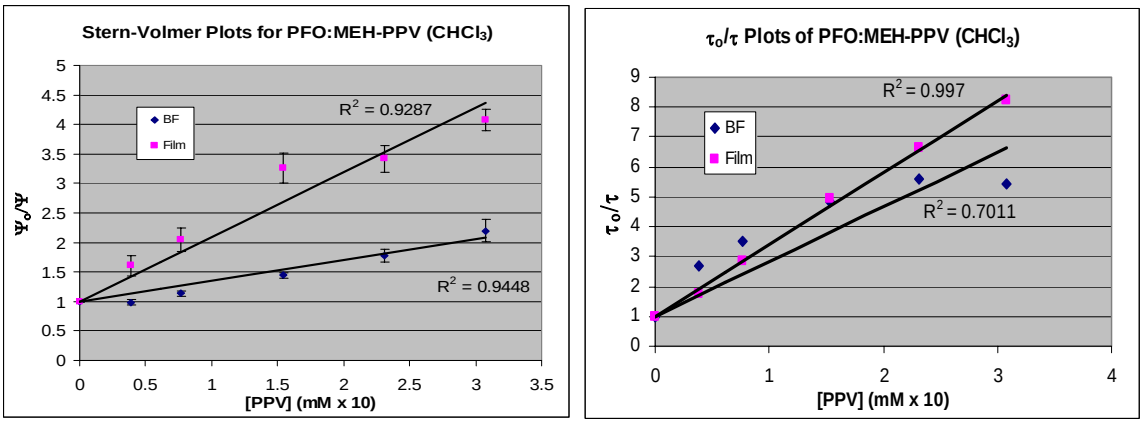

Figure 4.42 Stern-Volmer and τ_o/τ plots for PFO:MEH-PPV samples cast from $CHCl_3$.

may play a role in the observed quenching behavior. However, the effective quenching of PFO fluorescence in the DCFs is, in deed, revealed by excited-state lifetime measurements (**Table 4.4 and Figures 4.41b & 4.42b**). Similar to the samples prepared from CS_2 solutions, the low ET efficiency coupled with a high rate of donor fluorescence quenching in the DCFs seemingly points to the existence of acceptor aggregation and donor crystallization where the latter process enables PFO to self-quench by exciton migration and lattice relaxation. In fact, the aggregation of MEH-PPV is suggested by its progressively red-shifted emissions (**Figure 4.40b**) and the presence of PFO crystals is confirmed by XRD (**Figure 4.38**). These findings from fluorescence measurements will

now be correlated with the morphology of the samples as observed under fluorescence microscope and AFM.

The microscopy images of the surfaces of the BFAs as shown in **Figure 4.43** display well defined donor-rich and acceptor-rich domains, which clearly indicate the prominent role of hydrodynamic flow in the phase separation of the blend components. Thus, during the breath figure formation, processes such as airflow, evaporative cooling of the polymer solution surface, and solvent evaporation redistribute the blend composition laterally. However, phase separation in the direction perpendicular to the film surface is minimal as the rims of the bubbles in the acceptor-rich domains display

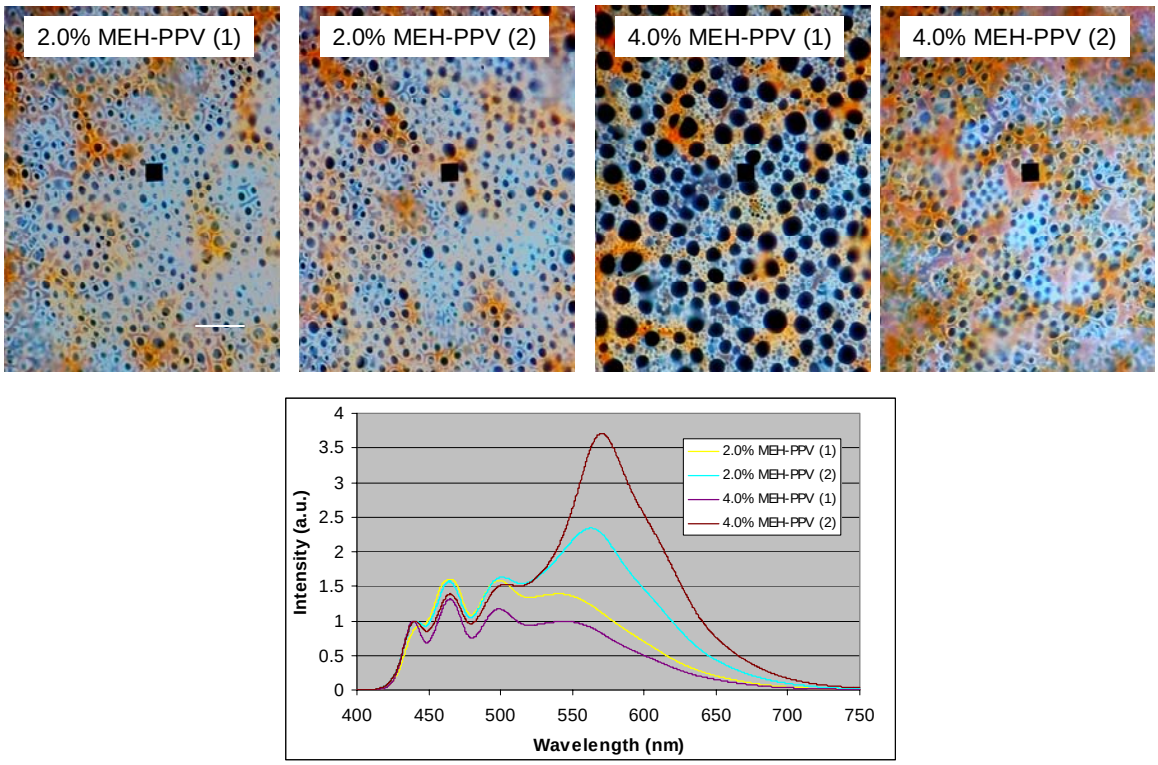

Figure 4.43 Fluorescence micrographs and spectra of PFO:MEH-PPV BFAs cast from $CHCl_3$ solutions. (The numbers in parentheses indicate different measurements on the same samples.) Scale bar = 12 μm.

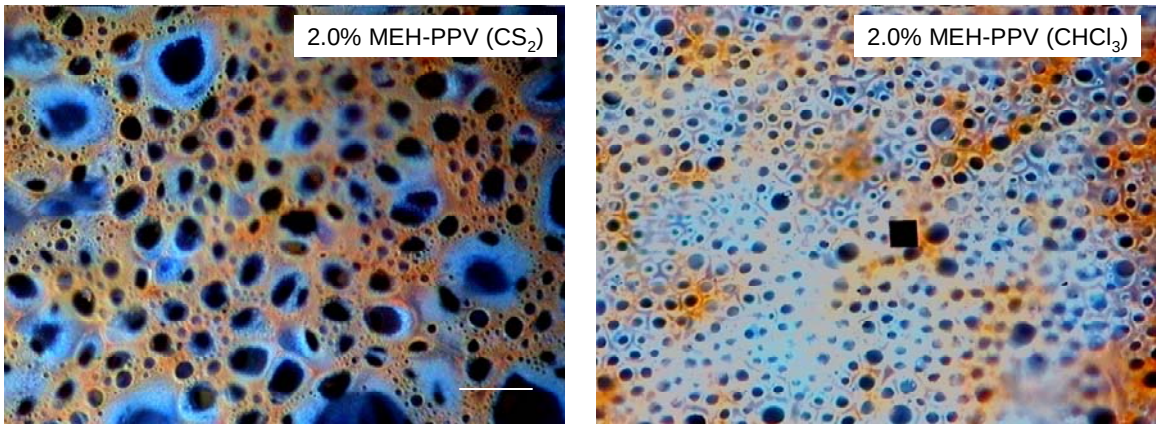

Figure 4.44 Fluorescence micrographs of PFO:MEH-PPV BFAs. (Left image: 0.23% blend solution where M_n of PFO is 56.4 kg/mol). Scale bar = 12 μm.

orange-red color, which comes from MEH-PPV fluorescence, but not the blue color that represents PFO (**Figure 4.44**, right). This is in contrast to the behavior observed in the BFAs cast from CS_2 where the rims of the bubbles are mainly decorated with blue color, suggesting that most of MEH-PPV forms a layer on top of a PFO-rich substrate-adhering layer (**Figure 4.44**, left). The limited phase separation in the vertical direction in the breath BF-structured films of PFO:MEH-PPV cast from $CHCl_3$ solutions not only explains the high efficiency in the energy transfer but also reveals the important impacts of solubility and solvent polarity on the film morphology. Since both PFO and MEH-PPV are more soluble in $CHCl_3$ than CS_2 and MEH-PPV is more soluble in CS_2 than PFO does in the same solvent, it is more likely for MEH-PPV in a blend with PFO in CS_2 to phase separate near the top of the becoming film due to the evaporative cooling effect. Moreover, carbon disulfide is non-polar while chloroform is polar and therefore the interaction of the latter with the hydrophilic substrate (glass) surface is expected to be stronger than that between CS_2 and the substrate. Consequently, it is a likely scenario that

as CS_2 is evaporating, PFO becomes more concentrated near the substrate surface while a considerable fraction of MEH-PPV is carried by CS_2 away from the substrate and redistributed laterally by the hydrodynamics, which comes from the airflow and the temperature gradient on the surface of the blend solution. In the case of $CHCl_3$ solution, the stronger solvent-substrate interaction and the higher solubility of the blend components in this solvent limit vertical phase separation as both factors minimize the partition of the blend components in the vertical direction. However, lateral phase separation is subjected to the same dynamics as in the case of CS_2.

The rate of solvent evaporation seems to play a more prominent role in the drop-coated films than in the breath figures as the blend components have more time to segregate and form aggregates as shown in **Figure 4.45**. However, while changing the solvent from CS_2 to $CHCl_3$ has a dramatic impact on the ET efficiency of the PFO-P3HT drop-cast films (**Figures 4.12b & 4.23b**), it exerts negligible effects on the fluorescence profiles of the PFO:MEH-PPV counterparts (**Figures 4.30b & 4.39b**). If anything, the energy transfer in the films of PFO:MEH-PPV cast from $CHCl_3$ is slightly more effective than in those prepared from CS_2. Perhaps, the compatibility of PFO and MEH-PPV is better in $CHCl_3$ than in CS_2, and that of PFO and P3HT is reduced in $CHCl_3$. In other words, the same solvent effects as seen in the BFAs of PFO:MEH-PPV blends may also play a part in the drop-coated films and result in more vertical phase separation in the CS_2-cast films than in the films prepared from $CHCl_3$. Whether such phase behavior exists in the films remains to be confirmed by depth profile analysis. What is more certain is the partial crystallization of PFO in the $CHCl_3$-cast films. This is not obvious from the images presented in **Figure 4.45** but clearly seen from the atomic force

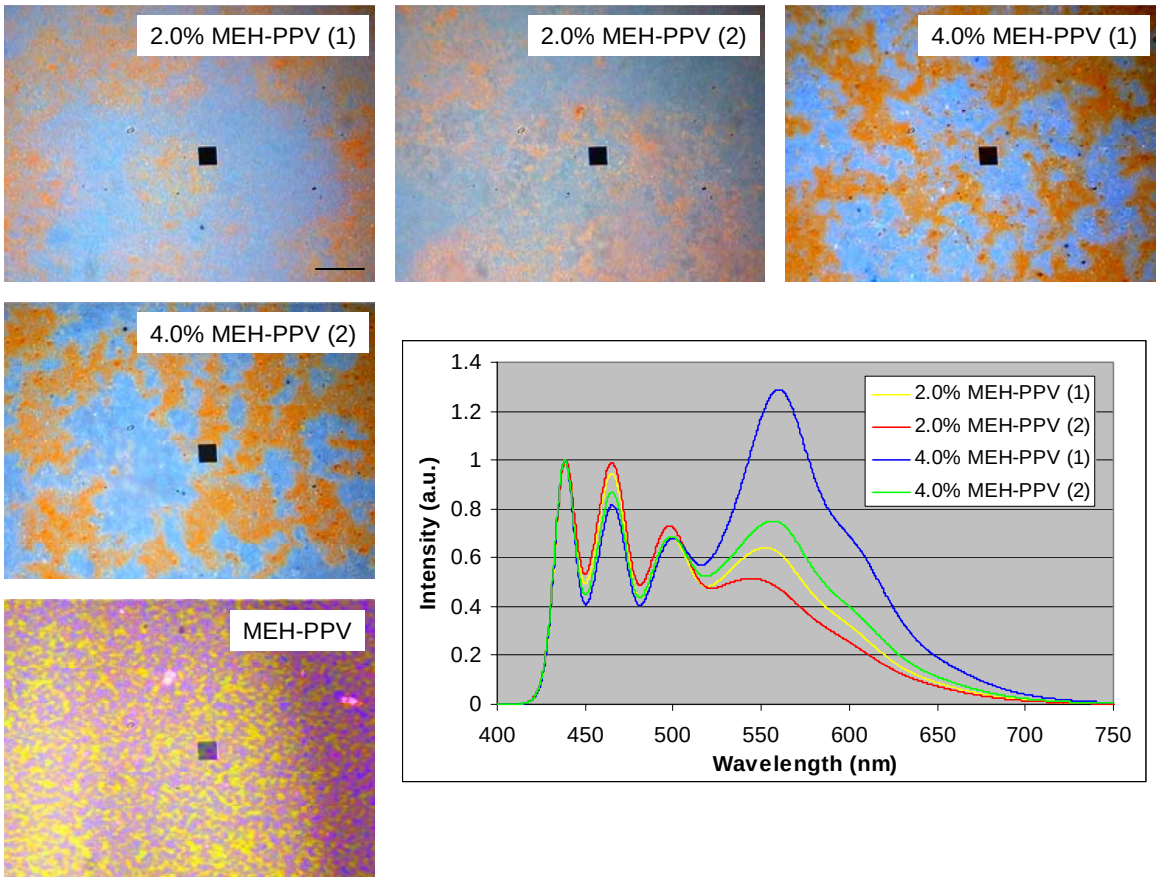

Figure 4.45 Fluorescence micrographs and spectra of PFO:MEH-PPV DCFs cast from $CHCl_3$. (Numbers in parentheses indicate different measurements on the same samples. MEH-PPV is from a drop-coated film of unblended MEH-PPV). Scale bar = 12 μm.

micrographs (**Figure 4.46**) and confirmed by XRD (**Figure 4.38**). The formation of PFO crystals may enable PFO relaxation from its excited state by interchain exciton migration and lattice relaxation and contribute to the effective quenching of PFO fluorescence as discussed above.

While it does not make much sense to classify the phase behavior in the PFO:MEH-PPV drop-coated films from $CHCl_3$ solutions as either spinodal decomposition or nucleation and growth (Chapter 3) since the aggregation of the blend

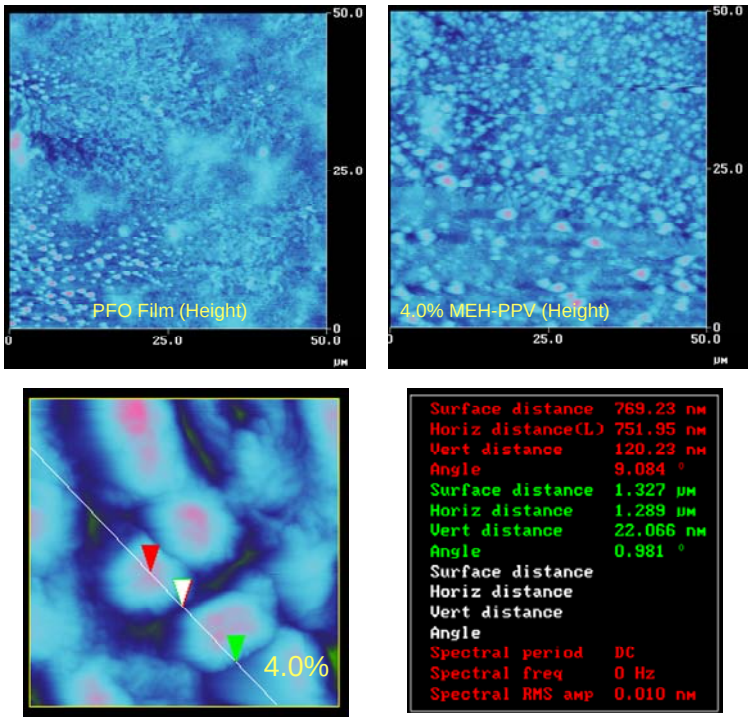

Figure 4.46 AFM images of unblended PFO film and 4.0% MEH-PPV blended film drop-coated from 0.23% polymer solutions in $CHCl_3$. (M_n of PFO is 56.4 kg/mol).

components does not follow any particular patterns, it is worth noting that the morphology of the unblended MEH-PPV film cast from $CHCl_3$ displays features that resemble spinodal dewetting (**Figure 4.45**, bottom image). However, drop-coated films of MEH-PPV in blend with PFO do not display such features but, instead, show random segregation of MEH-PPV and small crystals of PFO. Since so much of energy transfer and phase behaviors depend on the compatibility of the blend components with one another and with the solvents, it would be interesting to study these properties when PFO is blended with a small molecule which possesses a viscosity that is negligible compared to that of P3HT or MEH-PPV and an extremely high solubility in both CS_2 and $CHCl_3$.

To this end, blends of PFO-TPP were prepared and studied, and the results will now be presented and discussed.

4.5.3 PFO-TPP

The use of a monomeric energy acceptor such as TPP instead of the polymeric ones was observed to have a negative impact on the formation of well-ordered breath figure arrays of the PFO-TPP blends as mentioned earlier in this chapter. Whether the effects come from the higher diffusibility of TPP or from the lower overall viscosity of the blend solutions are not clear. Prior studies of this blend system were mainly concerned with either device performance or using it as a model for an investigation into the Förster-type energy transfer process.[19,21] However, phase separation behaviors of thin films of TPP blended with a conjugated polymer are poorly understood. Additionally, the energy transfer process and the morphology of TPP-doped polymer breath figures are not known. These issues will now be addressed for BFAs and DCFs of PFO-TPP blends prepared from CS_2 and $CHCl_3$ solutions.

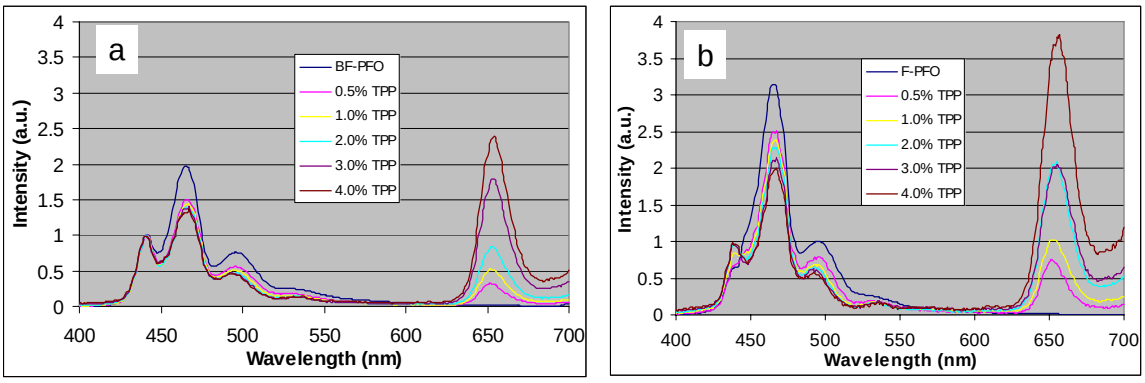

Figure 4.47 Fluorescence spectra of PFO-TPP BFAs (a) and DCFs (b) prepared from CS_2 solutions. (Excitation at 360 nm).

4.5.3.1 PFO-TPP samples cast from CS_2 solutions

The relative TPP fluorescence intensity and PFO fluorescence quenching efficiency are surprisingly similar between the BFAs and DCFs prepared from CS_2 as evidenced from steady-state fluorescence measurements (**Figures 4.47 & 4.48)** and excited-state decay profiles (**Figures 4.49 & 4.50b**). From the ineffective quenching of PFO fluorescence by TPP, it may be inferred that energy transfer efficiency is quite low for both breath figure and drop-coated systems and significant phase separation is expected. Unlike the cases of P3HT and MEH-PPV where the aggregations of the energy acceptor components are revealed by the red-shifts of the emission peaks, the positions of the fluorescence maxima of TPP change little, regardless of its concentration.

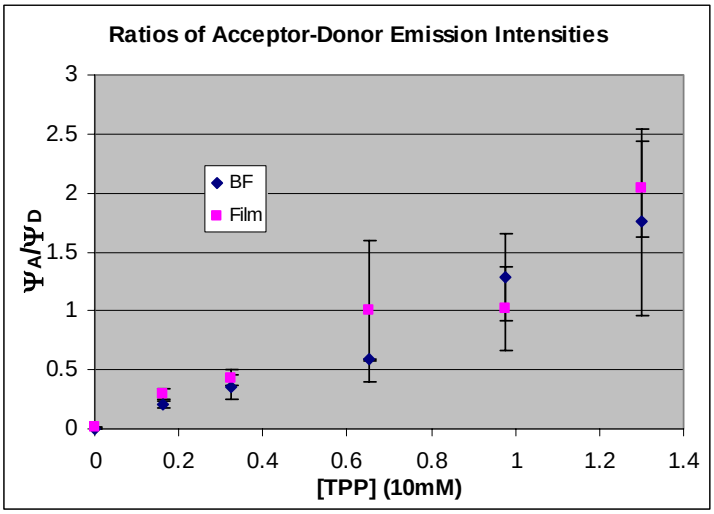

Figure 4.48 A-D emission intensity ratio plots for PFO-TPP samples cast from CS_2.

Nevertheless, the considerable errors involved in the fluorescence measurements as indicated in the acceptor-donor emission intensity ratio plots and the Stern-Volmer plots (**Figure 4.50a**) imply a great inhomogeneity of the film structures. The errors observed in

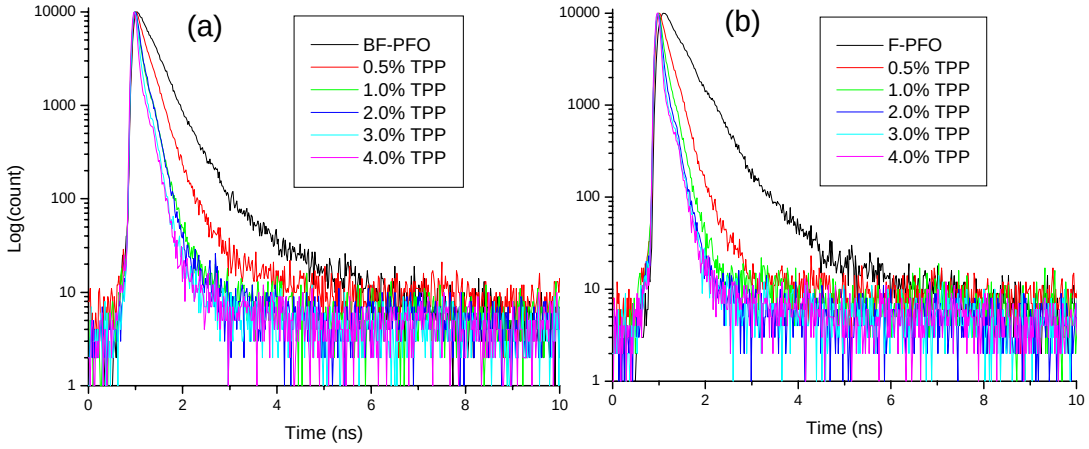

Figure 4.49 Excited-state decay profiles of PFO-TPP BFAs (a) and DCFs (b) cast from CS_2 solutions. (λ_{pump} 372 nm, λ_{probe} 466 nm).

Table 4.5 Excited-state lifetimes of PFO-TPP samples prepared from CS_2 solutions.

TPP (wt%)	τ (ps) BFAs	τ (ps) DCFs
0	306.6	405.2
0.5	142.3	125.2
1.0	62.3	83.8
2.0	59.4	46.2
3.0	55.9	34.7
4.0	24.1	27.1

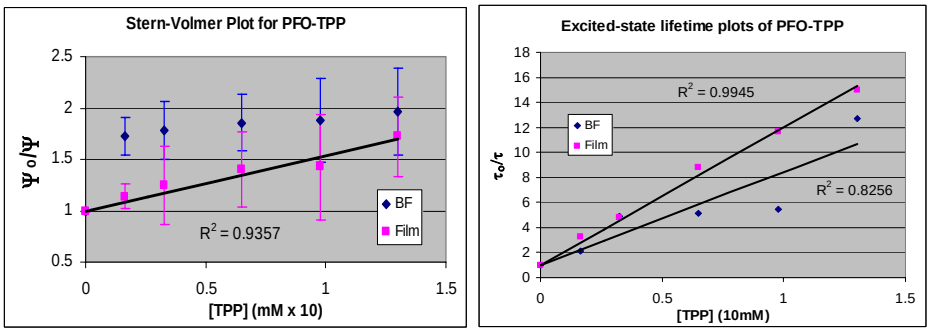

Figure 4.50 Stern-Volmer and τ_o/τ plots of PFO-TPP samples cast from CS_2.

the Stern-Volmer plots also come from the unpredictable behavior of the three PFO emission peaks. For some unknown reason, the inconsistency in the relative intensities of the PFO emission maxima is much greater from the PFO-TPP samples in contrast to the PFO-P3HT and PFO:MEH-PPV ones. Thus, while the quenching of PFO fluorescence by TPP in the DCFs is shown by the Stern-Volmer plots to be less efficient than that in the BFAs, the rate at which PFO decays from its excited state is faster in the films than in the breath figures (**Figure 4.50b**). In other words, according to the data from the pump-probe measurements, PFO fluorescence in the DCFs is heavily quenched while relatively little energy is transferred from the donor to the acceptor. This behavior, which has also been observed in the drop-coated films of PFO-P3HT and PFO:MEH-PPV blends, implies self-quenching. Partial crystallization of PFO is therefore expected in the DCFs.

The inhomogeneity in the structures of the BFAs as suggested by the fluorescence measurements is clearly revealed by optical microscopy, which displays well-defined PFO-rich and TPP-rich domains (**Figure 4.51**). These phase separation features have been observed repeatedly in different sets of PFO-TPP breath figures (**Figure 4.52**). The fluorescence spectra obtained at the red-colored domains or the blue-colored ones show significant fluorescence from PFO, indicating that even the TPP-rich domains (i.e., red-colored areas) contain a considerable amount of the PFO component. It is also noted that, unlike the case of the polymer-polymer blends where the acceptor-rich domains are very often located in the sections where the bubbles are not formed, the formation of the TPP-rich domains do not have a preference on the surface. These observations suggest a mode of phase separation where TPP may have diffused to the surface during the evaporation of CS_2 and hydrodynamic flow breaks up the continuum of the TPP solution in CS_2 into

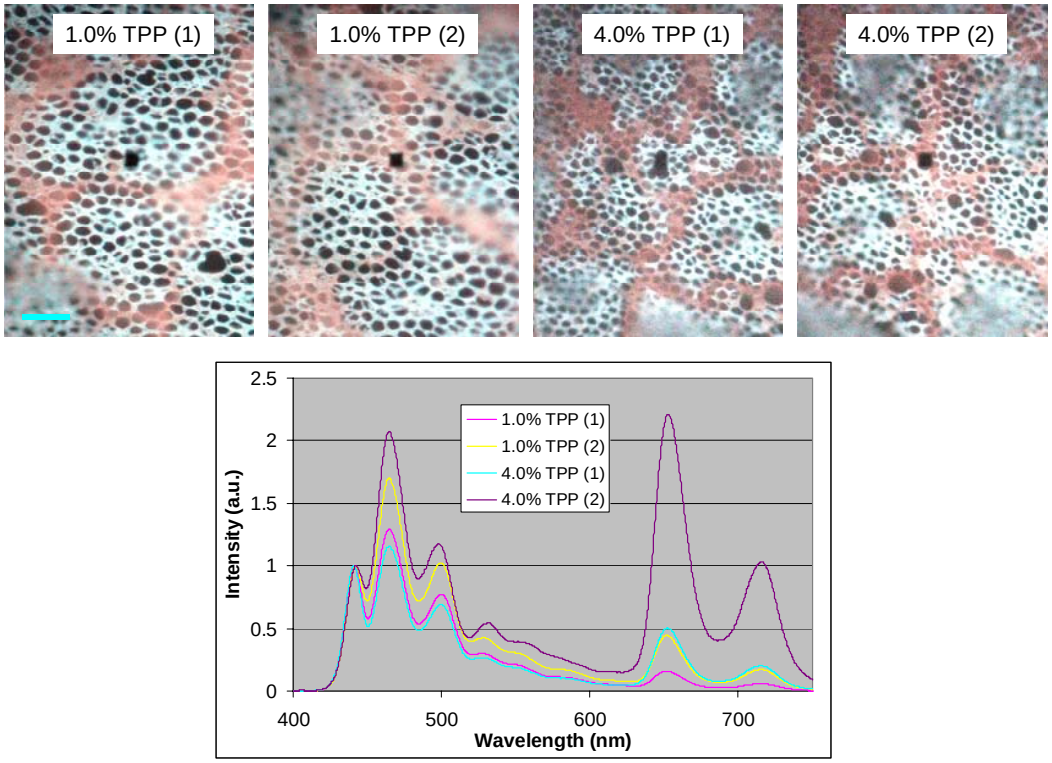

Figure 4.51 Fluorescence micrographs and spectra of PFO-TPP BFAs cast from CS_2. Scale bar = 15 μm.

patches that eventually settle on top of a thick BF-structured PFO layer. During this process, even the rims of the bubbles in the TPP-rich regions are coated on the surface with a thin layer of TPP. Of course, only a fraction of TPP was carried by the solvent to the surface during the breath figure formation process because significant TPP fluorescence is observed in the PFO-rich domains. The relatively low energy transfer efficiency as observed in **Figure 4.47a** and the high standard deviations associated with fluorescence measurements are thus correlated with a morphology where large-scale lateral phase separation driven by TPP's high diffusibility and hydrodynamic flow is extensive. Phase behavior in the DCFs is quite different, however.

The fluorescence microscopy images of PFO-TPP DCFs display features that are

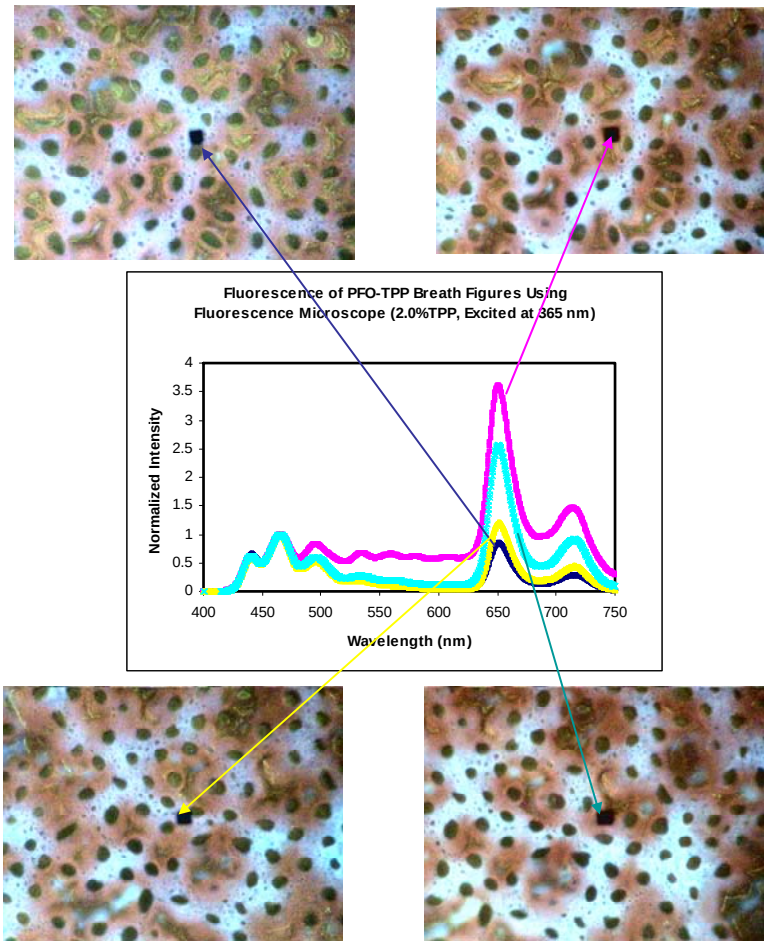

Figure 4.52 Fluorescence micrographs and spectra of PFO-TPP BFAs cast from CS_2. (0.23% final polymer concentration. M_n of PFO is 56.4 kg/mol).

shown by XRD to be PFO crystals (**Figures 4.53-4.55**). Although XRD does not validate the presence of TPP crystallization in the blend films due most likely to the low concentration of TPP crystals, this dye does form crystals in the unblended film cast from CS_2 (**Figure 4.54**, TPP) and sometimes near the edges of the blend films (**Figure 5.43**, second from left). Clearly, the crystallization-induced phase separation in the DCFs accounts for the low energy transfer efficiency observed in **Figure 4.47b**. Moreover, the formation of the PFO crystals may enable PFO to relax from its excited state by

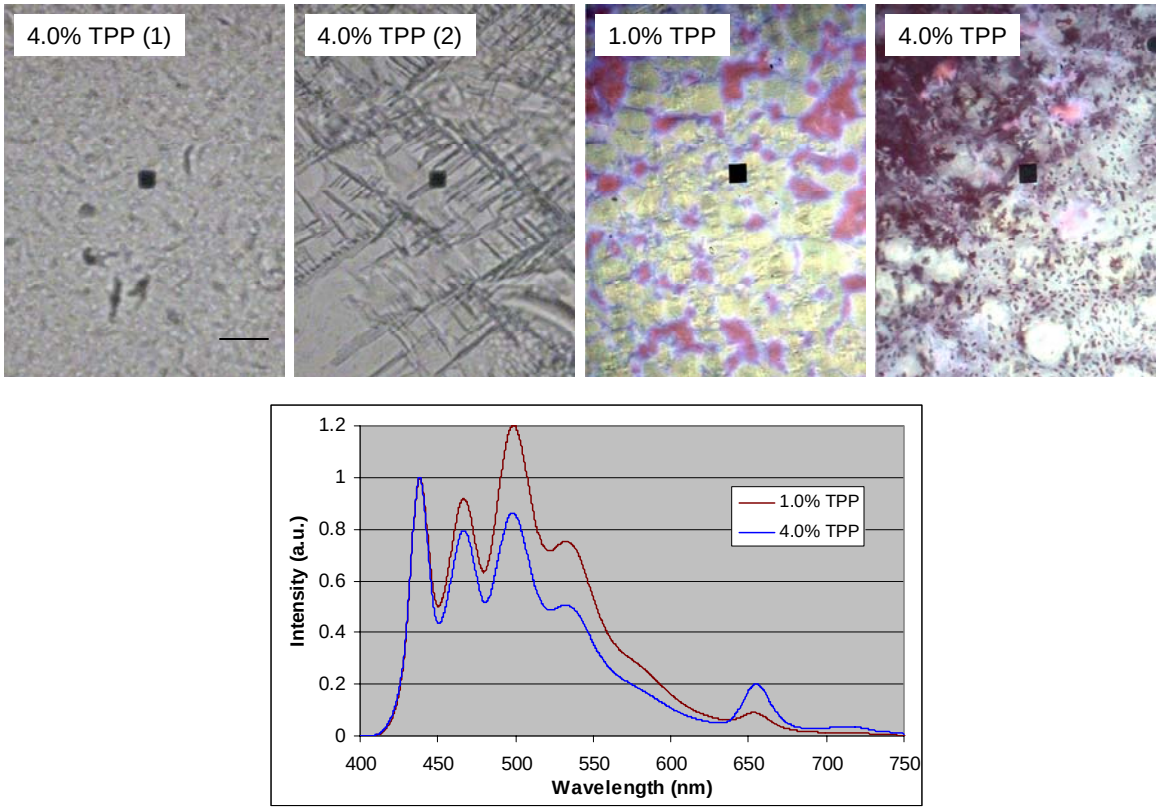

Figure 4.53 Fluorescence micrographs and spectra of PFO-TPP DCFs cast from CS_2 solutions. (The two images on the left were taken under transmission mode at different regions of the same sample). Scale bar = 15 μm.

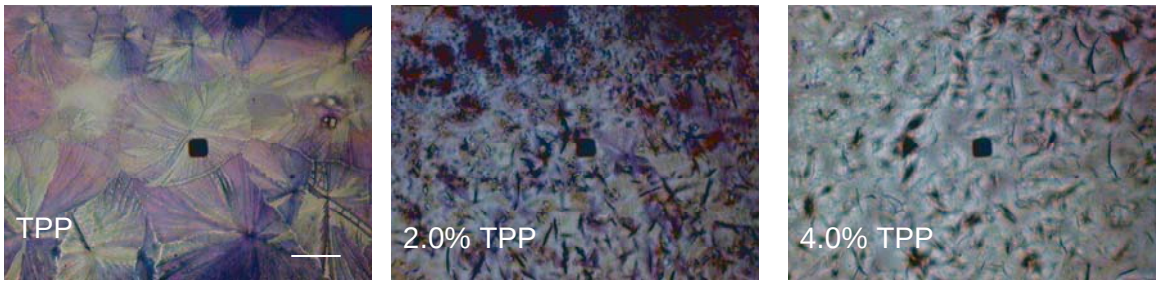

Figure 4.54 Fluorescence micrographs of PFO-TPP DCFs cast from 0.23% blends in CS_2. (The leftmost image is from an unblended DCF of TPP). Scale bar = 12 μm.

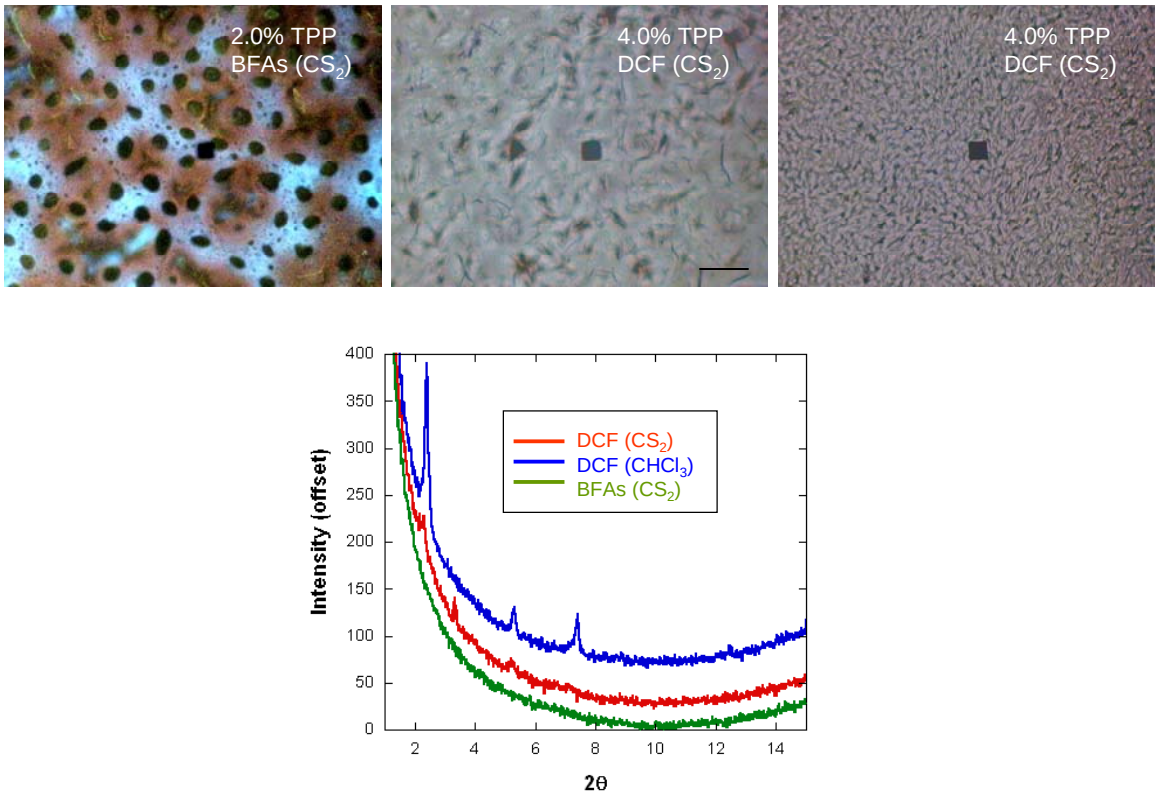

Figure 4.55 Fluorescence micrographs and the corresponding X-ray diffraction patterns of PFO:TPP BFAs and DCFs cast from 0.23 wt% blend solutions in CS_2 and $CHCl_3$. (PFO of M_n 56.4 kg/mol was used). Scale bar = 12 μm.

interchain exciton migration and lattice relaxation. These processes are reflected in the rapid rate of decay of PFO excited state as indicated by the τ_o/τ plot. The crystallization of the blend components is undoubtedly facilitated by the slow solvent evaporation rate as afforded by the drop-coating process. Accordingly, phase separation by crystallization in films drop-coated from chloroform is expected to be more extensive as this solvent evaporates slower than CS_2. However, the energy transfer behavior of the PFO-TPP BFAs and DCFs cast from $CHCl_3$ reveals more than just the effects of solvent evaporation rate on phase separation and overall morphology.

4.5.3.2 PFO-TPP samples cast from $CHCl_3$ solutions

The fluorescence spectra of the $CHCl_3$-cast breath figures and drop-coated films of PFO-TPP blends expose a number of intriguing features. First, the emission of TPP is much higher in the BFAs than DCFs even though the quenching of PFO fluorescence is quite similar between the two sets of samples (**Figures 4.56 & 4.57**). Second, the ET efficiency is significantly greater in the $CHCl_3$-cast samples than the CS_2 counterparts for

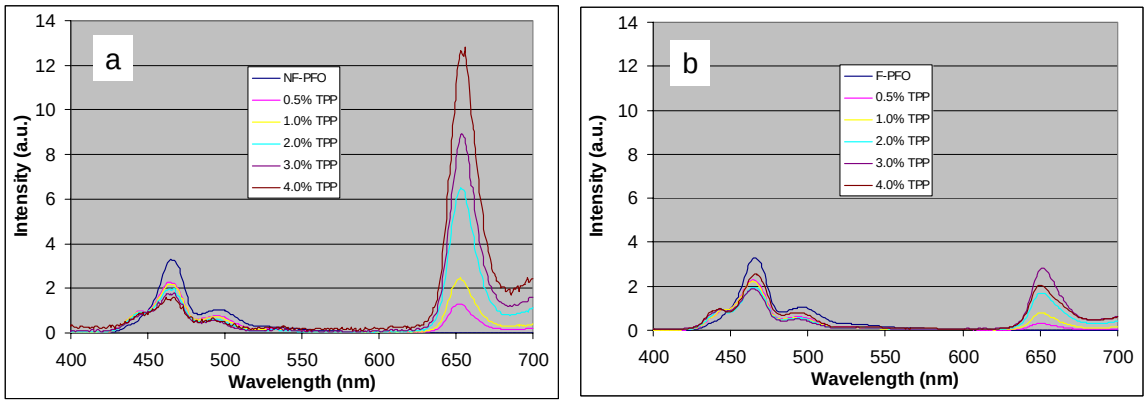

Figure 4.56 Fluorescence spectra of PFO-TPP BFAs and DCFs cast from $CHCl_3$.

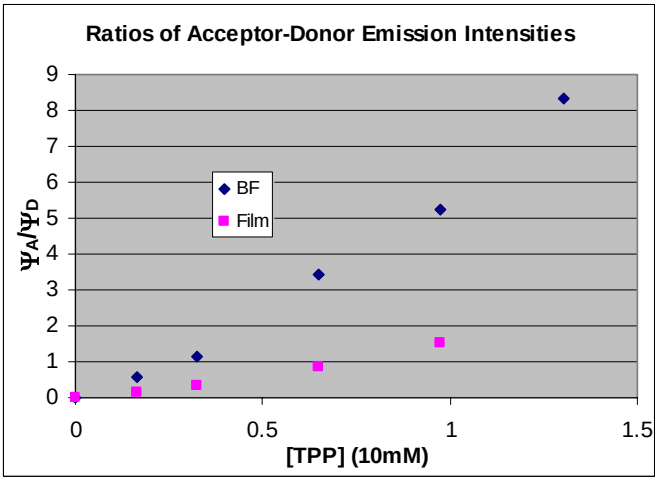

Figure 4.57 A-D emission intensity ratio plots for PFO-TPP samples cast from $CHCl_3$.

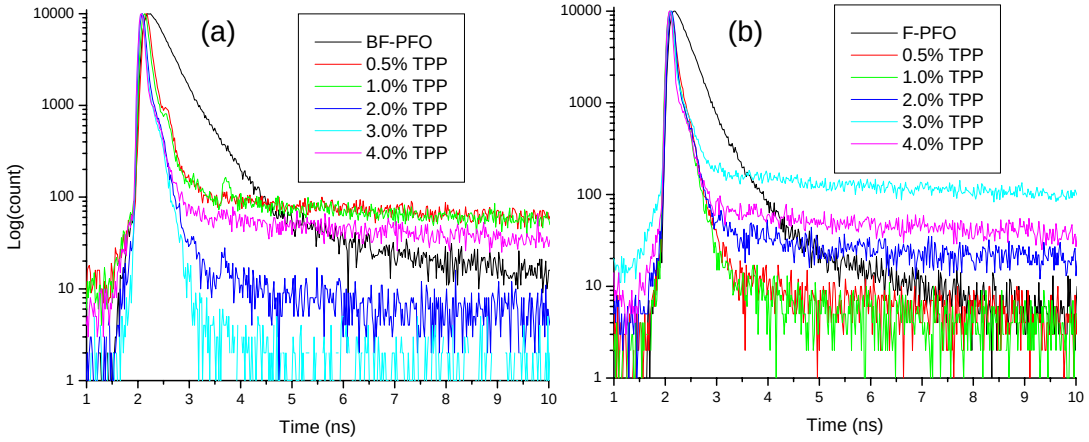

Figure 4.58 Excited-state decay profiles of PFO-TPP BFAs (a) and DCFs (b) cast from $CHCl_3$ solutions. (λ_{pump} 372 nm, λ_{probe} 466 nm).

the BFAs but is hardly affected in the DCFs by the change of solvents. The behavior shown in **Figure 4.56b**, where little energy transfer is observed in the DCFs despite the fact that PFO fluorescence is heavily quenched, can not be explained by the non-constant relative intensities of the PFO vibronic couplings because such efficient quenching is also confirmed by the excited-state lifetime measurements (**Figures 4.58b & 4.59b**). As seen in the DCFs of other blend systems as well as in the PFO-TPP DCFs prepared from CS_2, such a behavior points to a possibility of self-quenching by PFO via interchain exciton migration and implies partial crystallization of PFO. In fact, the relevance of PFO crystallization in the films drop-coated from $CHCl_3$ is supported by microscopy studies as will be shown momentarily.

Why is energy transfer more efficient in the $CHCl_3$-cast BFAs of PFO-TPP blends than in the CS_2-cast analogues? The determining factor is definitely not the solvent evaporation rate because one would expect a reverse relationship due to the fact that

Table 4.6 Excited-state lifetimes of PFO-TPP samples prepared from $CHCl_3$ solutions.

TPP (wt%)	τ (ps) BFAs	τ (ps) DCFs
0	328.4	248.7
0.5	65.4	62.3
1.0	63.8	50.2
2.0	37.4	36.7
3.0	32.3	32.4
4.0	23.1	20.9

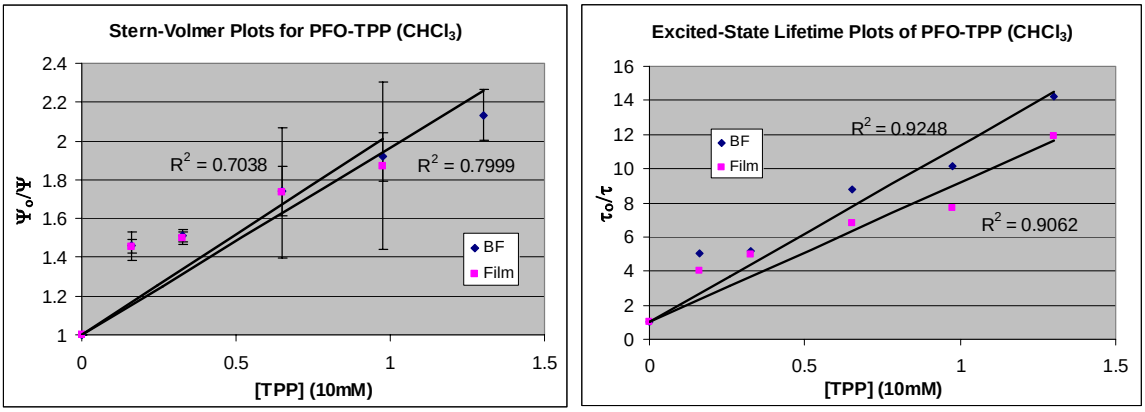

Figure 4.59 Stern-Volmer and τ_o/τ plots for PFO-TPP samples cast from $CHCl_3$.

$CHCl_3$ evaporates slower than CS_2 and, not withstanding other effects, enables material transport dynamics to exert a greater impact on phase separation. It is more likely that, whatever the morphology may be, a rather uniform distribution of the blend components is expected which results in greater donor-acceptor interactions. In fact, the phase separation behavior in the PFO-TPP BFAs is quite different as the solvent is changed from CS_2 to $CHCl_3$.

The features comprised of well-defined red and blue domains observed in the CS_2-cast BFAs are absent from the $CHCl_3$-cast samples as evidenced from the fluorescence microscopy images (**Figure 4.60**, top row). Instead, the distribution of the

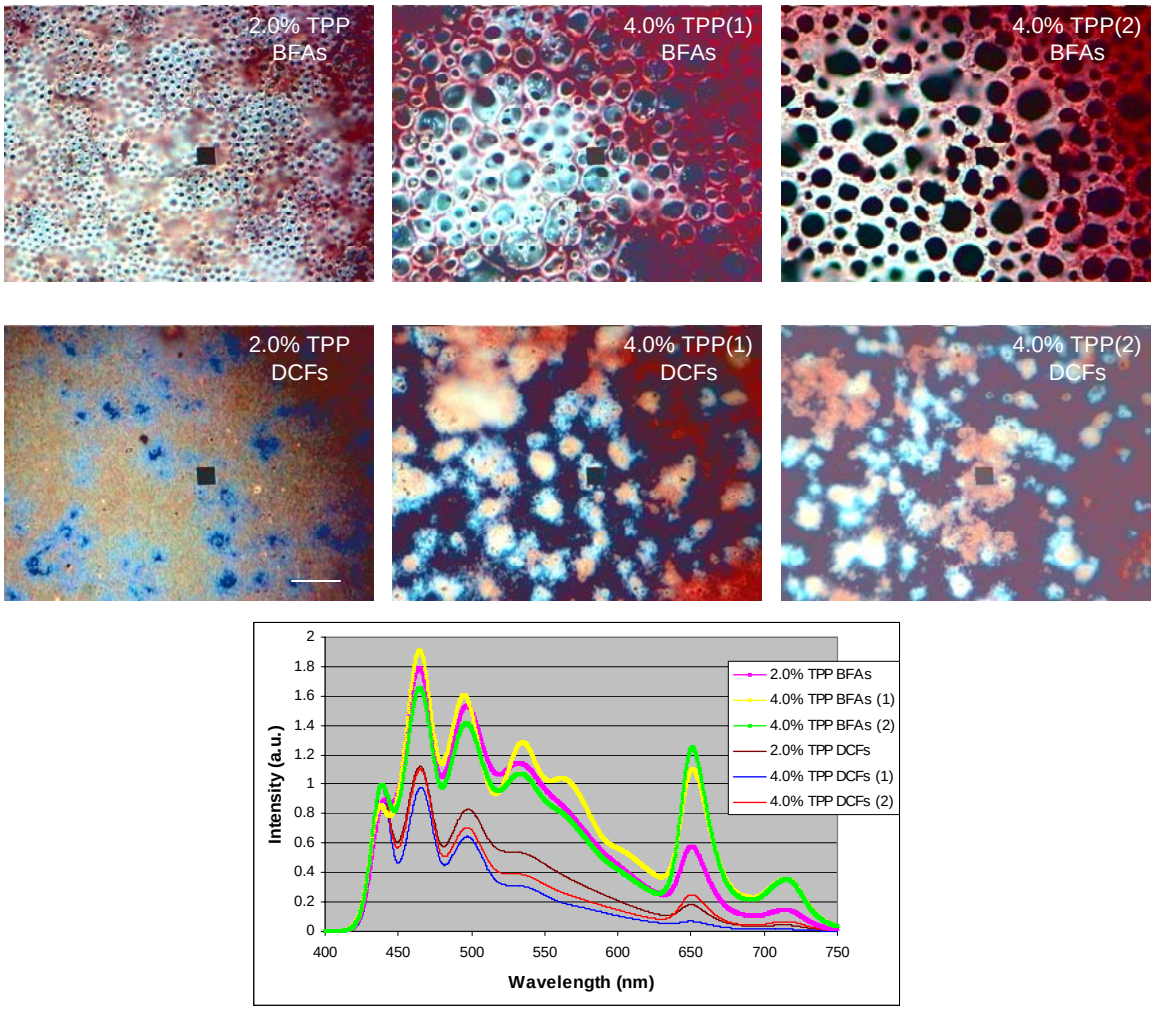

Figure 4.60 Fluorescence micrographs and spectra of $CHCl_3$-cast PFO-TPP samples. Scale bar = 12 μm.

TPP component is relatively uniform across the breath figures prepared from $CHCl_3$. The phase separation patterns suggest that the extent to which TPP diffuses to the surface and be affected by hydrodynamic flow during the formation of the bubble arrays is not as pronounced as it does in the samples cast from CS_2. Perhaps, the higher solubility of PFO in $CHCl_3$ (as apposed to CS_2) limits the partition of the blend components under the evaporative cooling effects. Moreover, the stronger solvent-substrate interactions may

have the effect of minimizing the de-mixing of the blend components in the direction perpendicular to the BF-structured films.

Phase separation in the drop-coated films, in contrast, is more extensive as indicated by the isolated areas of deep red and blue colors (**Figure 4.60**, bottom row). These features, together with a low energy transfer efficiency, suggest extensive aggregation of the blend components. Additionally, phase separation across the film thickness (i.e., in the vertical direction) is expected to be considerable because relatively little TPP fluorescence is observed in the red domains although the significant PFO fluorescence indicates the presence of PFO in these areas. In other words, little energy

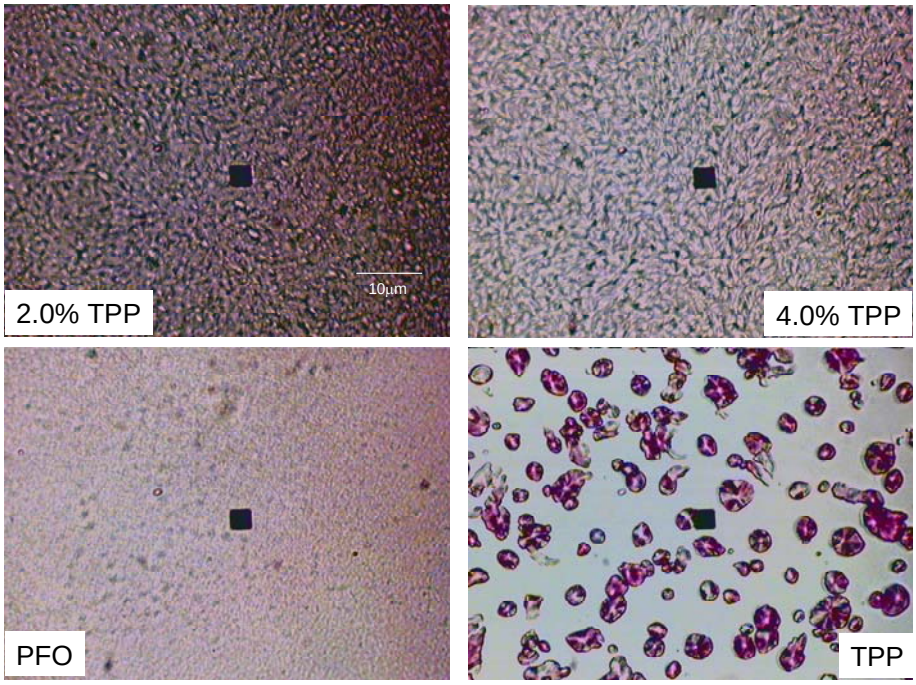

Figure 4.61 Fluorescence microscopy images of PFO-TPP films drop-coated from $CHCl_3$ solutions. (All films were prepared from solutions of 0.23% final polymer concentration. The PFO and TPP images are from unblended samples. PFO with M_n of 56.4 kg/mol was used).

transfer is effected in domains that are rich in both donor and acceptor contents. Clearly, the longer solvent evaporation time associated with the drop-coating process enables the blend components to separate and form aggregates in both vertical and lateral directions. The crystalline nature of these aggregates, although not implied in the microscopy images in **Figure 4.60**, is clearly seen in another set of samples prepared from 0.23% blend solutions in $CHCl_3$ (**Figure 4.61**). It is still not clear why in all the three blend systems the crystallization of the blend components, especially PFO, is visibly extensive in the films drop-cast from 0.23% blend solutions that used PFO with an average M_n of 56.4 kg/mol but not always observed in the films prepared from 0.2% blend solutions that employed PFO with an M_n of 12.9 kg/mol. Nevertheless, the phase separation by aggregation and crystallization of the blend components in the PFO-TPP films drop-coated from $CHCl_3$ not only accounts for the low ET efficiency but also explains the effective PFO fluorescence quenching which comes mainly from intrachain/interchain exciton migration and lattice relaxation, the two processes that are undoubtedly facilitated by the formation of PFO crystals.

4.6 Summary

The fluorescence energy transfer efficiency in the films of polymer-polymer and polymer-dye blends is found to correlate with the underlying phase-separate film morphology, which in turn depends not only on the solvent system but also on the dynamics involved in the film preparation. For the polymer blends of PFO:MEH-PPV and PFO-P3HT, the rate of solvent evaporation seems to be the determining factor in the

fluorescence energy transfer efficiency and the morphology of the drop-coated films. For the breath figures, on the other hand, the phase separation is dictated less by solvent evaporation rate and more by hydrodynamic flow, the solubility of the blend components in the solvents, and the polarity of the solvents.

During the bubble array formation process, the airflow causes the solvent to evaporate quickly and, as a result, the small difference between the evaporation times of CS_2 and $CHCl_3$ exerts little influence on the de-mixing of the blend components. However, the drop-coating process enables the solvents to evaporate more slowly and the blend components have time to phase separate by aggregation and crystallization in both vertical and lateral directions. Yet, even in these systems, the time scale of the drying process is too small for them to establish equilibrium, and the phase separation behavior resembles neither spinodal decomposition nor nucleation and growth, the two types of morphology often observed in the phase separation of systems at equilibrium. The formation of aggregates and crystals in the DCFs explains not only the low ET efficiency but also the effective quenching of the donor fluorescence, which is likely enhanced by exciton migration and lattice relaxation. Furthermore, the slower evaporation rate of $CHCl_3$ as compared to CS_2 results in more extensive phase separation in the $CHCl_3$-cast films as revealed by a lower ET efficiency. This is especially true in the PFO-P3HT DCFs but not so obvious in the PFO:MEH-PPV blends where ET behavior is quite similar in the DCFs prepared from CS_2 and $CHCl_3$. Clearly, the solubility of the blend components in each solvent plays an important role in the morphology of the films but its influence is more evidenced in the breath figures.

The phase separation patterns observed in the BFAs of the polymer-polymer blends as well as the higher ET efficiency in the BFAs cast from $CHCl_3$ than in those cast from CS_2 reveal the factors that influence the morphology. Carbon disulfide is non-polar and its interaction with the hydrophilic substrate is relatively weak. Thus, its tendency to diffuse away from the substrate is higher than that of the more polar chloroform. When this driving force is combined with the higher solubility of PFO in $CHCl_3$ than in CS_2, a substrate-adhering layer rich in PFO tends to form in the BF-structured films cast from CS_2 during the solvent evaporation process. On top of this layer, the blend composition becomes acceptor-rich and it is re-distributed laterally by hydrodynamic flow and evaporative cooling effects, resulting in domains with varying acceptor concentrations. The material transport dynamics may carry the acceptor-rich portions of the blend to an area where a layer of bubble arrays has been formed. Depending on the viscosity of the newly arrived solution, a new layer of disordered bubble arrays may form or no bubbles are formed at all. Consequently, when a blend solution in CS_2 is used to prepare the polymeric breath figures, phase separation in both vertical and lateral directions is likely although it is limited by the short solvent evaporation time.

When chloroform is employed, the solubility of the blend components in this solvent is more comparable. Moreover, the stronger interaction of $CHCl_3$ with the substrate decelerates the rate at which the blend components de-mix in the direction perpendicular to the substrate surface. Nevertheless, lateral phase separation still occurs due to hydrodynamic flow and evaporative cooling, the two effects driven by the flow of moist air over the surface of the blend solution. Thus, although chloroform evaporates slower than carbon disulfide, the better mixability of the blend components in chloroform

and the stronger interaction of this solvent with the substrate produce less extensive phase separation and higher ET efficiency in the BFAs cast from $CHCl_3$ than those prepared from CS_2. It is to be stressed that for BF-structured samples prepared from either solvent, phase separation is ultimately limited by the non-equilibrium states of the systems as dictated by such factors as rapid solvent evaporation, flow of moist air, convection, and surface cooling.

The phase separation behavior in the drop-coated films of PFO-TPP is similar to the counterparts in the polymer-polymer blends. That is, the morphology of the DCFs is influenced mostly by the rates of solvent evaporation and phase separated by the aggregation and crystallization of the blend components in vertical and lateral directions. Since donor-acceptor interactions are minimal, energy transfer efficiency is low although the quenching of the donor fluorescence is significant as resulted from the self-quenching processes. In the BFAs, however, the rapid solvent evaporation and the dynamics involved in the bubble-forming process do not enable crystallization of the blend components.

The morphology of the breath figures of PFO-TPP blends is determined mostly by the higher rate of diffusion of the molecular dye TPP. When the high diffusibility of TPP is considered along with the solubility of the blend components and the solvent interactions with the substrate surface as discussed above, vertical phase separation is much more extensive in the BFAs cast from CS_2 than those fabricated from $CHCl_3$. Consequently, despite the observation of lateral phase separation in the BFAs cast from the two solvents, energy transfer efficiency is much higher in the samples obtained from $CHCl_3$ solutions.

This study shows that fluorescence measurements can serve as an effective means in the investigation of thin film morphology when the materials are light-emitting polymers and dyes. Since this class of materials holds great potential for many advanced applications in electronics and photonics, the task of preparing the solid-state surfaces of the polymer-polymer and polymer-dye blends as well as characterizing and controlling the resulted film morphology poses a real challenge. The results obtained from this study have shown that correlation of energy transfer behavior with film morphology is an effective method that will aid us in the search for an answer to that challenge.

6.7 Future research direction

Phase separation in the breath figures and thin films of polymer-polymer and polymer-dye blends can not be properly studied without depth profile analysis. A major drawback in the use of the conventional depth profile analytical techniques such as XPS and nuclear reaction analysis (NRA) is the large cross-section area of the probe, which does not allow the analysis to be focused on small regions of a sample. For example, our understanding of phase separation of polymer blends in systems that are driven far from equilibrium such as in the breath figures will be greatly enhanced if a depth profile analysis can be done at the bubbles and at the inter-bubble areas. This can be achieved with either secondary ion mass spectrometry (SIMS) or confocal microscopy. State-of-the-art secondary ion mass spectrometers may allow analysis to be done within a small section (i.e., proportional to the bubble diameters) of a sample. Confocal microscopy can be employed to view the fluorescence energy transfer at each specific depth of a sample.

However, high-resolution confocal microscopy requires the sample to be coated with a layer of oil, which tends to delaminate the BFAs and DCFs that are prepared and investigated in this study. Another issue with the use of confocal microscopy for morphological study of the PFO-polymer and PFO-dye BFAs and DCFs involves photobleaching that is caused by the intense UV-laser light used to excite the samples.

This study has shown that phase separation behavior in the BFAs is dictated significantly by hydrodynamics. Thus, *in situ* study of phase separation in the breath figure structured samples is to be pursued in the near future. For energy donor-acceptor blends of light-emitting polymers and dyes, such an analysis may be achieved by using a fluorescence microscope to monitor the fluorescence energy transfer on the surface of a sample while bubble arrays are being fabricated. New findings may be revealed if the results from such study are then compared to those obtained for the samples subjected to the same bubble-forming environment but without humidity.

The effects of the diffusion rates of the blend components on film morphology are far-reaching as shown in this study and further investigation on these effects is called for. Thus, future studies will employ oligomers instead of polymers as energy acceptors. By varying the chain length of an oligomer, the diffusibility of that component can be controlled and related to the final film morphology.

4.8 References

.

[1] Perepichka, I. F., Perepichka, D. F., Meng, H., Wudl, F. *Adv. Mater*. **2006**, *17*, 2281.

[2] Moons, E. *J. Phys.: Condens. Matter* **2002**, *14*, 12235.

[3] Friend, R. H., Gymer, R. W., Holmes, A. B., Burroughes, J. H., Marks, R. N., Taliani, C., Bradley, D. D. C., Dos Santos, D. A., Brédas, J. L., Lögdlund, M., Salanek, W. R. *Nature (London)* **1999**, *397*, 121.

[4] Chen, L., McBranch, D. W., Wang, H., Helgeson, R., Wudl, F., Whitten, D. G. *Proc. Natl. Acad. Sci. U.S.A.* **1999**, *96*, 12287.

[5] Sariciftci, N. S. *Curr. Opin. Solid-State Mater. Sci.* **1999**, *4*, 373.

[6] Liu, Y., Nishiura, M., Wang, Y., Hou, Z. *J. Am. Chem. Soc*. **2006**, *128*, 5592.

[7] Byun, H. Y., Chung, I. J., Shim, H-K., Kim, C. Y. *Macromolecules* **2004**, *37*, 6945.

[8] Liu, J., Shi, Y., Yang, Y. *Appl. Phys. Lett.* **2001**, *79*, 578.

[9] Sun, Q. J., Fan, B. H., Tan, Z. A., Yang, C. H., Li, Y. F. *Appl. Phys. Lett*. **2006**, *88*, 163510.

[10] Klaerner, G., Lee, J. I., Davey, M. H., Miller, R. D. *Adv. Mater*. **1999,** *11,* 115.

[11] Shim, H. K., Kang, I. N., Jang, M. S., Zyung, T., Jung, S. D. *Macromolecules* **1997**, *30*, 7749.

[12] Chappell, J., Lidzey, D. G., Jukes, P. C., Higgins, A. M., Thompson, R. L., O'Connor, S., Grizzi, I., Fletcher, R., O'Brien, J., Geoghegan, M., Jones, R. A. L. *Nature Mater*. **2003**, *2*, 616.

[13] Greenham, N. C., Samuel, I. D. W., Hayes, G. R., Phillips, R. T., Kessener, Y. A. R. R., Moratti, S. C., Holmes, A. B., Friend, R. H. *Chem. Phys. Lett.* **1995**, *241*, 89.

[14] Veenstra, S. C., Verhees, W. J. H., Kroon, J. M., Koetse, M. M., Qweelssen, J., Bastiaansen, J. J. A. M., Schoo, H. F. M., Yang, X., Alexeev, A., Loos, J., Schubert, U. S., Wienk, M. M. *Chem. Mater*. **2004**, *16*, 2503.

[15] Yu, G., Gao, J., Hummelen, J. C., Wudl, F., Heeger, A. J. *Science* **1995**, *270*, 1789.

[16] Sirringhaus, H., Tessler, N., Friend, R. H. *Science* **1998**, *280*, 1741.

[17] Babel, A., Jenekhe, S. A. *Adv. Mater*. **2002**, *14*, 371.

[18] Hill, J., Heriot, S. Y., Worsfold, O., Tichardson, T. H., Fox, A. M., Bradley, D. D. C. *Synth. Met*. **2003**, *139*, 787.

[19] Buckley, A. R., Rahn, M. D., Hill, J., Cabanillas-Gonzalez, J., Fox, A. M., Bradley, D. D. C. *Chem. Phys. Lett*. **2001**, *339*, 331.

[20] Cerullo, G., Stagira, S., Zavelani-Rossi, M., De Silvestri, S., Virgili, T., Lidzey, D. G., Bradley, D. D. C. *Chem. Phys. Lett*. **2001**, *335*, 27.

[21] Virgili, T., Lidzey, D. G., Bradley, D. D. C. *Adv. Mater.* **2000**, *12*, 58.

[22] Redecker, M., Bradley, D. D. C., Inbasekaran, M., Woo, E. P. *Appl. Phys. Lett*. **1998**, *73*, 1565.

[23] Chen, S. H., Su, A. C., Su, C. H. *Macromolecules* **2005**, *38*, 379.

[24] Neher, D. *Macromol. Rapid. Commun*. **2001**, *22,* 1365.

[25] Scherf, U., List, E. J. W. *Adv. Mater*. **2002**, *14*, 477.

[26] Kawana, S., Durrell, M., Lu, J., Macdonald, J. E., Grell, M., Bradley, D. D. C., Jukes, P. C., Jones, R. A. L., Bennett, S. L. *Polymer* **2002**, *43,* 1907.

[27] Winokur, M. J., Slinker, J., Huber, D. L. *Phys. Rev. B* **2003**, *67*, 184106.

[28] Ariu, M., Lidzey, D. J., Lavrentiv, M., Bradley, D. D. C., Jandke, M., Strohriegl, P. *Synth. Met.* **2001**, *116*, 217.

[29] Lieser, G., Oda, M., Miteva, T., Meisel, A., Nothofer, H. G., Scherf, U. *Macromolecules* **2000**, *33*, 4490.

[30] Khan, A. L. T., Banach, M. J., Köhler, A. *Synth. Met*. **2003**, *139*, 905.

[31] Alam, M. M., Jenekhe, S. A. *Macromol. Rapid Commun.* **2006**, *27*, 2053.

[32] Hers, L. M., Phillips, R. T. *Phys. Rev. B* **2000**, *61*, 13691.

[33] Zeng, G., Yu, W. L., Chua, S. J., Huang, W. *Macromolecules* **2002**, *35*, 6907.

[34] List, E. J. W., Guentner, R., Scanducci de Freitas, P., Scherf, U. *Adv. Mater*. **2002**, *14*, 374.

[35] Jacob, J., Crimsdale, A. C., Müllen, K. *Macromolecules* **2003**, *36*, 8240.

[36] Hung, M-C., Liao, J-L., Chen, S-A., Chen, S-H., Su, A-C. *J. Am. Chem. Soc*. **2005**, *127*, 14576.

[37] Lemmer, U., Heun, S. Mahrt, R. R., Scherf, U., Hopmeier, M., Siegner, U., Göbel, E. O., Müllen, K., Bässler, H. *Chem. Phys. Lett*. **1995**, *240,* 371.

[38] Jenekhe, S. A., Osaheni, J. A. *Science* **1994**, *265*, 765.

[39] Brown, P. J., Thomas, D. S., Köhler, A., Wilson, J. S., Kim, J-S., Ramsdale, C. M., Sirringhaus, H., Friend, R. H. *Phys. Rev. B* **2003**, *67*, 064203.

[40] Xu, B., Holderoft, S. *Thin Solid Films* **1994**, *242*, 174.

[41] Babel, A., Jenekhe, S. A. *Macromolecules* **2003**, *36*, 7759.

[42] Geoghegan, M., Krausch, G. *Prog. Polym. Sci.* **2003**, *28*, 261.

[43] (For the synthesis of PFO derivatives) Jin, S-H., Park, H-J., Kim, J. Y., Lee, K., Lee, S-P., Moon, D-K., Lee, H-J., Gal, Y-S. *Macromolecules* **2002**, *35*, 7532 (and references therein).

[44] (For the synthesis of MEH-PPV) Hsieh, B. R., Yu, Y., VanLaeken, A. C., Lee, H. *Macromolecules* **1997**, *30*, 8094.

[45] (For the synthesis of regioregular P3HT) Loewe, R. S., Khersonsky, S. M., McCollough, R. D. *Adv. Mater.* **1999**, *11*, 250.

[46] (For the synthesis of TPP) Geier III, G. R., Ciringh, Y., Li, F., Haynes, D. M., Lindsey, J. S. *Org. Lett.* **2000**, *2*, 1745 (and references therein).

[47] Bunz, U. H. F. *Adv. Mater*. **2006**, *18*, 973.

[48] Ariu, M., Lidzey, D. G., Bradley, D. D. C. *Synth. Met.* **2000**, *111-112*, 607.

[49] Khan, A. L. T., Sreearunothai, P., Hers, L. M., Banach, M. J., Koehler, A. *Phys. Rev. B* **2004**, *69*, 085201.

[50] Chen, S. H., Su, A. C., Chou, H. L., Peng, K. Y., Chen, S. A. *Macromolecules* **2004**, *37*, 167.

[51] Förster, T. *Ann. Phys*. **1948**, *2*, 55.